

ADVERTIMENT. La consulta d'aquesta tesi queda condicionada a l'acceptació de les següents condicions d'ús: La difusió d'aquesta tesi per mitjà del servei TDX (www.tesisenxarxa.net) ha estat autoritzada pels titulars dels drets de propietat intel·lectual únicament per a usos privats emmarcats en activitats d'investigació i docència. No s'autoritza la seva reproducció amb finalitats de lucre ni la seva difusió i posada a disposició des d'un lloc aliè al servei TDX. No s'autoritza la presentació del seu contingut en una finestra o marc aliè a TDX (framing). Aquesta reserva de drets afecta tant al resum de presentació de la tesi com als seus continguts. En la utilització o cita de parts de la tesi és obligat indicar el nom de la persona autora.

ADVERTENCIA. La consulta de esta tesis queda condicionada a la aceptación de las siguientes condiciones de uso: La difusión de esta tesis por medio del servicio TDR (www.tesisenred.net) ha sido autorizada por los titulares de los derechos de propiedad intelectual únicamente para usos privados enmarcados en actividades de investigación y docencia. No se autoriza su reproducción con finalidades de lucro ni su difusión y puesta a disposición desde un sitio ajeno al servicio TDR. No se autoriza la presentación de su contenido en una ventana o marco ajeno a TDR (framing). Esta reserva de derechos afecta tanto al resumen de presentación de la tesis como a sus contenidos. En la utilización o cita de partes de la tesis es obligado indicar el nombre de la persona autora.

WARNING. On having consulted this thesis you're accepting the following use conditions: Spreading this thesis by the TDX (www.tesisenxarxa.net) service has been authorized by the titular of the intellectual property rights only for private uses placed in investigation and teaching activities. Reproduction with lucrative aims is not authorized neither its spreading and availability from a site foreign to the TDX service. Introducing its content in a window or frame foreign to the TDX service is not authorized (framing). This rights affect to the presentation summary of the thesis as well as to its contents. In the using or citation of parts of the thesis it's obliged to indicate the name of the author



Stochasticity, complexity and synchronization in semiconductor lasers

Jordi Tiana i Alsina

Memoria presentada per optar al grau de Doctor per la
Universitat Politècnica de Catalunya

Directors:

Jordi García Ojalvo

M. Carme Torrent Serra

Departament de Física i Enginyeria Nuclear

Universitat Politècnica de Catalunya

Terrassa, 2011

Contents

I	INTRODUCTION	1
1	An overview of semiconductor Edge-Emitting Lasers (EEL)	3
1.1	General description	3
1.2	Types of EELs	6
1.2.1	Homostructure lasers	6
1.2.2	Heterostructure lasers	6
1.2.3	Gain and index guided lasers	8
1.2.4	Types of EEL cavities	10
1.3	Rate equations for a solitary semiconductor laser	13
1.4	EEL characteristics	14
1.4.1	Ligth-current characteristics	14
1.4.2	Optical spectrum characteristics	16
2	Dynamics of single semiconductor lasers	21
2.1	Optical feedback	22
2.1.1	Rate equations for a semiconductor with feedback	22
2.1.2	Regimes of optical feedback	26

2.2	Pump current modulation	32
2.3	Pump current modulation and optical feedback	34
3	Dynamics of coupled semiconductor lasers	37
3.1	Synchronization	37
3.1.1	Phase and frequency locking	38
3.1.2	Synchronization of two oscillators	42
3.1.3	Kinds of synchronization	45
3.2	Synchronization in coupled semiconductor lasers	50
3.2.1	Unidirectional injection in a semiconductor lasers	51
3.2.2	Bidirectional injection	56
4	Stochasticity and complexity in dynamical systems	61
4.1	Entropy and statistical complexity	62
4.2	Forbidden ordinal patterns	68
II	Results: Laser with feedback	73
5	Temporal correlations induced by intrinsic rate switching in a semiconductor laser with feedback	75
5.1	Experimental setup	76
5.2	Serial correlation (SCC) at constant pumping	78
5.3	Two-state theory of laser dropouts	79
5.4	Comparison between experiments and theory	81
5.5	Externally controlled state switching	83

5.6	Conclusions	85
6	Language structure of a semiconductor laser with feedback	87
6.1	Symbolic analysis of low-frequency fluctuations	89
6.2	Experimental results	92
6.3	Comparison with theoretical models	98
6.3.1	The LK model	98
6.3.2	The EMG model	102
6.4	Conclusions	105
7	Quantifying the statistical complexity in a semiconductor laser with optical feedback	107
7.1	Experiments	110
7.2	Statistical characterization of the time series	112
7.3	Quantifying the statistical complexity	114
7.4	Conclusions	118
III	Results: Coupled lasers	119
8	Quantifying the stochasticity in the dynamics of two mutually coupled semiconductor lasers	121
8.1	Experimental setup	122
8.2	Experimental results	124
8.3	Numerical simulations	129
8.4	Conclusions	132

9	Dual-lag synchronization due to path-delay interference	133
9.1	Experimental setup	134
9.2	Experimental results	136
9.3	Numerical simulations	138
9.4	Chaotic communications	141
9.5	Conclusions	144
10	Zero-lag synchronization and bubbling in bidirectionally coupled lasers	147
10.1	Experimental setup	148
10.2	Zero-lag synchronization and bubbling	152
10.2.1	The role of detuning	153
10.2.2	The role of pump current	154
10.3	Conclusions	160
IV	Conclusions	163
11	Conclusions and future work	165
11.1	On the chaotic dynamics of a semiconductor laser with feedback . . .	165
11.2	On the synchronization of coupled semiconductor lasers	167
11.3	Perspectives for future work	168
V	APPENDICES	171
A	Derivation of the rate equations for a semiconductor laser	173

B	Statistical tools	183
B.1	Correlations	183
B.1.1	Auto-correlation	183
B.1.2	Cross-correlation	186
B.1.3	Sliding cross-correlation	188

List of publications related with this Thesis

- Tiana-Alsina, J., Buldú, J. M., Torrent, M. C., and Garcia-Ojalvo, J. *Quantifying stochasticity in the dynamics of delay-coupled semiconductor lasers via forbidden patterns*. Phil. Trans. R. Soc. A 368, 367-377 (2010).
- Tiana-Alsina, J., Torrent, M. C., Rosso, O. A., Masoller, C., and Garcia-Ojalvo, J. *Quantifying the statistical complexity of low-frequency fluctuations in semiconductor lasers with optical feedback*. Phys. Rev A 82(1), 013819 (2010).
- Rubido, N., Tiana-Alsina, J., Torrent, M. C., Garcia-Ojalvo, J., and Masoller, C.. *Language organization and temporal correlations in the spiking activity of an excitable laser: Experiments and model comparison*. Phys. Rev. E 84(2), 026202 (2011).
- Tiana-Alsina, J., Garcia-Lopez, J. H, Torrent, M. C., and Garcia-Ojalvo, J. *Dual-lag synchronization between coupled chaotic lasers due to path-delay interference*. Chaos, in press (2011).
- Tiana-Alsina, J., Hicke, K., Porte, X., Soriano, M. C., Torrent, M. C., Garcia-Ojalvo, J. and Fischer, I. *Zero-lag synchronization loss due to bubbling in delay-coupled lasers*. To be submitted to Phys. Rev. E (Rapid Comm).
- Tiana-Alsina, J., Schwalger, T., Torrent, M. C., Garcia-Ojalvo, J. and Lindner, B. *Inter-spike correlations induced by dichotomous noise modulation in an excitable laser*. To be submitted to Phys. Rev. Lett.

Conference contributions related with this Thesis

- FisEs'08 (Salamanca 2008), *Caracterización dinámica de redes modales en láseres de semiconductor*, Tiana-Alsina, J., Torrent, M. C., and Garcia-Ojalvo, J. **Poster contribution.**
- NoLineal'08 (Barcelona 2008), *Estocasticidad en la dinámica leader-laggard en dos láseres de semiconductor acoplados*, Tiana-Alsina, J., Buldú, J. M., Torrent, M. C., and Garcia-Ojalvo, J. **Oral contribution.**
- CLEO Europe-EQEC'09 (Munich 2009), *Lag alternance in unidirectional coupled semiconductor lasers*, Tiana-Alsina, J., Garcia-Lopez, J. H, Torrent, M. C., and Garcia-Ojalvo, J. **Poster contribution.**
- CLEO Europe-EQEC'09 (Munich 2009), *Lag synchronization in delay-coupled semiconductor lasers*, Garcia-Ojalvo, J., Gonzalez, M. C., Tiana-Alsina, J., Torrent, M. C., Fischer, I., and Berkvens, T. **Oral contribution.**
- DCS'09 (Dresden 2009), *Delay interference in semiconductor lasers coupled via multiple paths*, Tiana-Alsina, J., Garcia-Lopez, J. H, Torrent, M. C., and Garcia-Ojalvo, J. **Oral contribution.**
- QUONLOP'11 (Valladolid 2011), *Inter-spike correlations induced by dichotomous noise modulation in an excitable laser*, Tiana-Alsina, J., Schwalger, T., Torrent, M. C., Garcia-Ojalvo, J. and Lindner, B. **Oral contribution.**

- FisEs'11(Barcelona 2011), *Inter-spike correlations induced by dichotomous noise modulation in an excitable laser*, Tiana-Alsina, J., Schwalger, T., Torrent, M. C., Garcia-Ojalvo, J. and Lindner, B. **Poster contribution.**
- CLEO Europe-EQEC'11 (Munich 2011), *Experimental characterization of bubbling in delay-coupled semiconductor lasers*, Porte, X., Tiana-Alsina, J., Hicke, K., Torrent, M. C., Garcia-Ojalvo, J., and Fischer, I. **Oral contribution.**
- CLEO Europe-EQEC'11 (Munich 2011), *Zero-lag synchronization of two delay-coupled lasers: The role of detuning*, Hicke, K., Tiana-Alsina, J., Porte, X., Torrent, M. C., Garcia-Ojalvo, J., and Fischer, I. **Poster contribution.**

Agraïments

Durant els anys en que he estat realitzant la Tesi Doctoral he estat envoltat de moltíssima gent, que d'una manera o d'una altra, m'han ajudat a que aquest projecte hagi arribat a bon port. Vull agrair, en primer lloc, als meus dos Directors de Tesi, en Jordi García Ojalvo i la M^a.Carme Torrent, grans científics i millors persones. M'és impossible imaginar tot aquest procés sense la vostra implicació, dedicació i suport. Sou sensacionals.

També agrair als col.laboradors amb qui he tingut el plaer de treballar. Gràcies Javier per les teves idees i aportacions sorolloses però sempre consistens. Com no, també agrair a l'Ingo Fischer, en Claudio Mirasso, en Konstantin i en Xavier la seva càlida benvinguda al laboratori de làsers de IIFISC. Vaig disfrutar com un nen amb sabates noves amb el vostre material. Reconèixer també les aportacions tèoriques d'en Benjamin Lindner i d'en Tilo Schwalger, sense vosaltres no hauríem fittejat ni una paràbola. Per últim, agrair a la Cristina Masoller i l'Osvaldo A. Rosso que m'introduïssin en el fabulós món de la complexitat, gràcies. Si d'alguna cosa m'ha servit aquesta tesi és per entendre que sense un gran grup humà és molt difícil treballar a gust i, evidentment en aquest he treballat molt a gust.

A la Cristina Martinez per ajudar-me a fer els primers passos en el tangible món dels experiments, gràcies. Gràcies Toni per introduir-me al món del bash scripting durant el temps que vam compartir despatx. Agrair també a la Lorena, la Belén, la Núria, la Marta, l'Andrés i al Pau (des de que has arribat el Toni ha passat del bash al python). Amb vosaltres es pot parlar de ciència però també de tantes i tantes coses. i tamb com no agrair a tots els membres de grup de recerrca DONLL

Finalment vull agrair el suport inestimable de la família i als amics. Sense vosaltres res seria el mateix. Visca Sabadell, visca Can vaques i visca Catalunya. Els moments amb vosaltres han estat maravellosos.

Al Roc, la Núria i l'Anna

Chapter 1

An overview of semiconductor Edge-Emitting Lasers (EEL)

1.1 General description

A laser is a device that emits spatially and temporally coherent light. The term “laser” is an acronym for “Light Amplification by Stimulated Emission of Radiation”. The invention of the laser can be dated to 1958 with the theoretical work by Schawlow & Townes (1958). The process to achieve laser light has three main ingredients: pumping, amplification via stimulated emission and cavity confinement. The pumping process consists in an external energy source that raises a certain electronic, atomic, or molecular state into a higher-energy (“excited”) quantum state. As Einstein predicted in 1917 (see e.g. Hawkes & Latimer (1995)), the light can interact with matter by either absorbing or emitting photons. The emission can be spontaneous or stimulated. Stimulated emission is a process by which an incident wave interacts with a particle lying at some excited state and consists in the emission of a photon identical to one photon of the incident wave. Note that “identical” here means same direction of propagation, frequency and phase as the incident photon.

Stimulated emission takes place when the number of particles in one excited state exceeds the number of particles in some lower-energy state (i.e. when population inversion is achieved). When the population inversion is achieved and the gain due to stimulated emission is larger than the absorption, the light is amplified. Finally, when such an optical amplifier is placed inside a resonant optical cavity, one obtains a laser. The role of the cavity is important for two aspects, first, the cavity creates a preferred direction for the light propagation parallel to the optical axis of the cavity, and second, the cavity makes the amplification more efficient, due to the fact that a photon can cross many times the gain medium. The cavity also selects the frequencies of radiation that will be sustained. These frequencies are known as cavity modes.

Lasers can be characterized by three physical quantities: the optical field, the polarization of the material and the population inversion. As Haken (1975) showed, lasers are nonlinear systems and can display chaotic behavior on their output power, due to the fact that the above mentioned physical quantities correspond to three coupled nonlinear degrees of freedom. Arecchi et al. (1984) analyzed the role of the relaxation times of the three variables and categorized the lasers in three classes: A, B and C. Class C lasers have to be described by the full set of laser variables and so, they can exhibit intrinsic chaotic behavior. Class B lasers can be fully described only taking into account the field and the population inversion, and class A lasers are described only by the field. Therefore class A and B lasers cannot display chaotic dynamics unless we introduce external perturbations (Weiss & Vilaseca, 1991) (more details will be presented in Sec. 1.3 and Ch. 2).

From now on we will focus on semiconductor lasers. This type of laser can be classified as class-B lasers. Semiconductor Edge-Emitting Lasers (EEL) are the original and still very widely used form of semiconductor lasers. In contrast to other types of lasers, these are very efficient, have very simple power supply requirements and they are physically very small. As it is shown in Fig. 1.1, semiconductor lasers consist in a pn -junction inside an optical resonator, operating in forward bias (a

positive voltage is applied to the p-side layer with respect to the n-side) that produces two kinds of charge carriers (electrons and holes). Electrons are injected from the n-doped region to the p-doped region and holes move in the opposite direction. This effect results in a region, called active layer, where holes and electrons can recombine and thereby emit a photon by spontaneous emission, which is necessary to initiate the stimulated emission, i.e laser light. The polished end faces of the pn-junction act as a cavity that is designed to resonate at the frequency corresponding to the energy gap of the semiconductor, amplifying the photons that propagate inside the cavity. In order to achieve lasing in a preferred direction, longitudinal faces are accurately cut, while side faces in all other directions, are roughened to avoid emission. The cavity length is around a few hundred micrometers, which is sufficient to reach a high gain. Lasing takes place only when the amplification is higher than the losses inside the cavity. Due to the high gain of the semiconductor laser material, lasing occurs even if the end facets (edges) are not coated and there is only the Fresnel reflection of the semiconductor/air interfaces. The reflectivity of the facets is given by $R = \frac{(n_m - n_a)^2}{(n_m + n_a)^2}$, where n_m and n_a are the refracting indices of the semiconductor material and air, respectively. For typical values of semiconductor refractive index, around 70% of the light escapes from the laser cavity.

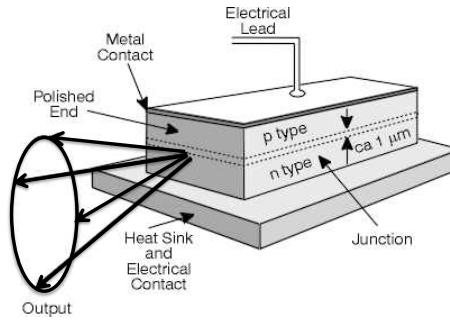


Figure 1.1: Simple scheme of edge-emitting semiconductor laser. Note that lasing occurs in the plane of the junction. From Simcik (1995).

1.2 Types of EELs

In this section we discuss the most common types of edge-emitting semiconductor lasers. We can classify EELs in two groups, depending on their internal structure.

1.2.1 Homostructure lasers

This type of laser is the simplest one and, as we have discussed in Sec. 1.1, consists of a single pn -junction operated in forward bias. Because the materials in each side of the junction are made by doping the same semiconductor material, such lasers are termed homostructures. Experimental investigations published simultaneously by Nathan et al. (1962) in IBM, Hall et al. (1962) in General Electric, and Quist et al. (1962) from MIT Lincoln Laboratories, showed laser amplification in GaAs diodes. These lasers do not exhibit any form of carrier confinement. The lack of confinement for a homostructure implies that the carriers are neither confined nor concentrated but are spread by diffusion. This fact leads to the homostructure lasers having an active region with a low concentration of excess carriers. Lasing takes place in the plane of the junction and the optical field is usually plane polarized, with the electric field vector lying in the plane of the junction. Due to the fact that carriers injected into the active layer diffuse away from the junction, the threshold current is very high at room temperature. Another drawback of this type of structures is the absence of any waveguiding mechanism. Therefore, it is hard to control the transversal mode characteristics. It is worth to note that this type of laser is technologically obsolete nowadays.

1.2.2 Heterostructure lasers

The high threshold currents for the simple pn -junction lasers described above motivated the development of new internal structures. Alferov et al. (1970) and Hayashi

et al. (1970) started to develop heterojunction structures in order to reduce the electron diffusion and thereby reduce the threshold current at room temperature. This new type of laser consist of an active region sandwiched between two layers that have a larger bandgap and also a smaller refractive index. This difference in the bandgap confines the electrons and holes to the active layer and prevent electrons to difusse freely due to the presence of a potential barrier. Moreover, the difference in the refractive index creates a waveguide which confines the light within the active region (Liu, 2005). There are several types of heterostructures, the two basic ones being the single heterostructure (SH) and the double-heterostructure (DH), depending on whether the active region is surrounded by one or two cladding layers of higher bandgap. In Fig. 1.2 we show the differences between homo and hetero-junction diode lasers in terms of the internal structure and energy bands.

The waveguide effect and the carrier confinement in the double heterostructure geometry are much more effective than in the single one. The reason is that in the SH there is no significant refracting index and energy gap difference between p -doped and n -doped semiconductor material while in DH the energy gap and refracting index difference between semiconductor material is enhanced.

The active layer in a DH is typically between 100 – 300 nm. When the active layer of a DH is thin enough (< 50 nm), the structure becomes a quantum well (QW). The current in a double-heterojunction semiconductor laser (for example PpN) is primarily carried by the electrons injected from the wide-gap N to the narrow-gap p layer (Liu, 2005). A possible real implementation for the double heterostructure junction, in terms of the chosen semiconductor materials, could be AlGaAs for the N and P layers and GaAs for the p layer. Note that we use capital letters to refer to higher energy gaps and lowercase to lower energy gaps. For these materials, the corresponding gap energies are $E_{g,N} = E_{g,P} = 2$ GeV, $E_{g,p} = 1.4$ GeV and the difference between refracting indices $\Delta n = 5\%$.

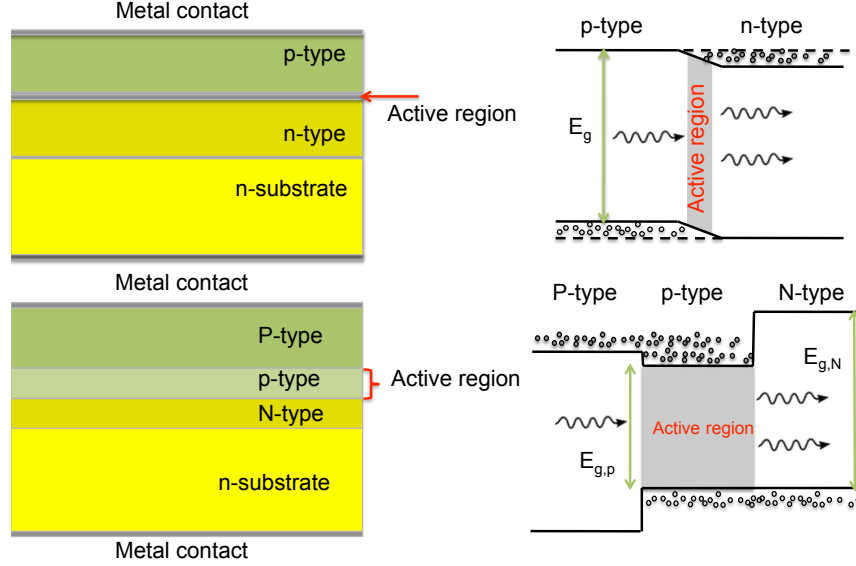


Figure 1.2: Internal structure and energy band diagram for homojunction (upper panel) and double heterojunction (lower panel) semiconductor lasers. Homojunction lasers consist in a pn -junction obtained by doping the same semiconductor material. Double heterojunction consist in a PpN -junction composed by an active region (p -type) sandwiched between two layers that have a larger band-gap (P and N -type).

1.2.3 Gain and index guided lasers

The lasers described in the previous sections can emit anywhere within the junction plane, thereby multiple transverse modes in the emission profile can be observed. This problem can be solved, and also lower threshold currents achieved, if some kind of lateral confinement in the current and/or photons is introduced in the junction plane. There are two main techniques used to achieve lateral confinement, which are known as gain-guiding and index-guiding (Liu, 2005; Hawkes & Latimer, 1995), which we describe in what follows.

Gain-guiding structures

The gain-guiding geometry is based on injecting the current within a narrow stripe ($\sim \mu\text{m}$) and therefore a striation of concentrated carriers in the active layer is formed along the longitudinal direction of the laser. As it is shown in Fig. 1.3, no additional lateral structure is incorporated in the device. In a semiconductor, an increase in carrier concentration is generally accompanied by a decrease in refractive index, and hence an undesirable antiguidance effect appears and tends to spread the light laterally instead of confining it. In this type of laser this effect is counteracted by the optical gain that is concentrated along the stripe. The width of a gain-guiding device varies between 10 and 200 μm . A wide stripe allows a large current to be injected leading to a high-power device. A gain-guided laser tends to oscillate in multiple transverse modes, making it difficult to focus or collimate. This kind of laser finds important applications in areas where high-power and high conversion efficiency are needed, but coherence and collimation are not so important.

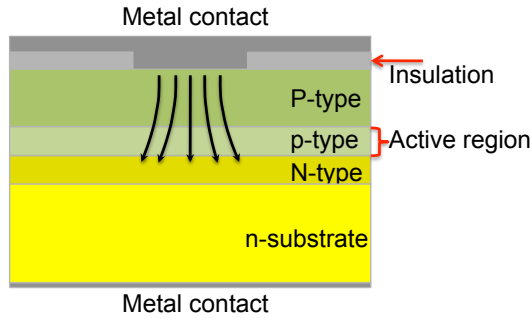


Figure 1.3: Internal lateral structure for a gain-guided semiconductor laser.

Index-guiding structures

For an effective lateral optical confinement, an index-guided structure has to be used. By introducing a lateral index profile around the active area, along the stripe where current is injected, a lateral waveguide is formed. In Fig. 1.4 we show the internal lateral structure for index-guided lasers. In this type of laser antiguidance

effect is not important, because the refracting index steps that form the waveguide are larger than the small changes in the refractive index caused by the carriers injected in the active region. The bandgap steps, associated with the refracting index steps, create energy barriers for the carriers, thereby a high concentration of carriers can be injected and confined inside the active region. For single transverse mode lasers, the width of the stripe is around $1 - 2\mu\text{m}$. For index-guiding lasers, the threshold current and the output beam characteristics are improved with respect to gain-guided devices.

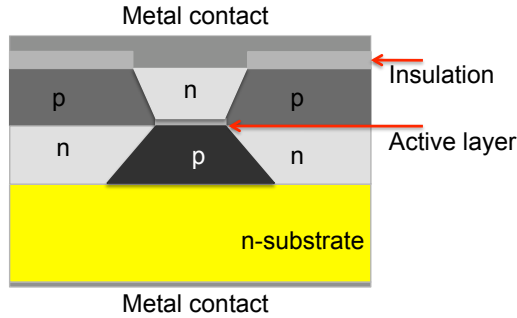


Figure 1.4: Internal lateral structure for an index-guided semiconductor laser. Lateral confinement of the optical field is achieved by surrounding the active area with semiconductor materials with lower refractive index.

1.2.4 Types of EEL cavities

So far we have classified the lasers depending on their internal structure. On the other hand, it is common to classify the lasers according to the type of the cavity. There are three main types of cavities for EELs lasers:

Fabry-Perot cavity lasers

A Fabry-Perot resonant cavity for an EEL simply consists in two cleaved end facets. Since a semiconductor material has a high refracting index ($n \sim 3$), a cleaved facet in air has a reflectivity typically in the range of 25% – 35%. Lasers with a Fabry-Perot cavity emit equally from both ends. In order to increase the output power,

one of the facets can be coated with a total-reflection coating, so the total laser output is emitted only from the uncoated end facet. This kind of lasers typically emit in multiple longitudinal modes with mode spacing equal to:

$$\Delta\nu_L = \frac{c}{2n_g L}, \quad (1.1)$$

where $n_g = n + \omega \frac{dn}{d\omega}$ is the group refracting index that depends on the emitting frequency (see Sec. 1.3). L and c are the laser cavity length and the speed of light, respectively.

Distributed Bragg Reflector (DBR) lasers

A DBR laser basically uses one or two frequency-selective Bragg reflectors, such as gratings parallel to the junction plane as end mirrors, as it is shown in Fig. 1.5(left). Figure 1.5(right) shows an electron micrograph of the Bragg reflector. Choosing the grating period Λ , a DBR can be designed to have a peak reflectivity at a desired Bragg frequency. The frequency bandwidth for a high reflectivity DBR device is approximately (Hawkes & Latimer, 1995):

$$\Delta\nu_{DBR} \simeq \frac{|\kappa|c}{\pi n_{g,\beta}}, \quad (1.2)$$

where $n_{g,\beta}$ is the effective group refracting index of the mode field at the Bragg frequency and κ is the wave vector of the incident field. Though a DBR laser cavity has multiple longitudinal modes (as a Fabry-Perot cavity), the DBR mirrors are much more frequency selective. Therefore, if the DBR bandwidth $\Delta\nu_{DBR}$ is made sufficiently narrow, this type of laser will oscillate with a single longitudinal mode at a frequency close to the Bragg frequency. Figure 1.6 shows the mechanism to select a single longitudinal mode in a DBR device. First, as usual in any semiconductor laser, a set of cavity modes are selected by the optical gain curve (red) and then, a single mode is selected by using the Bragg reflectivity curve (green).

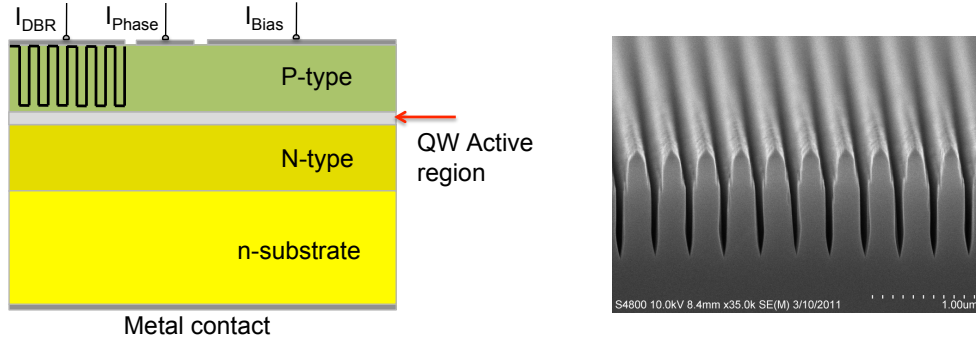


Figure 1.5: Schematic representation of the structure of an asymmetric-cladding DBR laser diode (left panel). External diffraction gratings serve as mirrors in a DBR lasers. Cross section of a first-order distributed Bragg reflector grating (right panel), from Ferdinand-Braun-Institut (2011).

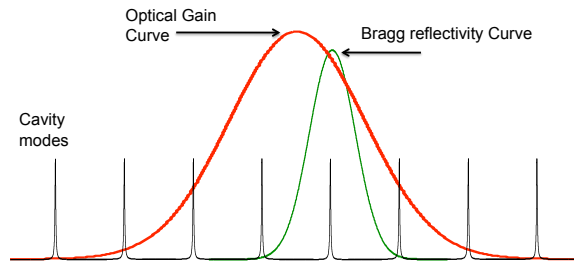


Figure 1.6: Mechanism to select a single longitudinal mode in a DBR device.

Distributed Feedback lasers (DFB)

A DFB laser replaces the back mirror with a grating along the cavity axis. An scheme of a DFB laser is depicted in Fig. 1.7. Because the grating runs along the whole length of the active region, where optical gain takes play, it does not behave as a passive reflector. The grating acts as a frequency selector due to the fact that it reflects a narrow band of optical frequencies, producing a single longitudinal lasing mode. For a periodicity of the grating equal to Λ there will be strong reflections for

the set of wavelengths equal to:

$$\lambda_m = \frac{2\Lambda n}{m}, \quad (1.3)$$

where n is the refracting index and m the mode number. For $m = 1$, the wavelength separation between Bragg resonances is much larger than the Fabry-Perot mode separation, and consequently a single mode operation is achieved. Traditionally, DFBs are antireflection coated on one side of the cavity and coated for high reflectivity on the other side.

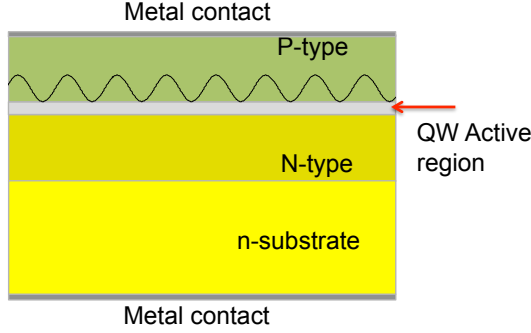


Figure 1.7: Internal lateral structure for a DFB semiconductor laser. The black curve corresponds to the grating used to select one single mode.

1.3 Rate equations for a solitary semiconductor laser

In this section we want to present the rate equations for a semiconductor laser that will allow us to understand the basic laser dynamics. As we have discussed in Sec. 1.1, semiconductor lasers can be classified as Class B lasers, due to the fact that the polarization relaxation time ($T_p < 0.1$ ps) is orders of magnitude smaller than the other relaxation times (photon lifetime $T_{ph} > 1$ ps and the carrier population inversion $T_n > 1$ ps). Therefore, the polarization can be adiabatically eliminated and the laser can be fully described by using the electric field and the population inversion, which in the case of these kind of lasers are the carriers.

Under these assumptions, the rate equations that describe the dynamics of a semiconductor laser and govern the electric field and the carrier density number are (see Appendix A for a complete derivation):

$$\frac{dE(t)}{dt} = \frac{(1 + i\alpha)}{2} [G(N, |E|^2) - \gamma] E(t) + \sqrt{2\beta N} \zeta(t), \quad (1.4)$$

$$\frac{dN}{dt} = C - \gamma_e N - G(N, |E|^2) |E|^2, \quad (1.5)$$

where E is the slowly-varying complex field amplitude and N is the carrier density. G is the nonlinear optical gain that includes a saturation coefficient ϵ :

$$G(N, |E|^2) = \frac{g_N N}{1 + \epsilon |E|^2}. \quad (1.6)$$

Other internal parameters of the laser are the linewidth enhancement factor α , and the injection current parameter C , normalized such that the threshold of the solitary laser is at $C = 1$. The term $\zeta(t)$ is a Gaussian white noise of zero mean and intensity unity with noise strength β .

A detailed derivation of the above mentioned rate equations is presented in Appendix A.

1.4 EEL characteristics

In this section, we discuss important lasing characteristics of edge emitting lasers, such as the power response of the emitted light versus pump current, and the optical spectrum characteristics for the different types of EELs that have been used in this Thesis.

1.4.1 Ligth-current characteristics

One of the most important characteristics of a semiconductor laser is the amount of light that it emits for a given injected current. As it was discussed before, a diode

laser converts electrical energy into optical output. The response of the laser can be depicted in a light-current curve (Fig. 1.8). With these curves one can derive the efficiency of the diode laser and also the threshold current (Herstens, 2005). As it is depicted in Fig. 1.8, when the pump current is increased, the laser first shows spontaneous emission and the output power grows very slowly (in the Figure it appears as a flat line). At a given value of the pumping (i.e I_{th}), the laser starts to emit stimulated light and the laser power increases linearly with the injection current.

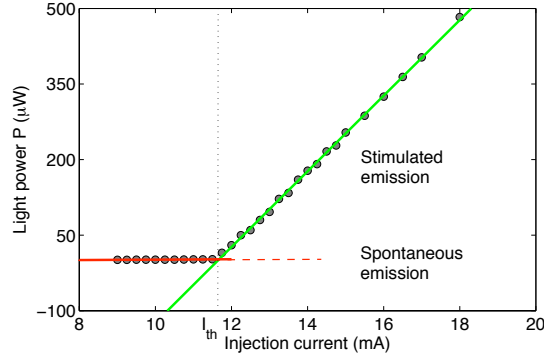


Figure 1.8: Schematic behavior of the power laser for different injection current values. I_{th} is the threshold current that marks the border between spontaneous and stimulated emission. Experimentally obtained at room temperature by using an InGaAsP Fabry-Perot semiconductor laser (Mitsubishi ML925B45F).

The light-current curve depends on the temperature of the laser diode, leading to a dependence between threshold current and temperature. The relation between I_{th} and T has the following expression (Herstens, 2005):

$$I_{th} = I_c \exp\left(\frac{T}{T_0}\right), \quad (1.7)$$

where I_c is a constant and T_0 is the characteristic temperature of the device (typically between 60 and 150 K). In Fig. 1.9, we show different light-current curves for different

values of the temperature. Note that, as given by Eq. 1.7, the threshold of the laser is strongly affected by the laser's temperature.

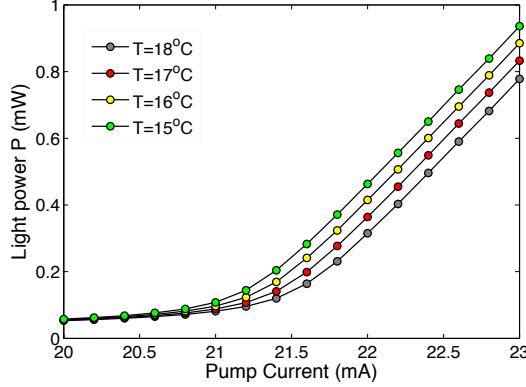


Figure 1.9: Light-current characteristics for an AlGaInP Fabry-Perot semiconductor laser (Sharp GH06510B2A) operating at different temperatures.

1.4.2 Optical spectrum characteristics

Another important characteristic of laser diodes is the optical spectrum. The optical spectrum also changes when the pump current is varied. At low pump currents the spectrum is multimode, but for sufficiently high pump currents, corresponding to high optical powers, the lasing operation becomes monomode, as can be seen in Fig. 1.10 (left and right panels respectively).

In this Thesis, we have employed three different types of semiconductor lasers. If we focus on the wavelength of the lasers, we can group them into two groups: infrared and visible lasers. In Fig. 1.11 we show the typical optical spectra of the lasers employed. In this figure we can see one laser (upper panel) operating at nominal wavelength $\lambda \sim 650$ nm (i.e visible) and two lasers (central and lower panels) operating at nominal wavelength $\lambda \sim 1550$ nm (i.e infrared). If we focus

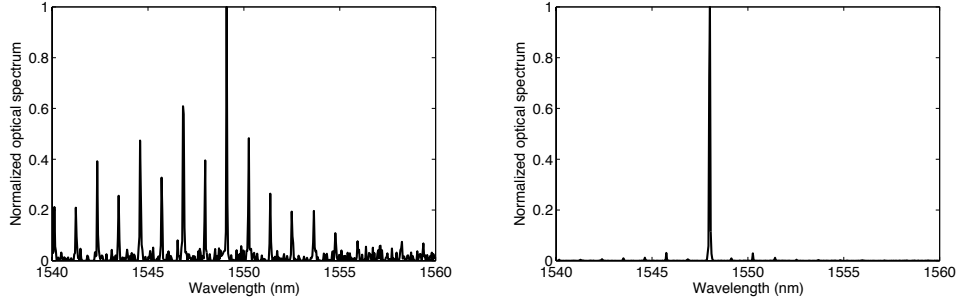


Figure 1.10: Optical spectrum below and well above threshold for a pigtailed Fabry-Perot semiconductor laser (Mitsubishi ML925B45F) composed by InGaAsP semiconductor material.

on the shape of the optical spectra, one can classify the lasers as monomode and multimode. The first two panels show a multimode behavior and the lower has only a single mode. Finally, one can classify the lasers according to the cavity type. The lasers in the upper and central panels of Fig. 1.11 have a Fabry-Perot cavity and the one in the lower panel has a DBR cavity. Note that the two Fabry-Perot lasers exhibit multimode behavior.

Another important characteristic of the optical spectrum of a semiconductor laser are the variations of the central wavelength with temperature. In Fig. 1.12 we show the optical spectrum as function of the temperature for the three lasers discussed above. A temperature variation of a laser causes a refractive index change of the semiconductor material that implies a shift of the cavity modes. Another consequence of a change in temperature is a shift of the maximum gain of the laser material, which produces a change of the emission wavelength. This fact can be understood due to that an increase of the temperature results in a reduction of the band-gap, resulting in a shift of the gain towards longer wavelength. Since the change of the wavelength of the cavity modes and the change of the center wavelength of the optical gain are not synchronous, multimode emission and mode

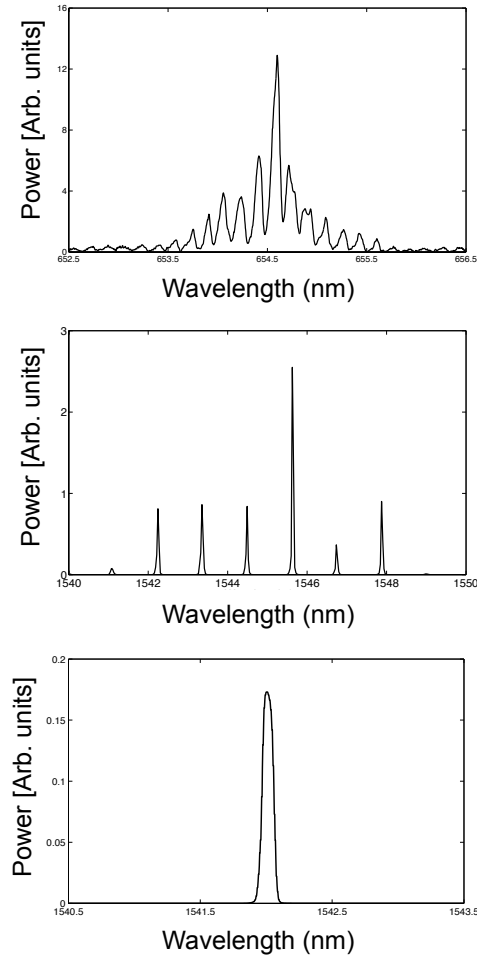


Figure 1.11: Optical spectra for the three kind of lasers used in this Thesis. The upper panel corresponds to a AlGaInP Fabry-Perot laser emitting at ~ 650 nm (Sharp GH06510B2A), the middle panel corresponds to InGaAsP Fabry-Perot laser emitting at ~ 1550 nm (Mitsubishi ML925B45F), and the bottom panel InGaAsP DBR laser emitting at ~ 1550 nm (Eblana ye1149).

hopping (see Fig. 1.12, upper and central panels) often occur. In the case of the DBR laser (lower panel), a similar increase of the wavelength with temperature is observed, but all the power is concentrated in a single mode, thus no mode-hopping occurs.

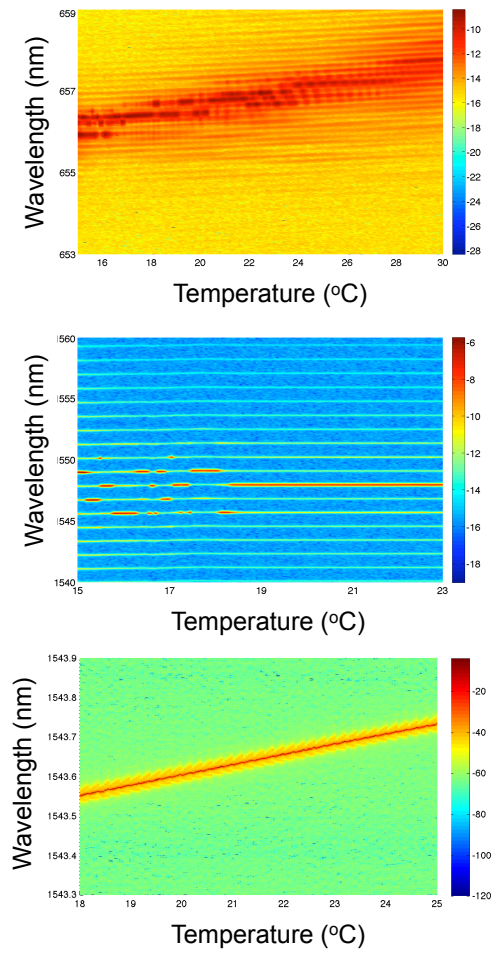


Figure 1.12: Optical spectrum behavior as a function of temperature for the three lasers used in this thesis. The panels correspond to the three lasers presented in Fig. 1.11. The data from bottom panel is courtesy of K. Hicke (IFISC).

As it can be seen in Fig. 1.12 (upper and central panel) the central wavelength of the semiconductor laser jumps between discrete wavelength values (mode hopping). Under some circumstances these mode hops can occur in an erratic manner, with the laser switching back and forth rapidly between wavelengths. During mode hopping, the lasers output intensity fluctuates slightly, resulting in an increase in relative intensity noise (mode partition noise). This mode hopping can occur even when the laser temperature and current are tightly controlled. As has been shown above, the laser cavity can support many different wavelengths. In laser diodes, these modes are separated by 0.2-1.0 nm. It is the wavelength of the peak of the gain profile relative to the mode wavelengths that determines which mode lases. The mode nearest the gain peak will lase; however, if the gain peak is between two modes, then the modes will compete for gain. Spontaneous emission will tip the balance first in favor of one mode and then the other, thereby causing mode hopping. If a multimode emission occurs, the different optical modes can be considered as amplified spontaneous emission noise. In Fig. 1.12 (central panel), we show that mode hopping noise occurs for low temperatures and at a certain temperature the laser stabilizes at a specific mode.

Chapter 2

Dynamics of single semiconductor lasers

Edge-emitting semiconductor lasers are very sensitive to external perturbations, such as optical feedback and/or pump current modulation, and due to that, they easily show unstable behavior. The reason for this high sensitivity can be explained by the fact that semiconductor lasers have high gain, low cavity mirror reflectivities, and weakly damped relaxation oscillations. Moreover, the α -parameter is a very important factor in the emergence of instabilities (Dente et al., 1988; Masoller, 1997a), as discussed in Appendix A. Optical feedback effects in semiconductor lasers have been extensively investigated in the past three decades (Fischer et al., 1996; Vaschenko et al., 1998; Ohtsubo, 2002). They are relevant, not only for practical applications in which the laser is subjected to feedback from an external reflector, but also they are very interesting from a nonlinear dynamics point of view, as optical feedback can induce a rich variety of dynamical regimes, including multi-stability, excitability and high-dimensional chaos.

2.1 Optical feedback

A chaotic oscillator consists in a system that shows irregular behavior although this does not mean complete unpredictability. More specifically, a chaotic system is deterministic, that means, if we know with infinite accuracy the state of the system at a certain time $t = 0$, the dynamics at time $t > 0$ is determined uniquely. But since it is not possible to know the variables of the system with infinite accuracy and due to the fact that a chaotic system is very sensitive to initial conditions, we cannot predict the state of the system for long times.

Optical feedback in semiconductor lasers arises from the re-injection of part of the laser's own emitted radiation, through a mirror placed in front of its output facet, as schematically depicted in Fig. 2.1. As mentioned in Sec. 1.1, semiconductor lasers can be classified as Class-B lasers and therefore, they cannot show chaotic dynamics by themselves. However, when an external perturbation is applied, such as optical feedback, the degrees of freedom of the dynamical system increase and so, the laser can exhibit chaotic behavior. In practice and due to the fact that a photon needs a finite time to travel around the external cavity, the optical feedback is delayed. The delay dramatically increases the number of degrees of freedom and consequently the observed chaos is high-dimensional.

As mentioned above, Fig. 2.1 depicts the schematic setup for a semiconductor laser with optical feedback. The light emitted from the laser is reflected by an external mirror at a distance L_{ext} from the front edge of the laser, and fed back into the laser cavity after a delay time (τ). The external mirror is an ordinary mirror located within the coherence length of the laser field.

2.1.1 Rate equations for a semiconductor with feedback

In this section we are going to describe the rate equations for a semiconductor laser subject to optical feedback. To find those equations we are going to proceed as in

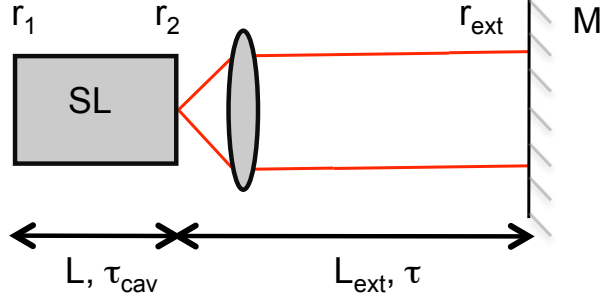


Figure 2.1: Scheme of the experimental setup of a semiconductor laser subject to an optical feedback. r_1 and r_2 are the reflectivities at the end-facets of the laser and r_{ext} is the reflectivity of the external mirror M . L and L_{ext} are the lengths of the laser cavity and external cavity, respectively. τ_{cav} is the time inverted by a photon to turn around the laser cavity, and τ is the time of flight of a photon around the external cavity.

the case of a solitary semiconductor laser described in Appendix A. Based on the theoretical work by Lang & Kobayashi (1980), the inclusion of an external mirror in front of a Fabry-Perot laser is nothing more than the addition of a delayed term to the standard laser field equation (Eq. 1.4). Then, the rate equation for the complex field $E(t)$ can be written as follows:

$$\begin{aligned} \frac{dE(t)}{dt} = & \frac{(1 + i\alpha)}{2} [G(N, |E|^2) - \gamma] E(t) + \\ & + \kappa_f E(t - \tau) \exp[-i\omega_0\tau] + \sqrt{2\beta N} \zeta(t), \end{aligned} \quad (2.1)$$

where κ_f is the feedback strength, $\tau = \frac{2L}{c}$ the round-trip of the light in the external cavity and ω_0 the free-running optical frequency of the laser. The second term in the right-hand side is the feedback term. The feedback strength can be derived by assuming that only one reflection in the external cavity has significance (i.e. the reflectivity of the external mirror is weak). We will also assume that the reflectivities for the front and back facets of the laser are the same (i.e. $r_1 = r_2 = r$). These assumptions imply some limitations on the applicability of the Lang-Kobayashi (LK)

model, due to the fact that the dynamics of a semiconductor laser subject to strong feedback can not be explained with these simplified model. Under these assumptions the feedback strength is:

$$\kappa_f = \frac{1 - r^2}{\tau_{cav}} \frac{r_{ext}}{r}, \quad (2.2)$$

where τ_{cav} is the time of flight of the light inside the laser cavity. It is worth to note that even for weak external reflectivities ($r_{ext} \sim 10\%$), the laser can easily show unstable oscillations. In practice, we can quantify the feedback strength by measuring the intensity threshold reduction as:

$$\frac{\Delta I_{th}}{I_{th}} = \frac{I_{th} - I_{th}^f}{I_{th}}, \quad (2.3)$$

where I_{th} and I_{th}^f are the threshold currents for the solitary and laser with feedback respectively. I_{th}^f has been estimated by measuring the intersection between the extrapolated spontaneous and stimulated emission lines, as we have done with the solitary laser (Sec. 1.4.1). In Fig. 2.2, we show the light-current curve for a semiconductor laser when the optical feedback is switched on and off. Note that the feedback implies a reduction on the lasing threshold.

The rate equation for the carrier density $N(t)$ can be described by the same equation as in the case of a solitary laser (Eq. 1.5) if we assume that the carrier density is not affected by the optical feedback. Therefore, the rate equations for the complex field and the carrier density obey the following expressions:

$$\begin{aligned} \frac{dE(t)}{dt} = & \frac{(1 + i\alpha)}{2} [G(N, |E|^2) - \gamma] E(t) + \\ & + \kappa_f E(t - \tau) \exp[-i\omega_0\tau] + \sqrt{2\beta N} \zeta(t), \end{aligned} \quad (2.4)$$

$$\frac{dN}{dt} = C - \gamma_e N - G(N, |E|^2) |E|^2. \quad (2.5)$$

Stationary lasing conditions can be obtained by imposing the electric field, $E(t)$, to be constant. As the electric field is complex, we will represent it in terms of its intensity $P(t) = |E|^2$ and its phase, $\phi(t)$. Assuming steady-state conditions,

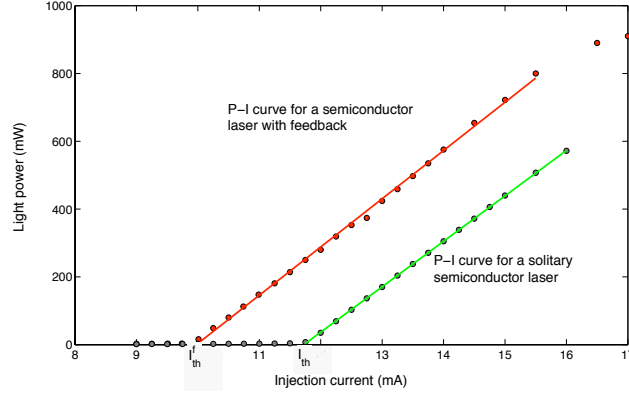


Figure 2.2: Schematic behavior of the laser power for increasing injection currents. The green line corresponds to the light-current curve for the solitary laser and the red line to the light-current curve for a laser with feedback.

$P(t) = P_s$, $N(t) = N_s$ and $\phi_s(t) = (\omega_s - \omega_{th})t$, one finds the following stationary solutions (Sano, 1994):

$$P_s = \frac{C - \gamma_e N_s}{g_N(N_s - N_{th})}, \quad (2.6)$$

$$N_s = N_{th} - \frac{2\kappa_f}{g_N} \cos(\omega_s \tau), \quad (2.7)$$

$$\Delta\omega\tau = (\omega_s - \omega_{th})\tau = \kappa_f \tau \sqrt{1 + \alpha^2} \sin(\omega_s \tau + \arctan(\alpha)). \quad (2.8)$$

By looking the evolution of the laser dynamics in the phase space defined by $(\omega\tau, N - N_{th})$, we obtain an ellipse that contains the steady-state solutions. The ellipse has the following expression:

$$\left[(\omega_s - \omega_{th})\tau + \frac{\alpha g_N \tau}{2} (N_s - N_{th}) \right]^2 + \left[\frac{g_N \tau}{2} (N_s - N_{th}) \right]^2 = \kappa_f^2. \quad (2.9)$$

In Fig. 2.3 we show the steady-state solutions in the $(\omega\tau, N - N_{th})$ space. The solutions, which appear in pairs, can be classified depending on their stability. By doing a linear stability analysis of the solutions, it is possible to distinguish between

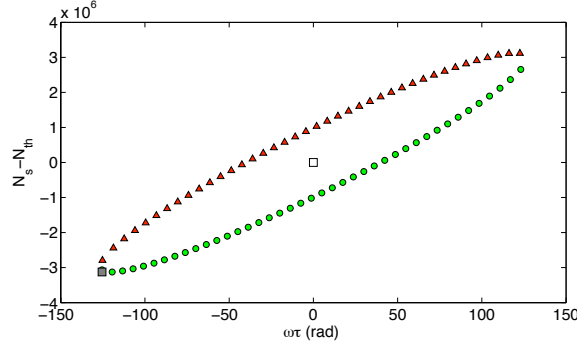


Figure 2.3: Steady-state solutions in the $(\omega\tau, N - N_{th})$ space for $\alpha = 3.0$, $\tau = 2.0$ ns and $\kappa_f = 0.02$ ps $^{-1}$. Note that solutions over the lower branch correspond to external cavity modes (green circles) and the solutions over the upper branch are saddle instabilities (red triangles). Filled square corresponds to the MGM and empty square to the stable emission without feedback.

stable and unstable solutions (Sano, 1994). The solutions lying on the upper branch of the ellipse (red triangles in the figure) are always unstable saddle-node solutions (called antimodes), due to the destructive interference between the field inside the laser and the feedback field. Solutions on the lower branch are either stable or unstable via a Hopf bifurcation. These solutions are called compound cavity modes. In this figure, we also show the maximum gain mode (MGM), that is located at the lower left corner of the ellipse. The MGM is always stable and corresponds to the regime of operation where the carrier density is minimum and the output power is maximum. The empty square, in the middle of the ellipse, corresponds to the stable solitary laser emission.

2.1.2 Regimes of optical feedback

There are multiple parameters to characterize, when studying the instabilities due to an external feedback. In this section, we will focus on the external feedback

strength (Tkach & Chraplyvy, 1986; Ohtsubo, 2002). Depending on the fraction of light being fed back into the laser, several effects can be observed. If the feedback is very small (less than 0.01%), the linewidth of the laser may become narrow for an adequate relative phase between the emitted and re-injected light. If we increase slightly the amount of feedback ($< 0.1\%$), external modes start to play a role and give rise to mode hopping among the internal and external cavity modes. For a yet higher amount of feedback $\sim 0.1\%$, mode hopping is suppressed and the laser oscillates with a very narrow linewidth. In the opposite limit of strong feedback ($> 10\%$), external cavity takes over and the laser behaves as if it had a single cavity, resulting in the laser oscillating once more with a single narrow longitudinal mode.

So far, we have enumerated the different effects for the extreme values of the feedback level, but in this Thesis we are mainly interested in moderate feedback effects. When the feedback fraction is around 1% the relaxation oscillations become undamped and the laser exhibits chaotic behavior. In this regime, the laser linewidth becomes broader.

The reason for our interest in the moderate feedback regime is that it is possible to observe a rich variety of dynamical regimes. From a technological point of view, it is also very interesting to understand how the system behaves under these conditions, since there are several applications in which the optical feedback plays an important role, such as DVD devices, velocimeters, etc... This regime can be described by the Lang-Kobayashi equations (Eq. 2.4 and 2.5). A possible classification for the different chaotic behaviors has been reported by Besnard et al. (1993) and Heil et al. (1998, 1999b). They distinguish between three main behaviors, depending on the pump current: stationary regime, low-frequency fluctuation regime (LFF) and coherence collapse regime (CC). It is worth to note that it is possible to observe coexistence between those regimes at the interfaces between their regions of existence in parameter space. In Fig. 2.4 Heil et al. (1999b) map the dynamics of a semiconductor laser subject to optical feedback in the parameter space formed by the injection current and the feedback strength.

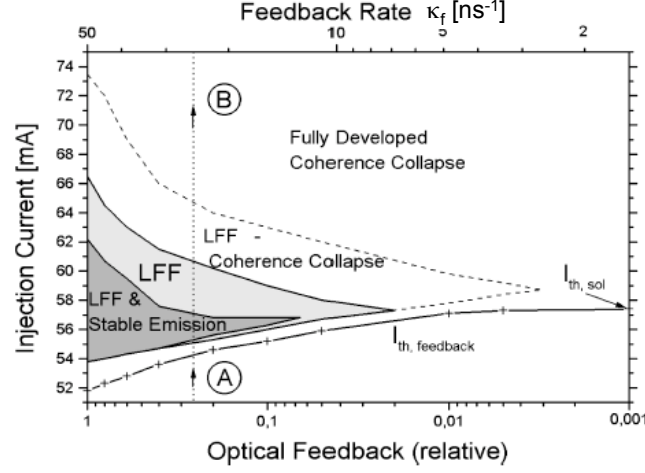


Figure 2.4: The possible dynamical regimes of a semiconductor laser subject to optical feedback in feedback κ_f -current I_p space are depicted. The LFF regime is depicted in light gray. The dark-gray region corresponds to the region of coexistence of the stable emission and the LFF state. The unshaded region delimited by the dashed line corresponds to the continuous transition between the LFF regime and the fully developed CC regime. From Heil et al. (1999b).

The Low-Frequency Fluctuation regime

A well-known feedback-induced instability is the regime of Low-Frequency Fluctuations (LFFs), which occurs for moderate feedback and near the lasing threshold. The LFFs consist in sudden power dropouts arising at irregular times, followed by gradual, stepwise recoveries, as can be seen in Fig. 2.5 (red line). The power dropouts are known to be actually a slow modulation (typically in range of ns to μ s) of fast picosecond pulses (Fischer et al., 1996), as depicted in Fig. 2.5(a) (black line). In practice, and due to the relatively small bandwidth of the detectors, we are only able to show the slower dynamics of the system, which for most of the results presented in this Thesis will be enough. A characteristic feature of LFFs is that, as the

laser bias current increases, the average time interval between consecutive dropouts decreases, and the dropouts become increasingly frequent and begin to merge (Heil et al., 1998). In Fig. 2.5(b), we show mean Inter-spike Interval $\langle T \rangle$ as a function of the injection current.

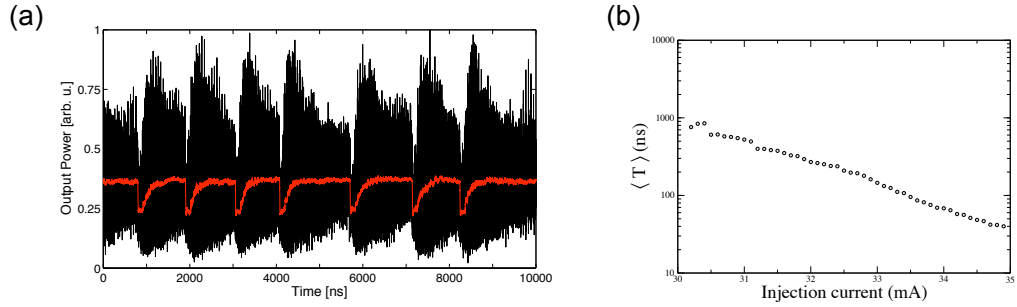


Figure 2.5: (a) Experimentally obtained LFF time series. Black line represents the fast dynamics and the red line the filtered output known as LFF's. (b) Average time interval between consecutive dropouts as a function of the pump current.

Two different explanations were initially proposed for the LFF phenomenon. In the first, the dropouts were stochastic events caused by spontaneous emission fluctuations (Henry & Kazarinov, 1986). In the second, the LFFs were considered to be an instance of chaotic dynamics (Mork et al., 1992), which was substantiated soon afterwards by Sano (1994), through an analysis of the LFF trajectories in phase space and their interaction with the many (unstable) fixed points of the delay-differential equation model that represents the dynamics of the system. A more detailed experimental and numerical investigation of the system revealed (Hohl et al., 1995; Lam et al., 2003) that both deterministic and stochastic mechanisms are necessary to explain the existence of LFFs, with noise being more important close the lasing threshold and chaos prevailing far from threshold. The chaotic itinerancy around external modes can be visualized in phase space by numerical calculations (Sano, 1994). In Fig. 2.6(a) the laser oscillates around the neighborhood of the MGM.

When the system is close enough to an anti-mode, a collision between the trajectory and the anti-mode can take place (more specifically, the state of the laser is trapped at one of the antimodes). As a result, the carrier density grows rapidly to the threshold of the solitary laser but keeping constant its phase. This rapid increase of the carriers induces a sudden increase of the phase towards the solitary laser behavior is achieved. The process related above is the power drop-out in the LFF's regime. After that, the laser trajectory begins to recover towards the MGM, becoming trapped around successive external cavity modes on its way, until reaching the neighborhood of the MGM. Around every cavity mode, the laser makes a few cycles, describing chaotic oscillations. The power dropout and the subsequent recovery process repeat again and again irregularly in time. As a result, LFFs are observed in the laser output oscillations as it is depicted in Fig. 2.6(b) and (d).

We now examine how this process changes when the pump current is varied. It is well known that the inter-dropout intervals decrease in duration when the pump current is increased (see Fig. 2.5(b)). By inspecting the trajectory in the $(\omega\tau, N - N_{th})$ space, one can see that when the pump current is increased, the amplitude of the chaotic itinerancy around the external cavity modes becomes larger, and thus it takes a shorter and shorter time to go through more external cavity modes and then collide with an "anti-mode" (as depicted in Fig. 2.6(c)). Lam et al. (2003) did the same study but they used the spontaneous emission noise as a parameter. They showed the same behavior in the phase space when the noise intensity was reduced. Therefore, and as mentioned above, we can conclude that for low pump currents, the noise plays an important role and the drop-outs are basically driven by noise, but for higher pump currents, the chaotic itinerancy itself can lead to deterministic collisions with antimodes, making the trajectory less sensitive to noise. In Ch. 6 and 7 we have systematically studied the degree of stochasticity on the time between dropouts for a laser with feedback as a function of the pump current.

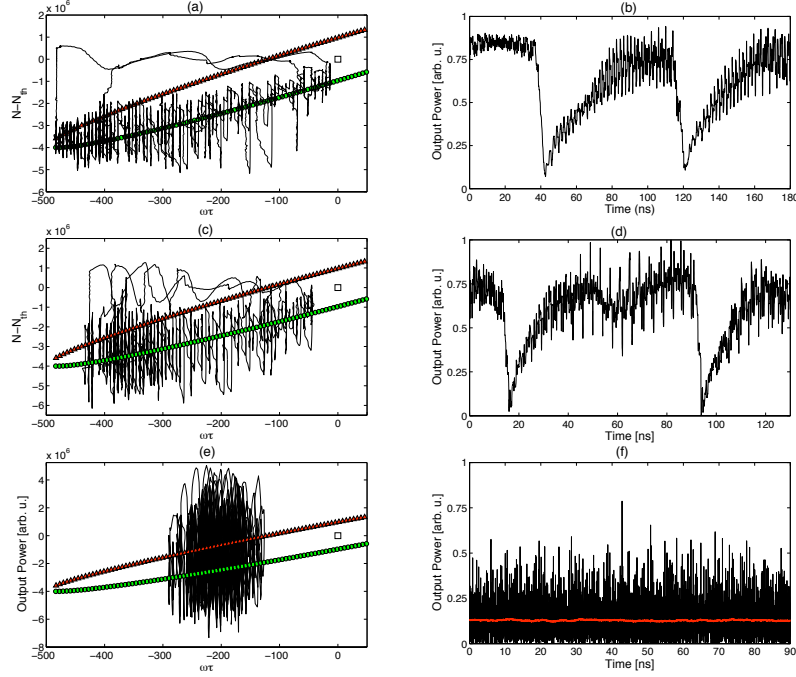


Figure 2.6: Numerically obtained chaotic itineracies around the external cavity modes (a), (c) and (e) and the corresponding LFF time series (b), (d) and (f) for three different values of the injection current. (a) and (b) correspond to $1.01 \times I_{th}$, (c) and (d) correspond to $1.05 \times I_{th}$, (e) and (f) correspond to $1.80 \times I_{th}$. Note the first two values of the pump current lead to the LFF regime and the last one to the CC regime.

The Coherence Collapse regime

By increasing more and more the injection current, the system enters into a regime called Coherence Collapse (CC), where the relaxation oscillations get excited due to feedback, and the spectral linewidth is increased up to ~ 25 GHz. A signature of this regime is that the trajectory is completely disordered and only the fast time scales of the system are retained (Mulet & Mirasso, 1999), as can be seen in Fig. 2.6(f). By inspecting the trajectory in phase space, the sudden dropouts in the output power merge, and only fully developed chaos can be observed. In the CC

regime we still have the stationary solutions of the ellipse, but now the trajectory is governed by a new chaotic attractor, instead of the modes and anti-modes of the ellipse (Fig. 2.6(e)). This regime has been identified as a high-dimensional chaotic dynamics (Ohtsubo, 2002; Masoller, 1997b). The high dimensionality comes from the delay time associated with optical feedback, is due to the finite flight time of the light in the external cavity. The CC regime has been studied in the past employing well-known techniques such as those based on Poincare Sections, Lyapunov exponents and fractal dimensions (Masoller, 1997b; Mork et al., 1992; Ahlers et al., 1998).

2.2 Pump current modulation

So far, we have discussed how a semiconductor laser behaves when its own light is re-injected. In this section, we study the power emission behavior when the laser is subject to a current modulation (see Fig. 2.7). As mentioned in Sec. 2.1, we need at least an extra degree of freedom to induce chaos in a semiconductor laser. The easiest way to introduce more degrees of freedom by using the injection current is to modulate it periodically with a frequency ω_{mod} .

In this case, the term C in Eq. 2.5 has to be replaced by $C_{DC} + C_{mod}$, where C_{DC} is a constant pump current and $C_{mod} = C_0 \cos(\omega_{mod} t)$. Therefore, the equations for the electric field and the carriers have the following form:

$$\begin{aligned} \frac{dE(t)}{dt} &= \frac{(1 + i\alpha)}{2} [G(N, |E|^2) - \gamma] E(t) + \sqrt{2\beta N} \zeta(t), \\ \frac{dN}{dt} &= C_{DC} + C_0 \cos(\omega_{mod} t) - \gamma_e N - G(N, |E|^2) |E|^2. \end{aligned} \quad (2.10)$$

A detailed analysis of these equations, as as the one performed by Sacher et al. (1992), points out that for frequencies $\omega_{mod} \sim \omega_{RO}$ (ω_{RO} is the relaxation oscillation frequency), a period doubling can be observed. If the modulation frequency is further increased, a period doubling route to chaos takes place (Lee et al., 1985). On

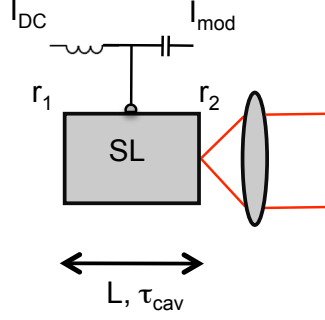


Figure 2.7: Scheme of the experimental setup of a semiconductor laser subject to external pump modulation. r_1 and r_2 are the reflectivities at the end facets of the laser cavity. L is the length of the laser cavity and τ_{cav} is the internal round-trip time.

the other hand, if the modulation frequency (ω_{mod}) is equal or a rational fraction ($\frac{\omega_{mod}}{\omega_{cav}} = p/q$) of the internal round-trip frequency ($\omega_{cav} = \frac{2\pi}{\tau_{cav}}$), quasiperiodicity and frequency locking (a detailed explanation of locking phenomena is given in Chapter 3) can arise. In this situation, the system is characterized by two time scales corresponding to the modulation frequency and the internal round-trip frequency. When both frequencies are exactly the same or have a rational ratio, the trajectory in the phase space lies in a closed curve on a two-dimensional torus (i.e. periodic output) and short optical pulses are generated (active mode locking) (Fig. 2.8(a)). On the other hand, when the ratio between the frequencies is irrational, the trajectory lies in a never-closing curve (i.e. quasiperiodic output) (Fig. 2.8(b)).

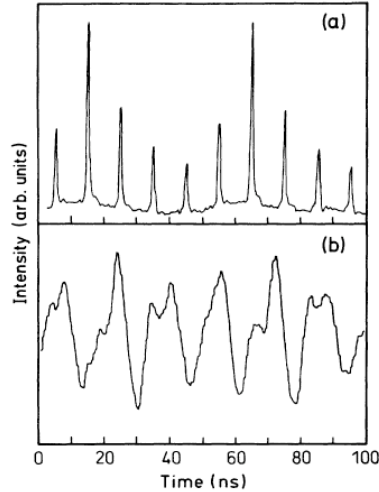


Figure 2.8: (a) Frequency-locked output of the laser cavity with the modulation frequency. The frequency ratio is chosen to be rational and equal to $\frac{\omega_{mod}}{\omega_{cav}} = 2/5$. Under these conditions, the laser shows a periodic pulsed activity. (b) Quasi-periodic output when the frequency ratio is chosen to be irrational and set to the golden-mean value $\sigma_g = 0.61803$. From Sacher et al. (1992).

2.3 Pump current modulation and optical feedback

Finally, we will consider the situation in which the semiconductor laser is subject to a delayed feedback and modulation of its pump current (Fig. 2.9). An early study of a semiconductor laser with feedback subject to an external modulation was made by Takiguchi et al. (1998), where they introduced a sinusoidal signal in order to entrain the dropouts. Similar situations were considered by Sukow & Gauthier (2000) and Buldú et al. (2003).

This setup has been used in the past to show that semiconductor lasers with feedback exhibit excitability properties (Giudici et al., 1997). In order to prove that a system is excitable, three conditions (at least) must to be satisfied: first, the existence of a threshold above which an excitation can occur; second, the form and size of the response must be invariant to any change in the magnitude of the perturbation and third, a refractory time must exist. In Giudici et al. (1997) and Sukow & Gauthier (2000), a perturbation in the pump current applied in the laser with feed-

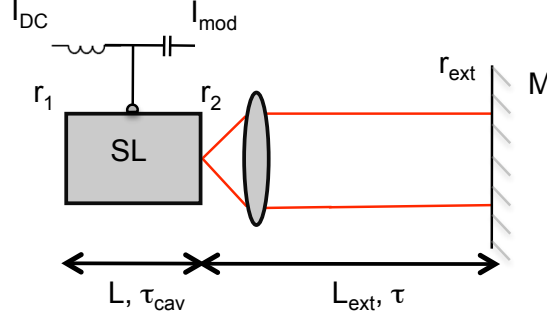


Figure 2.9: Scheme of the experimental setup of a semiconductor laser subject to an external pump modulation and optical feedback.

back was seen to generate power dropouts that were independent of the modulation properties. Heil et al. (1999b) and Mulet & Mirasso (1999) revealed the existence of a refractory time during which the next dropout cannot occur. Marino et al. (2002) and Buldú et al. (2002) showed that when the system is driven by a weak periodic signal, a certain amount of noise can help the system to follow the frequency of this signal. This resonance-like behavior is known as stochastic resonance (SR). Furthermore, it was also shown that this system can exhibit coherence resonance (CR), when the system is modulated by noise instead of a sinusoidal signal (Giacomelli et al., 2000; Buldú et al., 2001). When an external noise is introduced in the pump current of the laser with feedback, an increase of regularity in the dropout events occurs for an optimal noise level (i.e. CR takes place).

As mentioned above, in this Thesis we study the degree of stochasticity of the time between dropouts by using different statistical techniques. We also show that a laser with feedback subject to a constant pumping signal (DC signal) can exhibit non zero correlations for sufficiently high pumping amplitudes. In Ch. 5 we study the response of an excitable laser subject to a random dichotomous modulation on its pump current in order to shed light into the emergence of these correlations.

Chapter 3

Dynamics of coupled semiconductor lasers

3.1 Synchronization

Synchronization phenomena are present in many fields such as physics (Bennett et al., 2002; Feng et al., 2010), life science (Strogatz & Stewart, 1993) and many others. Synchronization can be observed in systems as diverse as pendulum clocks, firing neurons, fireflies, social networks, etc... Synchronization has been investigated since the earliest days of modern physics. Christian Huygens was one of the first physicists that approached the study of synchronization. Huygens, in collaboration with Alexander Bruce, constructed maritime pendulum clocks in order to guarantee timing with sufficient accuracy to determine longitude reliably during a sea travel. During their investigation they realized that when he suspended two pendulum clocks in the same wooden beam, each pendulum swung at exactly the same frequency, and 180° out of phase with respect to one another. Finally, Huygens could not solve the longitude problem (due to so slight and almost insensible motion was able to cause an alteration in their periodic oscillations), but synchronization

observations have served to inspire the study of sympathetic rhythms of interacting nonlinear oscillators in many areas of science.

The origin of the word synchronization comes from the greek root $\sigma\psi\nu$ (*syn*) that means *same* and $\chi\rho\nu\nu\omicron\varsigma$ (*kronos*) that means *time*. In direct translation, “synchronous”, means “occurring at the same time”. A modern definition of synchronization could be an “*adjustment of rhythms of oscillating objects, due to their weak interaction*” as appears in PhD Thesis of Vicente (2006).

3.1.1 Phase and frequency locking

In this Section, we analyze the conditions leading to frequency and phase locking between two coupled nonlinear oscillators. As we will show in Sect. 3.1.3, synchronization can be achieved between two oscillators even when they are not identical.

For simplicity, we will focus on an harmonically driven quasilinear oscillator and finally, we will generalize the argumentation to two coupled semiconductor lasers. As usual a quasilinear oscillator is represented by the expression, $x(t) = A \sin(\phi(t))$, with $\phi(t) = \omega_0 t + \phi_0$. In order to study the effects of the coupling and detuning on synchronization, it is useful to work on a reference frame that rotates with the frequency of one of the nonlinear oscillators (Pikovsky et al., 2001). Note that an observer lying in the rotating reference frame sees an harmonic oscillator (i.e. $x(t) = A \sin(\omega t + \phi_0)$) as a resting phase point. In a phasor representation, sustained harmonic oscillations correspond to a fixed point with the polar coordinates A and $\phi_0 = \phi(t) - \omega t$ in this new reference frame. Similarly we define the forcing by $F(t) = \epsilon \cos(\phi_e(t))$, with $\phi_e(t) = \omega t + \phi_{e,0}$. As shown in Fig. 3.1(a), an harmonically driven quasilinear oscillator, with a forcing strength $\epsilon \rightarrow 0$ and a given detuning $\Delta\omega = \omega_0 - \omega$, corresponds to a rotation of the phase point with angular velocity $\Delta\omega$ in the rotating frame (here we choose the rotating frame to have the frequency ω of the forcing). This phase dynamics can also be represented by means of a particle sliding with constant velocity along a tilted potential plane, as shown in Fig. 3.1(c).

In the particular case of zero-detuning the phase remains at some arbitrary point on the cycle with no angular velocity (Fig. 3.1(b)).

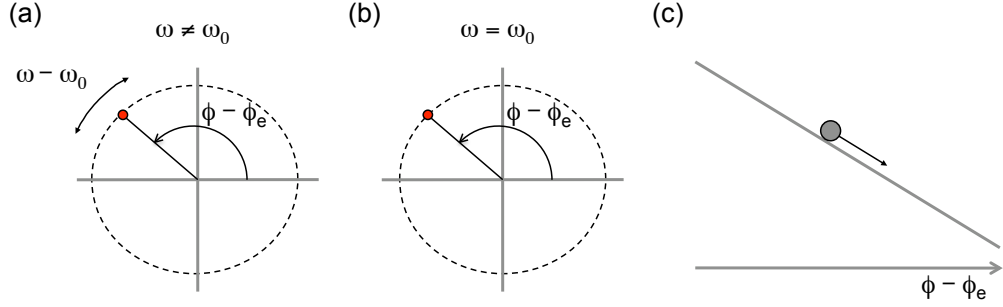


Figure 3.1: In the reference frame rotating with ω , the limit cycle oscillation corresponds to a rotating point that depends on the detuning $\omega_0 - \omega$ (a) and to a fix point in the case of zero detuning (b). The position of the point is characterized by the phase difference $\phi - \phi_e$. Panel (c) shows a particle falling down a tilted plane with constant velocity, which illustrates the phase dynamics in the rotating frame. ϕ is the phase of the oscillator and ϕ_e is the phase of the forcing. Based on Pikovsky et al. (2001).

We now apply a non-zero force (i.e. $\epsilon \neq 0$). The force defined above is represented, in the rotating frame, by a constant vector of length ϵ acting at some phase ϕ^0 . The angle ϕ^0 depends on the initial phase of the force $\phi_{e,0}$, and for quasilinear oscillators $\phi^0 = \phi_e(t) - \phi(t) = \phi_{e,0} + \pi/2$ (Pikovsky et al., 2001). Under weakly forcing, the oscillator amplitude A is invariant respect to the non-forced scenario but the phase is influenced by the forcing. A weak force in resonance ($\Delta\omega = 0$) with the autonomous oscillator creates two equilibrium points, one stable and one unstable on the cycle. The effect of the force depends on the phase difference. When the force acts in the radial direction, it cannot shift the phase along the circle (points 1 and 2 in Fig. 3.2(a)), but when the force is tangent to the circle then the phase shift is maximal (points 3 and 4 in Fig. 3.2(a)). If we move away from point 1, the phase shift due to the force pushes us towards to this point, which makes it a stable point. On the other hand, point 2 is an unstable point, since the effect of the force in its

neighborhood propels the phase point away from it. Therefore, the external force creates an stable equilibrium position at point 1 (phase locking) and an unstable equilibrium position at point 2.

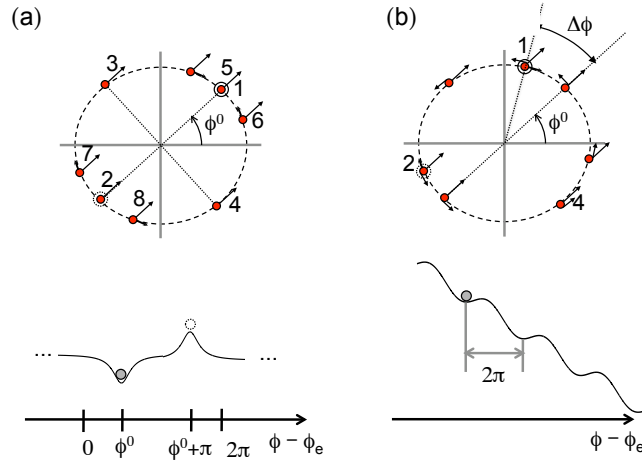


Figure 3.2: (a) A weak external force cannot influence the amplitude of the limit cycle but can shift the phase of the oscillator. The external force creates a stable equilibrium point when acting in the radial direction only. (b) In the presence of a small detuning the phase point rotates due to the detuned external force. The phase point is stopped by the force and a stable phase shift $\Delta\phi$ is maintained. The external force creates a minimum in the tilted phase potential. Based on Pikovsky et al. (2001).

Finally we can merge the effects of the detuning and forcing to show the complete forced oscillator scenario. As shown in Figure 3.2(b), the effect of the force counteracts the detuning. While the force pushes the phase point to the minimum of the potential, the detuning rotates the phase with angular velocity equal to $\omega - \omega_0$. That means, for a particular value of the phase shift ($\phi^0 + \Delta\phi$, where ϕ^0 is the phase shift corresponding to the forcing and $\Delta\phi$ is the angle where the phase point is stopped due to the combined effect of the detuning and the forcing), the force balances the rotation and the phase point stops. It is worth to note that for a large

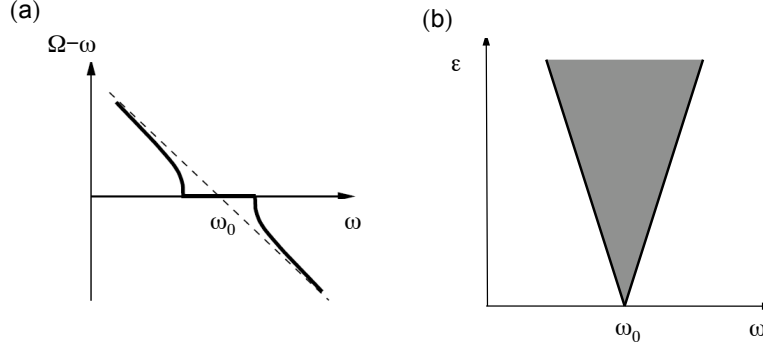


Figure 3.3: (a) Frequency difference vs forcing frequency curve for a given interaction strength. $\Omega - \omega$ represents the frequency difference between the forced and the unforced system. (b) Arnold tongue for a forced periodic oscillator. Based on Pikovsky et al. (2001).

detuning, it could be possible to never find a force capable of stopping the rotation.

Once we have examined the effects of detuning and forcing on the synchronization, we are able to define the phenomena of the frequency locking and phase locking.

Frequency locking

Imagine an oscillatory system with frequency ω_0 forced by an external oscillator with frequency ω , which exhibit a mismatch between their natural frequencies (i.e with a detuning $\Delta\omega = \omega_0 - \omega$). For sufficiently small detuning the external force entrains the oscillator, therefore, the frequency of the forced oscillator Ω becomes equal to the frequency of the forcing ω . On the other hand, a weak coupling strength can only induce small changes in the frequency of the oscillators, and hence, there should be a critical detuning beyond which the frequency matching cannot be possible. The conjugation of these two effects leads to the appearance of a plateau in the $\Delta\Omega = \Omega - \omega$ vs ω curve, for a given force amplitude (ϵ), as shown in Fig. 3.3(a). The identity of the frequencies that holds within a finite range of the detuning is the hallmark of synchronization and is often called **frequency locking**. For each

value of the forcing amplitude we can find a region where the frequency locking is achieved, and thus we can determine a region in the (ω, ϵ) plane where the force and the oscillator are synchronized (Fig. 3.3(b)). This region is called synchronization region or Arnold tongue.

Phase locking

As we have shown, when an oscillator is not locked in frequency with the forcing, the phase difference increases with time. Therefore, in the synchronous state there exists a constant (or bounded) phase shift between the phases of the oscillator and the force:

$$\phi(t) - \phi_e(t) = \phi^0 + \Delta\phi = \text{constant}. \quad (3.1)$$

It is worth to note that the phase difference $\Delta\phi$ is zero (or π) only at zero detuning. For non-zero detuning the phase difference is not exactly zero as we have seen in Fig. 3.2.

As mentioned above, usually in the synchronous state, the phase and the frequency remain locked, but recent investigations (Thévenin et al., 2011) have shown the existence of a synchronization region beyond the Arnold tongue boundary, where it is possible to observe frequency locking without phase locking. In this region the phase dynamics remains bounded (i.e. $-\pi < \Delta\phi < \pi$) but not constant, while the average frequencies are locked. This phenomenon can be observed in sufficient complex systems, such as Class-B lasers. The intermediate regime between phase locking and phase shift is called phase entrainment regime (Chakraborty & Rand, 1988).

3.1.2 Synchronization of two oscillators

In this section, we are going to extrapolate the ideas presented in the previous section to two coupled oscillators instead of a single forced oscillator. Generally,

the interaction between two systems can be non-symmetrical, and so the action of one of the coupling directions can be stronger than the other. In this case, we can recover the results for the case of an external forced oscillator, showed above. As we have seen, in this scheme, the frequency of the driven oscillator is entrained by the forcing, but when the coupling strength of both oscillators is similar (bidirectional coupling), the frequencies of both systems changes in a non-trivial manner. We can denote the frequencies of the isolated systems as ω_1 and ω_2 with, $\omega_1 < \omega_2$ without loss of generality, and the frequencies of the coupled systems as Ω_1 and Ω_2 . The locking frequency typically lies in between of the two autonomous frequencies (i.e. $\omega_1 < \Omega < \omega_2$ with $\Omega_1 = \Omega_2 = \Omega$). The coupling between identical systems leads, in general, to a phase-attractive or phase-repulsive synchronization. The shift between phases is determined by the coupling strength and the detuning. One of the simplest mathematical models that describes the dynamics of the phase difference between two weakly coupled oscillators, with constant amplitude, is given by the Adler equation (Adler, 1946):

$$\frac{d\Delta\phi}{dt} = \Delta f \pm \kappa \sin(\Delta\phi), \quad (3.2)$$

where κ and Δf are the coupling strength and detuning, respectively. Using the same argument as for the case of an externally forced oscillator (see Fig. 3.2), the detuning makes the phase difference not exactly zero or even non-stationary. The loss of synchronization can be understood as a disappearance of the local minima in the tilted potential (Fig. 3.2). In Fig. 3.4 we show the phase difference dynamics for different values of the detuning between the oscillators and keeping constant the coupling strength ($\kappa = 1.00 \ t_{steps}^{-1}$, with t_{steps} being the integration time step used to compute the phase difference dynamics). In Fig. 3.4(a) we set the detuning $\Delta f = 0.00 \ t_{steps}^{-1}$ (the system lies in the very center of the Arnold tongue) and the phase difference remains equal to zero. In Fig. 3.4(b) we set $\Delta f = \kappa = 1.00 \ t_{steps}^{-1}$ and the phase grows asymptotically to $\pi/2$. In this situation the system lies on the border of the Arnold tongue but the phase is still locked. In Fig. 3.4(c) we slightly

increase the detuning, $\Delta f = 1.01 t_{steps}^{-1}$, and the dynamics of the phase difference is intermittent, which means that the system exhibits rapid phase jumps followed by epochs of synchronous behavior. In this case the system lies out of the Arnold tongue but very close to its border. With further increases in detuning, $\Delta f = 10.00 t_{steps}^{-1}$, the duration of the epochs of synchronous behavior becomes smaller, and eventually the growth of the phase difference becomes almost uniform (Fig. 3.4(d)).

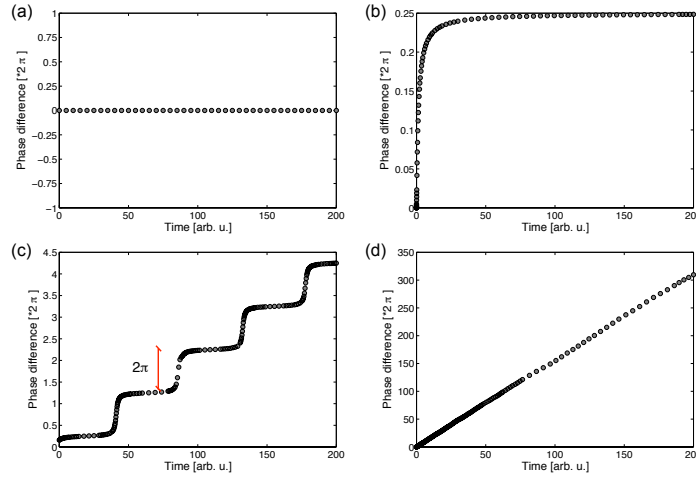


Figure 3.4: Phase difference for different values of the detuning and a constant coupling strength, $\kappa = 1.00 t_{steps}^{-1}$. (a) $\Delta f = 0.00 t_{steps}^{-1}$, (b) $\Delta f = 1.00 t_{steps}^{-1}$, (c) $\Delta f = 1.01 t_{steps}^{-1}$ and (d) $\Delta f = 10.00 t_{steps}^{-1}$.

3.1.2.1 Synchronization of chaotic oscillators

So far, we have pointed out how periodic oscillators can synchronize due to either an external force or the presence of another oscillator. Next we will focus on chaotic oscillators, since the results presented throughout the Thesis deal with these type of systems (i.e. a semiconductor lasers in the presence of either an external modulation or an optical feedback behaves chaotically in time for a wide range of parameters, as

presented in Ch. 2). Due to the irregularity of chaotic oscillators, it is not possible to define the phase and frequency as in the case of periodic oscillations, but one can define the instantaneous frequency of the chaotic system by using the Poincaré approach or the Hilbert approach. The Poincaré approach consists in constructing a Poincaré map and determine the times between successive crossings of the Poincaré surface. Each interval between crossing times can be considered as the instantaneous period of the oscillation, and therefore the inverse is the instantaneous frequency. We can estimate the mean frequency as follows:

$$\langle \omega \rangle = 2\pi N / \Delta T, \quad (3.3)$$

where N is an integer that counts how many times the Poincaré surface has been crossed in a given ΔT .

From the Hilbert approach, we can obtain the instantaneous phase of any real signal $s(t)$ from the discrete-time analytic signal (Gabor, 1946):

$$\psi(t) = s(t) + i\tilde{s}(t) = A(t)e^{i\phi(t)}, \quad (3.4)$$

with $\phi(t)$ and $A(t)$ being the Hilbert phase and Hilbert amplitude of the signal, respectively. The imaginary part of the analytic signal is the Hilbert transform $\tilde{s}(t) = \pi^{-1} P.V. \int_{-\infty}^{+\infty} \frac{s(\tau)}{t-\tau} d\tau$. Note that the phase $\phi(t)$ describes changes in the field envelope. From the Hilbert phase one can deriving the frequency with a simple time derivative.

3.1.3 Kinds of synchronization

The first investigations of synchronization phenomena were mainly focused on periodic systems, while recently the search for synchronization has turned to chaotic systems. Early experimental evidences on chaos synchronization were performed by Afraimovich et al. (1986) and Pecora & Carroll (1990) in chaotic circuits. When two or more chaotic elements are coupled, many interesting kinds of synchronization

can be found, including complete or identical synchronization, generalized synchronization, phase and lag synchronization, and intermittent lag synchronization. We will now describe these different kinds of synchronization.

3.1.3.1 Complete synchronization

Complete synchronization is the simplest form of synchronization, and consists in a perfect matching of the trajectories between two or more identical chaotic systems in time. In Fig. 3.5(a) we show the experimental time traces for two bidirectionally coupled lasers with cross-feedback (acting as a passive relay) exhibiting complete synchronization. As depicted in Fig. 3.5(b), the correlation plot between the two laser outputs shows a substantial linear correlation between the two laser outputs.

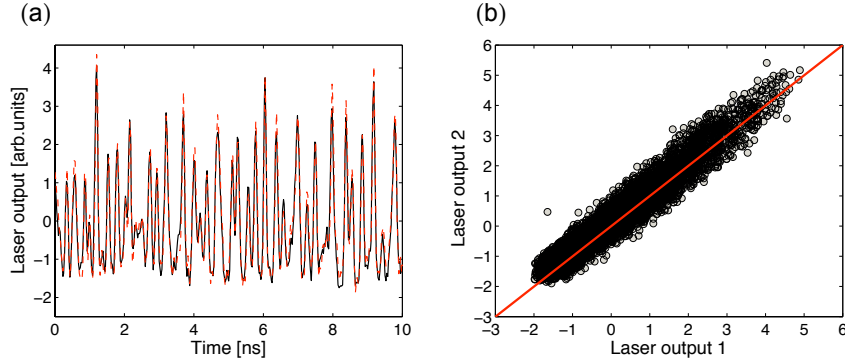


Figure 3.5: (a) Time traces for two mutually coupled semiconductor lasers (see Ch. 10 below) exhibiting complete synchronization. (b) Correlation plot between the two outputs.

This kind of synchronization can be observed in systems, which the coupling time is assumed to be zero (or much smaller than the system dynamics time scale) or systems which have a finite coupling time but show isochronal behavior. This latter case is often called zero-lag synchronization.

3.1.3.2 Generalized synchronization

When the oscillators are not identical they cannot synchronize identically. Under certain conditions, however, they can synchronize in a generalized way if there exists a transformation $f : \mathbf{X} \rightarrow \mathbf{Y}$ that relates the trajectories of the attractor in \mathbf{X} space into the trajectories of the attractor in the \mathbf{Y} space, with \mathbf{X} and \mathbf{Y} denoting the phase spaces of two oscillators. In that case:

$$y(t) = f(x(t)), \quad (3.5)$$

where $x(t)$ and $y(t)$ are the state variables of the two oscillators. Note that complete synchronization is a particular case of generalized synchronization (for $f(x(t)) = x(t)$). As one can expect from Eq. (3.5), non-trivial relations between coupled signals can appear. In order to measure the degree of synchronization between coupled systems, the auxiliary system method has been suggested for detecting generalized synchronization (Abarbanel et al., 1996). This method is used when two systems are coupled unidirectionally (i.e. drive-response system). The method consists in applying the same driving to two identical systems (or to the same system but in different experiments), known as replicas. If the replicas show linear correlations, the driving and the response are synchronized in generalized manner.

Figure 3.6(a) shows the time traces for the driving and the two replicas for a laser-diode-pumped Nd:YAG microchip laser (Uchida et al., 2003). In that paper they used the same laser as a driver and replicas. They stored a waveform and then re-injected into the system by using an arbitrary waveform generator. The driving and response systems did not exhibit correlations between them (Fig. 3.6(b)), but linear correlations appear between the replicas (Fig. 3.6(c)), indicating that the two instances of the chaotic oscillator are synchronized in a generalized manner.

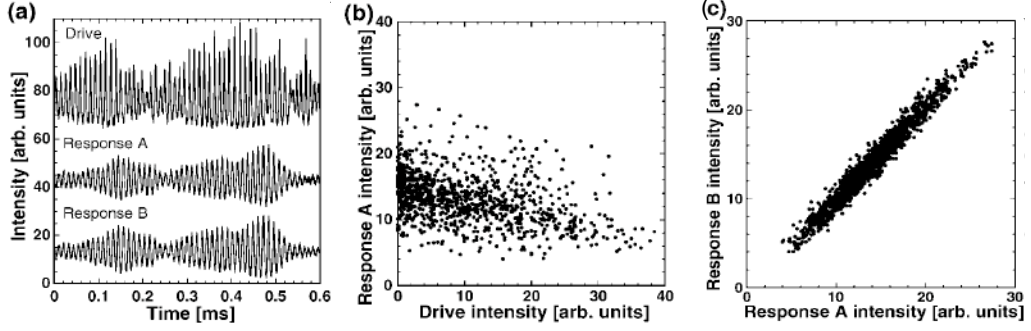


Figure 3.6: (a) Temporal waveforms of experimentally measured total intensity of the drive (Nd:YAG microchip laser with optoelectronic feedback) and two response systems. (b) Correlation plot between the drive and response outputs. (c) Correlation plot between the two response outputs. From Uchida et al. (2003)

3.1.3.3 Phase synchronization

Two chaotic systems are phase-synchronized when locking between the phases is achieved, regardless of the correlation between the amplitudes. Figure 3.7(a) shows the time traces for two diffusely coupled Rössler systems. For the parameters used in this simulation, the systems are phase locked (i.e. phase synchronization) but the Hilbert amplitudes are uncorrelated, as can be seen in Fig. 3.7(b). Note that in order to determine the phase and the amplitude of an arbitrary signal, we have used the general approach based on discrete-time analytic signal (Gabor, 1946) described in Sec.3.1.2.1.

3.1.3.4 Lag synchronization

Lag synchronization is a type of generalized synchronization with the particularity that trajectories of the attractor in \mathbf{X} space are related with those \mathbf{Y} space after a

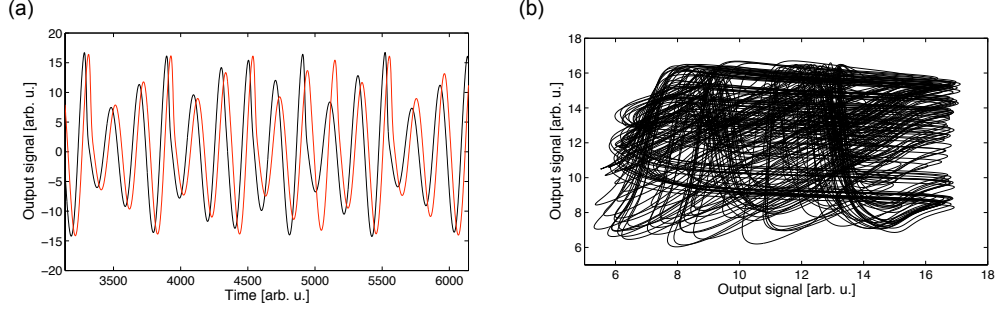


Figure 3.7: Adapted from (Rosenblum et al., 1996). (a) Temporal series of numerically obtained output signal for two coupled Rössler systems. (b) Correlation plot for the two Hilbert amplitudes showing an uncorrelated behavior.

lag time τ :

$$y(t) = f(x(t - \tau)), \quad (3.6)$$

where τ is the time needed by the first system to interact with the second one. The particular case $f(x) = x$ can be called identical lag synchronization.

Figure 3.8(a) shows the output intensity for two bidirectionally coupled lasers displaying lag synchronization. Note that one of the lasers leads the dynamics and the other laser follows with a certain delay τ . In Fig. 3.8(b) we show a histogram for the difference between corresponding dropout times. A peak appears at the delay time of $\sim 25ns$.

An interesting feature of this type of synchronization is the fact that, depending on the delays of the coupled system, the system can show zero lag synchronization (Englert et al., 2010) (there is coincidence without delay between the signals of the systems) and even anticipated (in a drive-response system, the response system leads the dynamics) (Masoller, 2001). This phenomenon can also occur intermittently, that means, the systems are most of the time verifying the condition for lag synchronization, but once in a while, they desynchronize.

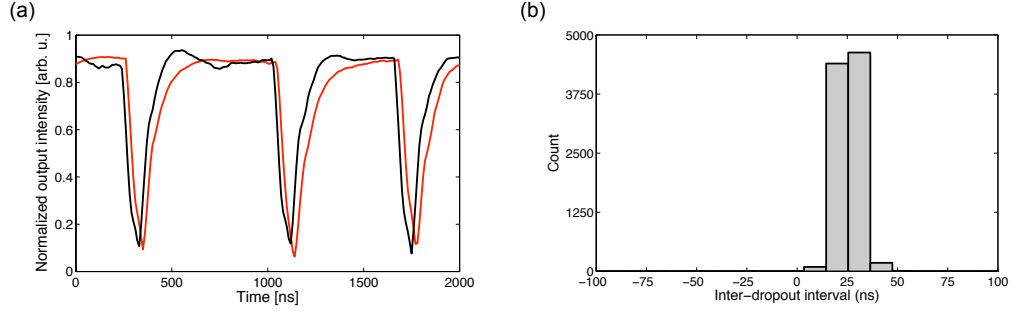


Figure 3.8: (a) Experimental output intensities and the corresponding histogram of the time between synchronized dropouts (b), for two bidirectionally coupled lasers.

3.2 Synchronization in coupled semiconductor lasers

As mentioned in Ch. 2, semiconductor lasers can exhibit chaotic behavior under the presence of external perturbations. We have also shown in Sec. 3.1.2.1 that chaotic systems can synchronize. Therefore, a characteristic of semiconductor lasers that makes them highly attractive for dynamical system studies, is the natural manner in which they can be coupled to one another, forming networks of interacting dynamical elements. Coupling can be accomplished optoelectronically, by modulating the pump current of a laser with the electrical signal of a photodetector that measures the light emitted by another laser (Larger et al., 1998; Kim et al., 2005; Illing et al., 2011), or more simply in a purely optical manner, by injection (coherent or incoherent) of a laser's output light into another (Mirasso et al., 1996; Sivaprakasam & Shore, 1999; Fischer et al., 2000). Given the fast temporal scales (on the order of picoseconds) with which semiconductor lasers operate, the time taken by the coupling signals to travel between the lasers (typically larger than nanoseconds) cannot be usually ignored, and thus interacting lasers become instances of *delay-coupled* dynamical systems (Schuster & Wagner, 1989). Within that context, two unidirectionally coupled lasers in which the light emitted by one laser is injected into the other, readily synchronize their dynamics with a time lag equal to the coupling delay

time, in such a way that the emitting laser leads over the receiver (Takiguchi et al., 1999)

For more than a decade semiconductor lasers have been used as model system for chaos synchronization. We now present an overview of chaos synchronization phenomena between coupled semiconductor lasers in different coupling setups.

3.2.1 Unidirectional injection in a semiconductor lasers

One of the most typical coupling architectures between two semiconductor lasers is unidirectional injection. It consists in optically injecting the output field of one laser into the other one. In this architecture, the driving laser acts usually as a transmitter of the dynamics and the other laser is the receiver and uniquely follows the emitter with a certain time delay. This corresponds to what is known as a leader-laggard behavior, in which the emitter laser leads the dynamics a time equal to the coupling time between the two lasers.

In what follows we are going to discuss the most common coupling architectures in unidirectionally coupled lasers.

3.2.1.1 Types of configurations

The most common coupling architectures in unidirectionally coupled lasers are the open loop and closed loop configurations. In the open loop configuration (Fig. 3.9(a)), only the emitter (i.e. driving) laser has optical feedback. On the other hand, on the closed loop configuration both lasers have their own feedback (Fig. 3.9(b)). In the open loop configuration, depending on the relation between time delays and coupling and feedback strengths, different synchronization phenomena can be observed.

Figure 3.10 shows an overview of different synchronization regimes that can be seen between two unidirectionally coupled lasers, in terms of the cross-correlation function (see Appendix B) between the time series of the light emitted by the two

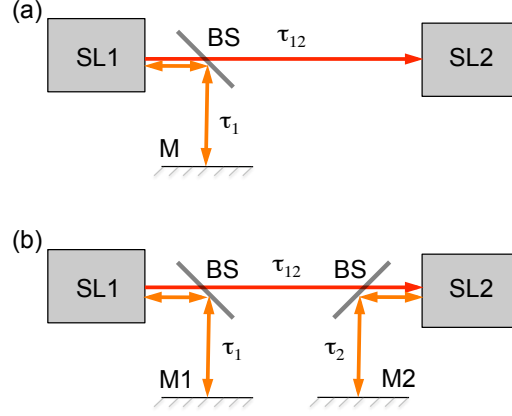


Figure 3.9: Unidirectionally coupled lasers in an open loop (a) and closed loop configuration (b). SL: semiconductor lasers, BS: beam splitters M: mirrors. τ_{12} is the coupling time between SL1 and SL2 and τ_i is the feedback time for each SL.

lasers. As shown in that panel (a) of that figure, when the time delays corresponding to the feedback (τ_1) and the coupling (τ_{12}), and also the feedback (κ_1) and coupling (κ_{12}) strengths are chosen to be the same, identical synchronization is observed (i.e. $I_2(t) = I_1(t)$). On the other hand, as shown in Fig. 3.10(b), when the delay times are different, $\tau_1 \neq \tau_{12}$ and $\kappa_{12} > \kappa_1$, the outputs show a leader-laggard behavior (i.e. $I_2(t) = aI_1(t - \tau_{12})$). Note that in this case, there is no perfect matching between the outputs of the two lasers, due to the fact that the re-injected power in both lasers (coming from itself in the case of the emitter, and from the other laser in the case of the receiver) is not the same. From an experimental point of view, this is the easiest configuration to achieve synchronization, due to the fact that it is not necessary to chose all the parameters to be carefully matched between emitter and receiver.

Finally, when the coupling strengths coincide but the delay time does not, anticipated or retarded synchronization takes place (i.e. $I_2(t) = I_1(t - \Delta\tau)$ with $\Delta\tau = \tau_{12} - \tau_1$). The synchronization will be anticipated or retarded synchronization

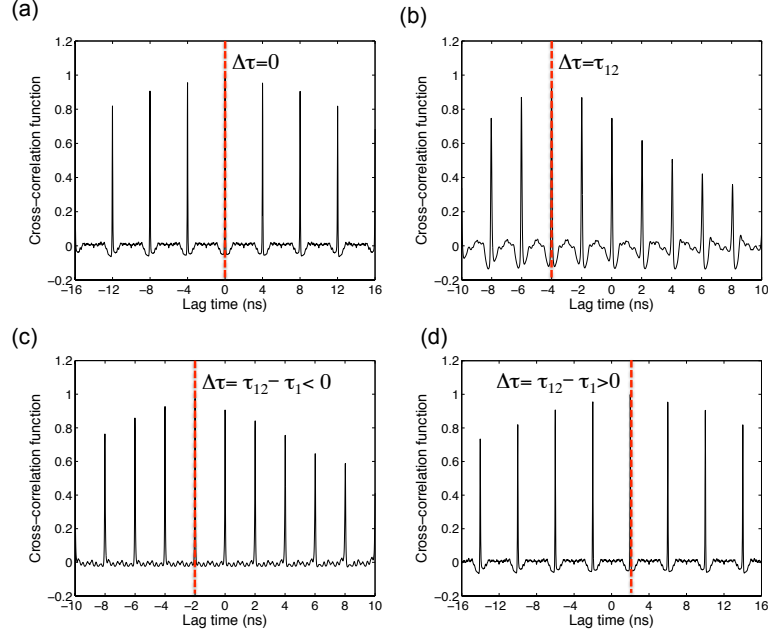


Figure 3.10: Cross-correlation function for different relations between delay times and coupling strengths, for an open loop configuration. (a) identical synchronization appears for $k_1 = k_{12}$ and $\tau_1 = \tau_{12}$. (b) Lag synchronization at $\Delta\tau = \tau_{12}$ is achieved when $\kappa_{12} > \kappa_1$. When coupling strengths are equal ($\kappa_{12} = \kappa_1$) but the delay times are different, retarded (c) and anticipated (d) synchronization appear with $\Delta\tau = \tau_{12} - \tau_1$. Red dashed line indicates the maximum of the cross correlation.

depending on the sign of $\Delta\tau$. In Fig. 3.10(c,d), we show retarded and anticipated synchronization respectively. In Ch. 9 we will discuss how two systems in an open loop configuration synchronize under the presence of two coupling paths.

Figure 3.11 shows the parameter region in which synchronization exists, as computed by Murakami & Ohtsubo (2002), in terms of the synchronization error ($\sigma = \frac{\langle |I_T - I_R| \rangle}{\langle I_R \rangle}$, where I_T and I_R are the normalized intensities of the transmitter and receiver lasers), as a function of the injection rate R_{inj} (representing the percentage of the transmitter's output intensity injected into the receiver laser cavity) and the

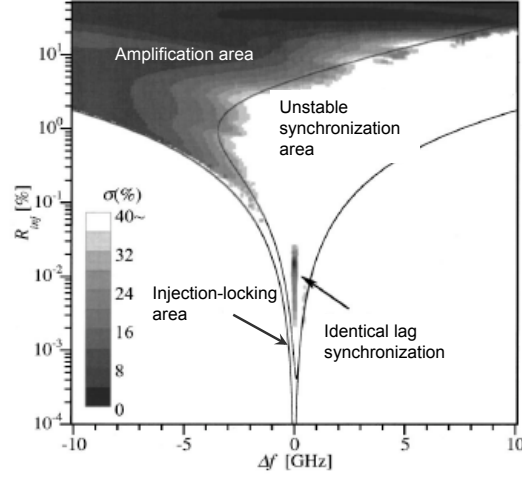


Figure 3.11: Phase diagram of a semiconductor laser receiving the injection from another, chaotic semiconductor laser subject to optical feedback, as a function of detuning and injection strength. The quality of the synchronization is represented by using gray scale with synchronization error, encoded in grey scale. From Murakami & Ohtsubo (2002)

detuning, $\Delta f = \frac{\omega}{2\pi}$. In this figure the boundaries, denoted by the outer solid lines, represent the injection-locking area (region where the lasers are locked in frequency when coupled) for two unidirectionally coupled lasers when the emitter laser operates at the continuous wave regime (i.e. in absence of optical feedback). In this case, the locking area, is composed by two main synchronization regions corresponding to stable and unstable synchronization. The lack of symmetry within the locking area is a consequence of the carrier changes induced by the α parameter (van Tartwijk & Agrawal, 1998). In the unstable region different dynamical regimes can be induced in the receiver laser depending on the injection current: periodicity, quasiperiodicity and chaos (Wieczorek et al., 2002). In the stable region different kinds of synchronization are observed. When optical feedback is present, identical lag synchronization is achieved for zero detuning and for small injection rates, when the coupling and feedback delay times are chosen to be equal. For large enough injection rate, ampli-

fication is observed even for detunings clearly different from zero (asymmetrically between negative and positive detunings). The amplification area is a region where the receiver output is non-linearly amplified. In this region the receiver output is larger than that of the emitter laser.

In the closed loop configuration (Fig. 3.9(b)), both lasers have their own optical feedback, with delays τ_1 and τ_2 respectively. This fact makes the system more symmetric, but on the other hand this configuration is more sensitive to parameter mismatch, and a careful tuning of the feedback parameter in the receiver (κ_2) is needed. In this configuration the relation between the delay times, on the one hand, and the coupling and feedback strengths, on the other, determine the time lag between the synchronized outputs, as in the open loop configuration. In the more symmetric configuration, i.e. when the injected light in the two lasers is the same, (which happens when the condition $\kappa_1 = \kappa_2 + \kappa_c$ is satisfied), zero-lag identical synchronization solution emerges. Note that this solution is equivalent to the open loop configuration for $\kappa_2 = 0$. Anticipated and retarded synchronization can also be observed for appropriate parameters.

3.2.1.2 Modeling chaotic synchronization between unidirectionally coupled lasers

In order to perform numerical simulations of the open and closed loop configurations, we use a generalized version of the Lang-Kobayashi that reads (Mirasso et al., 2002; Gonzalez et al., 2007):

$$\frac{dE_1}{dt} = \frac{1+i\alpha}{2}(G_1 - \gamma_1)E_1(t) + \kappa_1 e^{-i\omega_1\tau_1} E_1(t - \tau_1) + \sqrt{2\beta N_1} \xi_1(t), \quad (3.7)$$

$$\begin{aligned} \frac{dE_2}{dt} = & \frac{1+i\alpha}{2}(G_2 - \gamma_2)E_2(t) + \kappa_2 e^{-i\omega_2\tau_2} E_2(t - \tau_2) \\ & + \kappa_{12} e^{i(\Delta\omega t - \omega_2\tau_{12})} E_1(t - \tau_{12}) + \sqrt{2\beta N_2} \xi_2(t), \end{aligned} \quad (3.8)$$

$$\frac{dN_i}{dt} = C_b - \gamma_e N_{th} - G_i |E_i(t)|^2, \quad (3.9)$$

where subindex $i = 1, 2$ denotes lasers SL1 and SL2 respectively. $E_{1,2}(t)$ is the electric field and, $N_{1,2}$ is the carrier number, and $\omega_{1,2}$ are the free-running optical frequencies of the two lasers. $\Delta\omega = \omega_1 - \omega_2$ is the detuning between lasers. The first terms in the right-hand side of Eq. (3.7) and Eq. (3.8) are related with stimulated emission. The linewidth enhancement factor α is assumed to be the same for both lasers, $\gamma_{1,2}$ is the inverse photon lifetime, and $G_{1,2} = g_{1,2}(N_{1,2} - N_{1,2}^0)$ is the gain (assumed linear), where $N_{1,2}^0$ denotes the carrier number at transparency and $g_{1,2}$ is the differential gain (gain saturation is neglected because the lasers operate close to threshold).

The second term in the right hand side of Eq. (3.7) and Eq. (3.8) is the feedback term, described by $\tau_{1,2}$ (feedback delay time) and $\kappa_{1,2}$ (feedback coupling strength). The feedback term in Eq. (3.8) is zero for the open loop configuration. The last term in Eq. (3.7) corresponds to the spontaneous emission noise, represented by a Gaussian white noise of zero mean, with spontaneous emission rate β . The third term in the Eq. (3.8) is the coupling term described by τ_{12} (injection delay time) and κ_{12} (injection coupling strength). This coupling term only appears on the field equation for the second laser in order to assure a unidirectional coupling.

3.2.2 Bidirectional injection

When two lasers mutually interact, we say that they are bidirectionally coupled. Synchronization phenomena in mutually (or bidirectionally) coupled semiconductor lasers has also been widely studied. Due to the reciprocal interactions between lasers, it is possible to induce chaotic behavior also in absence of feedback (Heil et al., 2001). In this section we are going to discuss the synchronization phenomena exhibited by two bidirectionally coupled lasers.

3.2.2.1 Types of configurations

For two bidirectionally coupled lasers, two kind of configurations can be devised. The difference between them lies on the presence or absence of feedback on the lasers. In the case of absence of feedback, the chaotic dynamics of the lasers is only induced by the mutual interaction. From now we will refer to this coupling architecture as face-to-face configuration. In Fig. 3.12(a) schematic setup of a face-to-face coupling configuration is depicted. For this coupling architecture lag-synchronization can be observed with a time lag between both signals equal to τ_c .

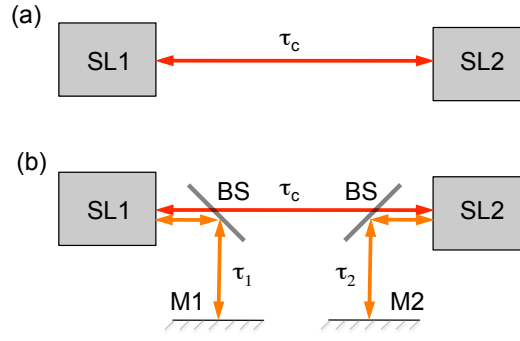


Figure 3.12: Bidirectionally coupled lasers face to face without (a) and with feedbacks (b). SL: semiconductor lasers, BS: beam splitters M: mirrors. τ_c is the coupling time between SL's and τ_i is the feedback time for each SL.

In Fig. 3.13(a) we show the cross-correlation function when the coupling strength between lasers is the same ($\kappa_{12} = \kappa_{21} = \kappa_c$) and also the optical frequencies are equal ($\omega_1 = \omega_2$). As Heil et al. (2001) showed, the optical frequencies plays an important role in order to establish which laser leads the dynamics. So, if the lasers have the same optical frequencies, a spontaneous symmetry-breaking leads into a switching of the role of leader between both lasers (Heil et al., 2001; Tiana-Alsina et al., 2009). On the other hand, when one of the lasers is detuned respect to the other one ($\Delta\omega = \omega_2 - \omega_1$), the laser with higher frequency takes the role of the leader.

Figures 3.13(c,d) show the cross-correlation function for a positive and negative detuning, respectively. It is worth to note that, in the face-to-face configuration, the zero-lag solution exists but it is unstable. In Ch. 8 we quantify the level of stochasticity in the dynamics of two mutually coupled semiconductor lasers. More specifically, we analyze the switching dynamics of the leader-laggard regime.

When the lasers have their own feedback (Fig. 3.12(b)), the zero-lag solution stabilizes, as depicted in Fig. 3.13(b), when the coupling and the feedback delay times are chosen to be the same. When the delay times are not equal, lag synchronization is observed at $\Delta\tau = \tau_c - \tau_{1,2}$. In Ch. 10 we analyze the stability of the zero-lag solution under different parameter variations, such as pump current and detuning, when the delay times are equal.

3.2.2.2 Modeling chaos synchronization between bidirectionally coupled lasers

As in Sec. 3.2.1.2, we use a generalized version of the Lang-Kobayashi equations, in order to simulate the behavior of two bidirectionally coupled semiconductor lasers with and without feedback. In this case the equations read:

$$\begin{aligned} \frac{dE_1}{dt} &= \frac{1+i\alpha}{2}(G_1 - \gamma_1)E_1(t) + \kappa_1 e^{-i\omega_1\tau_1} E_1(t - \tau_1) \\ &+ \kappa_{2,1} e^{i(\Delta\omega t - \omega_2\tau_c)} E_2(t - \tau_c) + \sqrt{2\beta N_1} \xi_1(t), \end{aligned} \quad (3.10)$$

$$\begin{aligned} \frac{dE_2}{dt} &= \frac{1+i\alpha}{2}(G_2 - \gamma_2)E_2(t) + \kappa_2 e^{-i\omega_2\tau_2} E_2(t - \tau_2) \\ &+ \kappa_{1,2} e^{i(\Delta\omega t - \omega_1\tau_c)} E_1(t - \tau_c) + \sqrt{2\beta N_2} \xi_2(t), \end{aligned} \quad (3.11)$$

$$\frac{dN_i}{dt} = C_b - \gamma_e N_{th} - G_i |E_i(t)|^2. \quad (3.12)$$

The model is the same as in the previous sections, but now the injection term appears in both field equations, in order to describe mutually coupling between lasers. Note that the feedback terms are set to zero on the face-to-face configuration (i.e. $\kappa_1 = \kappa_2 = 0$).

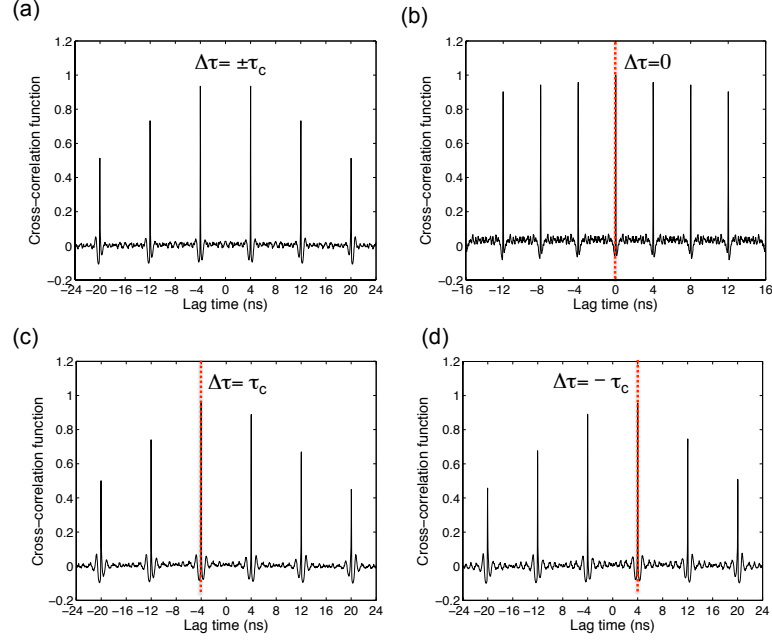


Figure 3.13: Cross-correlation function for two bidirectionally coupled lasers. (a) leader-laggard switching in the case of face to face configuration with $\Delta\omega = 0$. (b) the zero-lag solution is stabilized when the feedback terms are different from zero. Panels (c) and (d) show that one of lasers can be induced to lead the dynamics by introducing a detuning different from zero. The red dashed line indicates the maximum of the cross correlation.

In this section we have discussed about synchronization and their consequences. We have also studied the possibility to synchronize chaotic oscillators under different coupling architectures. In the next Chapter we are going to present different statistical techniques that will allow us to characterize the degree of complexity of a chaotic system.

Chapter 4

Stochasticity and complexity in dynamical systems

As discussed in previous Chapters, nonlinear systems can show chaotic motion, and so a very irregular and complex behavior lying between complete order (i.e. periodic behavior) and complete disorder (i.e. stochastic behavior). Due to the fact that chaotic motion is characterized by complex non-periodic time traces with a broadband Fourier spectrum, it is not trivial to distinguish a chaotic signal from a stochastic signal. Therefore a natural question that arises is: is an irregularly-behaving system chaotic or stochastic? In principle, if we are able to determine the maximum Lyapunov exponent (λ) or the Kolmogorov-Sinai entropy per unit time (h_{KS}) of a data sequence, we would know, with certainty, whether the sequence is generated by a deterministic law (in which case $\lambda, h_{KS} < \infty$) or by a stochastic law (in which case $\lambda, h_{KS} \rightarrow \infty$). Due to the finite resolution and noise contamination of the experimental data, this methodology usually is not able to give conclusive results. Depending on the degrees of freedom of the system, different quantifiers have been used in order to distinguish chaos from noise. For detecting low-dimensional chaos, metric entropy and Lyapunov exponents can be used. Grassberger & Procac-

cia (1983) proposed a method for the evaluation of the correlation dimension based on the assumption that any chaotic system displays a finite fractal dimension, in opposition with a stochastic system that should display an infinite fractal dimension. A generalization of this method was proposed by Kantz & Olbrich (2000) and Cencini et al. (2000), who presented a way to classify the behavior of the time series as stochastic or deterministic for a given scale ϵ in the phase space, and time resolution τ according to the dependence of the entropy, $h(\epsilon, \tau)$ on ϵ and τ , and the redundancy $r(\epsilon)$ on ϵ . The redundancy measures the amount of uncertainty on future observations which can be removed by the knowledge of the past (Cencini et al., 2000). For long enough time series and for a given time scale τ , if the entropy, $h(\epsilon)$ saturates we can consider the system to be deterministic. On the other hand, if the redundancy of the system is constant, for a given length scale ϵ , the system behaves stochastically.

Another way to quantify the degree of stochasticity of a given time trace is based on the concept of information theory. For stochastic processes, Shannon's entropy is a very useful technique to measure the degree of unpredictability. An information measure can be viewed as a quantity that depends on the probability that a certain event occurs (the more improbable the event is, the more information we gain from its occurrence). Therefore, firstly we need a probability distribution associated with the time series. The determination of the most adequate probability distribution is crucial to reveal all the relevant physical details. In what follows we give a brief description of the information theory quantifiers used in this Thesis.

4.1 Entropy and statistical complexity

As mentioned above, completely ordered or disordered systems display opposite behaviors in terms of the Shannon entropy (i.e. $S = 0$ and $S = \log(n)$ respectively, where n is the number of possible outcomes). Nevertheless, at a given level of ran-

domness, away from these extremes, systems with different probability distributions can have the same entropy, thus the entropy measures do not quantify how the patterns are structured in a given process (Feldman & Crutchfield, 1998). This fact leads to the need of using other methods in order to quantify the degree of structure present in a process. The methods that have been proposed as general structural measures are often referred as statistical complexity measures. Measures of complexity can be useful tools for understanding neural computation (Young & Schuff, 2008), analyzing patterns in medical signals (Rosso et al., 2003), etc...

In Fig. 4.1 we show satellite images of three different cities, which exemplify the different degrees of order that a system can show. In Fig. 4.1(a) we depict l'Eixample of Barcelona, which is a very good example of ordered urban development. On the opposite limit, in Fig. 4.1(c) we show the case of Mexico DF, which exemplifies a pure random structure. In between there are several cities with an intermediate degree of order (complex): Figure 4.1(b) shows Terrassa as an example of a complex city.

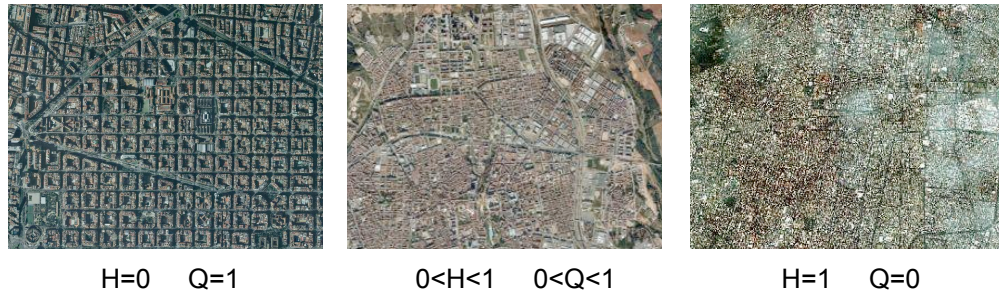


Figure 4.1: Three different examples of cities that have different disorder degree. (a) High order (Barcelona), (b) intermediate mix between order and disorder (Terrassa), and (c) high randomness (Mexico DF).

With the tools presented in the paragraph above we can qualitatively measure the degree of disorder, but if we want to quantitatively measure the complexity

of a system we have to use a suitable quantifier. We now present the complexity measure used during this Thesis, which we call MPR complexity, after the authors who originally introduced it (Martin et al., 2006). This measure is defined as:

$$C[P] = H[P] \cdot Q[P], \quad (4.1)$$

where $H[P]$ is the normalized Shannon's entropy and $Q[P]$ quantifies the disequilibrium at a given probability distribution P .

We can define a complex system as a system consisting of many different and connected parts. The complexity of a system must reach a maximum between the limits of perfect order and perfect disorder. The evaluation of the complexity provides additional insight into the details of the system, such as the correlational structure between the components of the physical process under study. Contrary to the entropy, the complexity is zero for both random and periodic processes and takes positive values in between of these extreme cases. In Fig. 4.2 we show the evolution of three statistical quantifiers frequently used to calculate the statistical complexity as a function of the amount of order of the system. The red line is the normalized Shannon's entropy, which increases monotonically with the disorder of the system. On the other hand, the green line depicts the Jensen-Kullback divergence, which measures the degree of disequilibrium of the system, decreasing monotonically when the disorder increases. Finally, the blue line is the statistical complexity defined as the product of the two previous quantities, which shows a maximum for intermediate values of the system disorder.

In our case we define the entropy as follows:

$$H[P] = S[P]/S_{\max}, \quad (4.2)$$

where $S[P] = -\sum_{i=1}^N p_i \log p_i$ and $S_{\max} = \log N$ (corresponding to the case in which all the patterns have the same probability), with $N = D!$ being the total number of vectors over which P is computed and p_i the probability of appearance of a certain

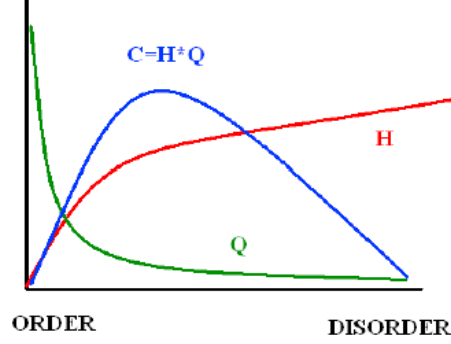


Figure 4.2: Schematic representation of the behavior of the Entropy (H), the Jensen-Kullback divergence (Q) and the statistical complexity (C) as a function of the order of the system.

pattern π in the order sequence of a set of time-consecutive values of the system's state variables.

In our case, the patterns have been determined by dividing the signal $\{s(t_i) = \{s_i\}, i = 1 \dots M\}$ into $M - D$ overlapping vectors of dimension D . Then, the value of s_i in a given vector is replaced by a number from 0 to $D - 1$, in accordance with the relative length of s_i in the ordered sequence (0 corresponding to the smaller s_i and $D - 1$ to the bigger s_i in each vector, as it is shown in Fig. 4.3 for the particular value of $D = 3$). This is the so-called Bandt and Pompe approach (BP) (Bandt & Pompe, 2002), which can be applied to any type of time series (periodic, chaotic and stochastic) with a weak assumption of stationarity (the probability of a certain pattern should not depend on time). The probability distribution $P = p(\pi)$ is defined as follows:

$$p(\pi) = \frac{\#(i | i \leq M - D; (s_{i+1}, \dots, s_{i+D}) \text{ has type } \pi)}{M - D + 1} \quad (4.3)$$

Since the number of different vectors of dimension D is equal to $D!$, to have a good

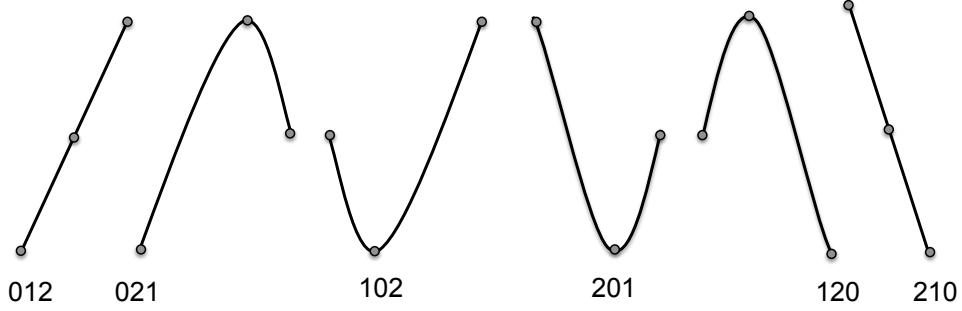


Figure 4.3: Possible ordinal patterns π for $D = 3$. The number of ordinal patterns is $N = D!$.

statistics one must have a large enough number of measures, such that $M - D \gg D!$.

The other term in Eq. (4.1) is $Q[P] = Q_0 J_S[P, P_e]$, which quantifies the disequilibrium and is calculated from the symmetric form $J_S[P, P_e]$ of the Kullback-Leiber relative entropy $K[P|P_e]$ (Kullback & Leibler, 1951).

$$\begin{aligned} J_S[P, P_e] &= (K[P|P_e] + K[P_e|P])/2 \\ &= S[(P + P_e)/2] - S[P]/2 - S[P_e]/2, \end{aligned} \quad (4.4)$$

P_e is the equilibrium distribution ($p_{i,e} = 1/N \forall i$) and Q_0 is a normalization constant,

$$Q_0 = -2 \left\{ \left(\frac{N+1}{N} \right) \ln(N+1) - 2 \ln(2N) + \ln N \right\}^{-1}, \quad (4.5)$$

The statistical complexity defined above is nothing more than the product between the Shannon entropy and the Jensen-Shannon divergence, but it is worth to note that the complexity is a nontrivial function of the entropy, because it depends on two different probabilities distributions.

To understand how the complexity behaves under different time traces, we calculate the MPR statistical complexity for three different probability distributions: uniform, normal and Dirac distribution. In Fig. 4.4 we show the case of a process

with uniform distribution on the unit interval $[0, 1]$. By calculating the patterns using the BP method, one finds that the probability density function (PDF) for the possible patterns is also an uniform distribution, where all the D -dimensional patterns have the same probability ($p_i \sim 1/D!$ as can be seen in Fig. 4.4(b)). Note that as mentioned above, when all the patterns have the same probability, the entropy $S = S_{\max}$, and thus $H[P] \sim 1$ and $Q[P] \sim 0$. Therefore the complexity associated with a uniformly distributed process is $C[P] \sim 0$.

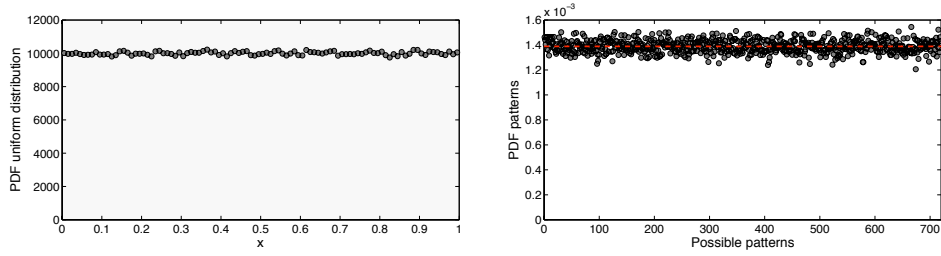


Figure 4.4: (a) PDF for a uniformly distributed process between 0 and 1. (b) PDF for the possible ordinal patterns with an embedding dimension $D = 6$. The dashed red line indicates the equilibrium probability.

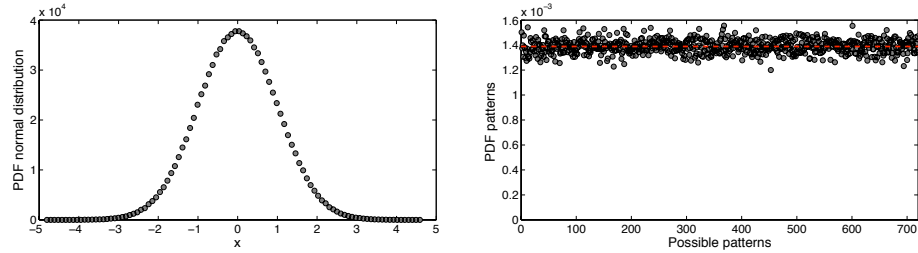


Figure 4.5: (a) PDF for a normal distribution with mean, $\mu = 0$, and variance $\sigma^2 = 1$. (b) PDF for the possible ordinal patterns with an embedding dimension $D = 6$. The dashed red line indicates the equilibrium probability.

In Fig. 4.5 we show a process that follows a normal distribution with mean $\mu = 0$ and variance $\sigma^2 = 1$. As in the previous example, the PDF for the possible patterns

follows a uniform distribution and so, the complexity is $C[P] \sim 0$. At this point it is worth to note that the value of the entropy depends on how we calculate the probabilities. For the Gaussian process one can use directly the probability of the distribution, $P(x) = \frac{1}{\sqrt{2\pi}\sigma} e^{-\frac{(x-\mu)^2}{2\sigma^2}}$, instead of the pattern probability, and then the Shannon's entropy is $H[P] = \frac{1}{2} \ln(2\pi\sigma) + \frac{1}{2}$, instead of $H[P] = 1$ (obtained with the BP method). This, however, does not modify the qualitative conclusion that can be extracted from the statistical complexity measure.

Finally, we analyze a Dirac distribution, $\delta(x - \mu)$, with $\mu = 0.5$. In this case only one pattern is possible, and thus $H[P] \sim 0$ and $Q[P] \sim 1$. Therefore the complexity associated with a Dirac distributed process is $C[P] \sim 0$, as in the previous cases.

On the other hand, the complexity is non-zero, when the probability distribution is neither uniform nor unimodal, as we will seen in Ch. 7 for the case of a laser with feedback. In this Chapter we have analyzed the behavior of the complexity for the time between dropouts at different pump currents.

4.2 Forbidden ordinal patterns

Another strategy that can be used to distinguish between chaotic and noisy time series is the method of the forbidden sequences. As shown by Amigó et al. (2006, 2007, 2008) for an one-dimensional map, not all possible ordinal patterns can be observed in the time series, i.e. there are forbidden patterns. For instance, for a deterministic logistic map $x_{k+1} = 4x_k(1 - x_k)$, the pattern of embedding dimension $D = 3$, $x_{k+s} < x_{k+1} < x_k$, never appears (Amigó et al., 2007) and so, this pattern is forbidden.

On the other hand, in time series generated by uncorrelated stochastic processes, for instance every ordinal patterns has the same probability of appearance. Therefore, if the time series is long enough, all the patterns will exist. Consequently, the existence of forbidden patterns in a long enough time series is an indication of its

deterministic character. If the probability distribution of the stochastic process is not uniform (i.e. correlated stochastic process), it is possible to observe forbidden patterns if the time series is not long enough. If the time series is sufficiently long, the patterns with low probability of appearance will eventually appear. In this case we should call these non-observed patterns as missing patterns instead of forbidden patterns.

For a real time series, we have always an stochastic component that can contaminate the data, so real data may exhibit false forbidden patterns due to their finite and noisy character. Amigó et al. (2007) proposed a test that uses these missing ordinal patterns to distinguish chaos from noise on finite time series contaminated with white noise. The technique consists in three steps: a) Compute the number of forbidden patterns in a series of adequate length (the length of the time series, M , has to fulfill that $M \gg D! + D - 1$). b) Generate a surrogate of the sequence, i.e., change the order of its elements in a random way. c) Proceed as in step a) with the randomized sequence. If the obtained forbidden patterns are the same, then the sequence is not deterministic at all (or the noise is high enough to mask the deterministic behavior), but if the distributions of forbidden patterns are different, one can conclude that the raw data is deterministic. In Fig. 4.6 we show an experimental example corresponding to the leader-laggard dynamics of two bidirectionally coupled semiconductor lasers (see Ch. 8 for more details), where it is possible to observe the evolution of the number of forbidden patterns as a function of the length of the time series. In this figure, we are comparing the evolution of an experimental time series with the surrogated time series. Due to the stochastic component of the experimental data, the number of forbidden patterns tends to zero but with much slower velocity than the surrogated data.

Figure 4.7(a), shows the evolution of the forbidden patterns for the logistic map, as a function of the uniform noise amplitude, η_{max} , for a fixed series length, $N = 6000$ and embedding dimension $D = 6$. In this figure one can see how the number of forbidden patterns decreases when the noise amplitude is increased. This figure

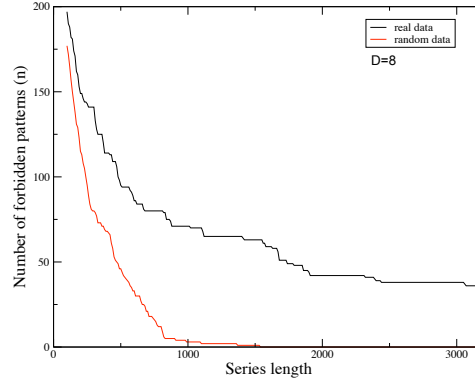


Figure 4.6: Evolution of the number of forbidden patterns with embedding dimension $D = 8$. The experimental time series is depicted in black and the surrogated in red.

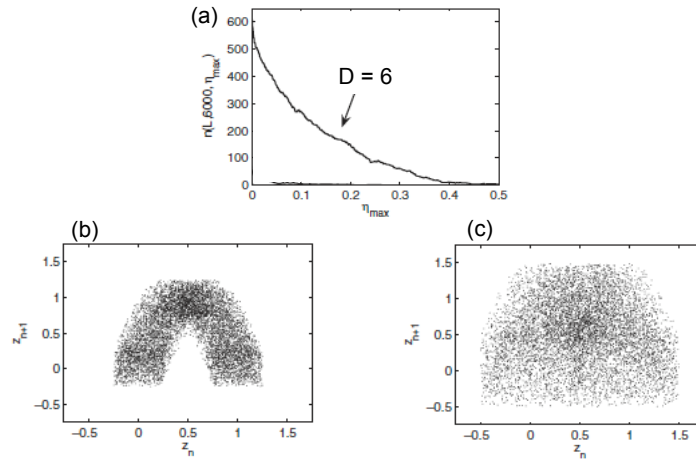


Figure 4.7: (a) Number of forbidden patterns as a function of the noise amplitude. Return map for noisy time series from logistic map with $\eta_{max} = 0.25$ (b) and $\eta_{max} = 0.5$ (c). From Amigó et al. (2007)

also gives information on how far we are from a chaotic deterministic process. In Fig. 4.7(b,c) we show the return map for two noise levels of the logistic map. For

an intermediate amount of noise (Fig. 4.7(b)) it is still possible to observe the deterministic dynamics but for a high enough noise level (Fig. 4.7(c)) does not allow to observe the underlying deterministic dynamics. However, even in this case one can realize that the number of forbidden patterns is slightly higher than zero (corresponding to the purely random case) as it is shown in Fig. 4.7(a).

In Ch. 8 we have applied the ideas presented above in order to quantify the level of stochasticity in the ladder-laggard dynamics of two mutually coupled semiconductor lasers.

Chapter 5

Temporal correlations induced by intrinsic rate switching in a semiconductor laser with feedback

The behavior of certain natural and technological systems often takes the form of sequences of discrete events (point processes), whose statistical properties can be controlled both by the internal dynamics of the system and by the environmental conditions to which the system is subjected. Correlations in the time intervals between subsequent events (named inter-spike intervals, ISIs, in what follows) arise in certain circumstances and can be functionally relevant. This is the case, for instance, of sensory neurons, in which ISI correlations are known to increase information transfer (Chacron et al., 2001) by reducing low-frequency noise (Chacron et al., 2004). A natural question is then, what is the simplest mechanism leading to ISI correlations?

In this Chapter we show experimentally that a semiconductor laser with feedback operating in the low-frequency fluctuation regime (which as discussed in Ch. 2 can be interpreted as an excitable dynamics, similar in some ways to that of a neuron)

exhibits in a natural manner ISI correlations. This behavior is attributed to the intrinsically complex firing behavior displayed by the laser for certain pump currents. In order to verify this conclusion we introduce an external modulation of the dropout rate (mimicking the intrinsic complex dynamics) by means of a dichotomous modulation of pump current. Our results show experimentally that dichotomous modulation of the laser's pumping leads to controlled correlations in the sequence of inter-spike intervals.

5.1 Experimental setup

Our experimental system consists in a diode laser subject to optical feedback through an external mirror presented in Sec. 2.1. As shown in that section, due to the action of the delayed feedback, the laser exhibits (provided the feedback strength is moderate and the pumping is close to threshold) an irregular series of power dropouts that can be interpreted as excitable pulses (Giudici et al., 1997; Mulet & Mirasso, 1999). In order to modulate the pumping we use a 100 kHz Bias T. The schematic experimental setup is depicted in Fig. 5.1.

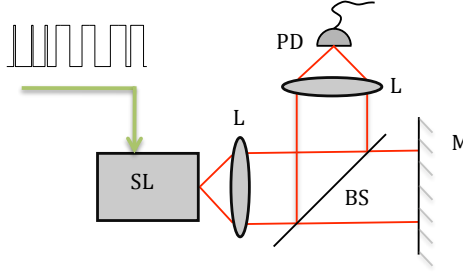


Figure 5.1: Scheme of the experimental setup of a semiconductor laser subject to an optical feedback and driven by a dichotomous noise. SL semiconductor laser; M mirror; PD photodetector; BS beam splitter; L lenses.

The laser used in our experiment is an AlGaInP Fabry-Perot semiconductor laser,

operating at a nominal wavelength around 650 nm. The laser intensity is captured by a high-speed fiber photodetector with 2 GHz bandwidth. The signal is then amplified, using a 2-GHz high-speed electronic amplifier, and sent to an oscilloscope with 1 GHz bandwidth.

Due to the finite bandwidth of our detection system we are only able to show the slow dynamics of the system, which is nevertheless enough for our study. Fig. 5.2(a) shows the dynamics of the laser in response to a constant DC input in its pumping. The feedback strength and the pump current level are chosen such that the laser operates in the above-mentioned LFF regime.

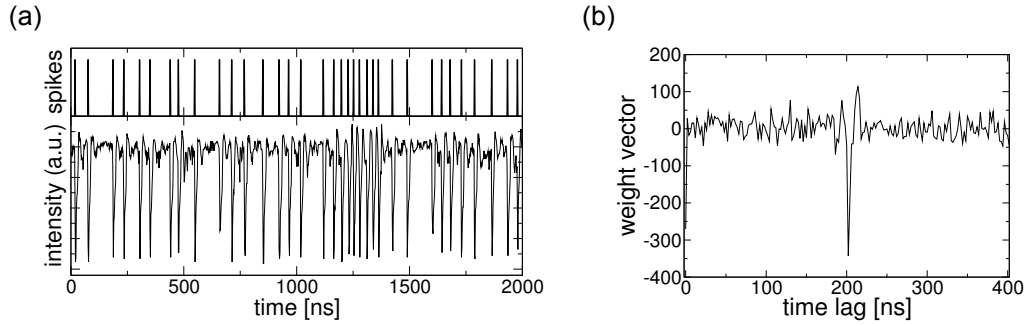


Figure 5.2: (a) Laser output for a constant pump current (lower panel, $V = 110$ mV) and detected spikes (upper panel). (b) Weight vector \vec{w} used for spike/no spike classification.

Spike detection

For the general purpose of this study it turns out that spike detection by simple threshold crossing is insufficient; here we use a pattern classification algorithm to detect power dropouts. To this end, we have gone through the time series with a sliding window of 400 ns, yielding a $n = 201$ -dimensional vector \vec{x} with a time discretization interval $\Delta t = 2$ ns. The vector \vec{x} has been rescaled and shifted such that the minimum and the maximum of the elements with 0 and 1, respectively. We

used a perceptron to decide whether \vec{x} has a spike around its center. Specifically, if $\vec{w} \cdot \vec{x} > \theta$, where \vec{w} is a real-valued weight vector and θ is a threshold, a spike at the center element was considered to occur, and the sliding window was shifted forward by a refractory time $\tau_{ref} = 14$ ns. If on the other hand $\vec{w} \cdot \vec{x} < \theta$, the pattern was classified as “no spike” and the time window was shifted by Δt . The weight vector \vec{w} and the threshold θ have been determined using the perceptron learning rule on a training set $(\vec{x}^\mu, \sigma^\mu)$ of 169 “spike” ($\sigma^\mu = 1$) and 127 “no spike” ($\sigma^\mu = 0$) examples. The resulting weight vector is shown Fig. 5.2(b). In order to prevent false positives in the noise floor, additional criteria have been adopted by the perceptron to accept a spike: we required that (i) $(1/n) \sum_i x_i > 0.6$, (ii) the skewness of x_i be smaller than -0.8 and (iii) the local standard deviation (averaged over 10 points surrounding the suspected spike) must be larger than 0.2 .

5.2 Serial correlation (SCC) at constant pumping

Once the spikes are detected, one could ask for how the power dropouts are organized in time. To that end, we define the k -th time interval between consecutive dropouts as I_k , and calculate the correlation between intervals separated by n dropouts as

$$\rho_n \equiv \frac{\langle I_{k+n} I_k \rangle - \langle I_{k+n} \rangle \langle I_k \rangle}{\langle I_k^2 \rangle - \langle I_k \rangle^2}. \quad (5.1)$$

By definition $\rho_0 = 1$, while ρ_1 measures the level of correlation between neighboring intervals. For a Poisson process, for instance, intervals are independent of each other and $\rho_n = 0$ for $n > 0$.

As depicted in Fig. 5.3(a), the sequence of power dropouts (our “spikes” in what follows) are uncorrelated up to the critical pumping $V_p = 50$ mV, beyond which the intervals between spikes appear to be significantly correlated. Serial correlation at constant pumping becomes maximum at $V_p = 100$ mV, and for sufficiently high DC signals (i.e. near CC but still in LFF’s regime) the correlations start to decrease until reaching zero again for a value of the DC signal equal to ~ 200 mV.

In order to investigate the origin of these correlations, we compared the joint ISI density $P(T_i, T_{i+1})$ of the return map, i.e. of adjacent ISIs, with the joint density $P_r(T_i, T_{i+1}) \equiv P(T_i)P(T_{i+1})$ associated to a renewal process (i.e. each interval is independent from the other) with ISI density $P(T_i)$ (Engel et al., 2008). Fig. 5.3(b) shows the difference $\delta P(T_i, T_{i+1}) = P(T_i, T_{i+1}) - P_r(T_i, T_{i+1})$ between both joint densities. The positive correlations seen at DC signals about 110 mV (Fig. 5.3(b)) are clearly due to an excess of short-short interval pairs (T_i, T_{i+1}) compared to the renewal assumption, which is apparent from the significantly positive spot in the lower left corner. The short-short events are mainly related with the appearance of fast firing activity in the temporal series of the laser. The combination of fast and slow firing states suggests the presence of slowly changing processes for certain constant DC signal.

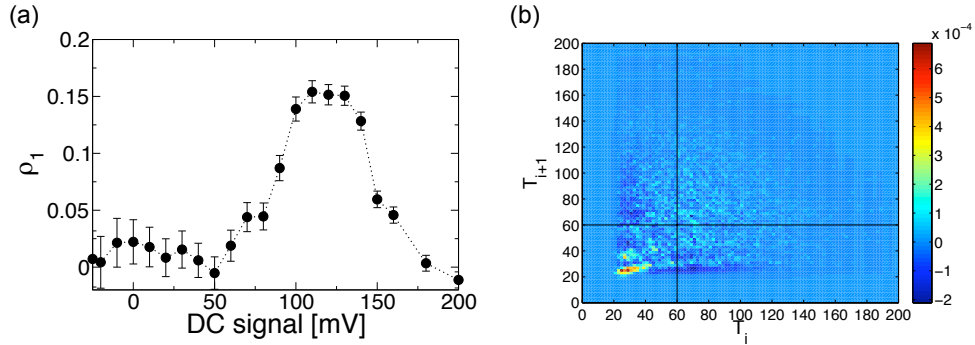


Figure 5.3: (a) Correlation coefficient of adjacent intervals ρ_1 for different levels of the pump current. (b) Correlation map $\delta P(T_i, T_{i+1})$ of the DC data for $V = 110$ mV; solid lines indicate the mean interval.

5.3 Two-state theory of laser dropouts

In the previous sections we have seen that the time intervals between consecutive dropouts exhibited by semiconductor lasers with optical feedback can display, for

large enough values of the pump current, statistical correlations. We have also pointed out that data suggests an intrinsic slow modulation of the rate at which the power dropouts occur. We now describe briefly a theoretical analysis of a general two-state model that links these two observations, showing that spontaneous switchings between two firing-rate regimes in a generic excitable medium gives rise to correlations in the corresponding inter-spike interval series.

We consider a discrete kinetic model in which the system switches randomly between two different states with distinct firing statistics (Fig. 5.4(a)). Mathematically, the model takes the form of a telegraph noise $S(t)$ that switches stochastically between two renewal processes: an active state $S = 1$ with high firing rate k_1 and coefficient of variation C_{V1} , and a quasi-quiescent state $S = 2$ with low firing rate k_2 and coefficient of variation C_{V2} . The waiting times in each state are taken to be exponentially distributed with switching rate λ (Fig. 5.4(b)). We ignore here the transition region between $S = 1$ and $S = 2$ in which an interval can belong to both states.

Since firing within each of the two states is a renewal process, the only source of correlation between inter-event intervals is the dichotomous switching between the two states $S = 1$ and $S = 2$. The expression for the correlation coefficient involves two averages: one with respect to the renewal process for a fixed realization of the dichotomous process, and another one with respect to the state of the dichotomous process itself. The resulting correlation coefficient for $n \geq 1$ is (Schwalger & Lindner, 2011)

$$\rho_n = \frac{\exp \left[- \left(\hat{\lambda}_1 + \frac{\hat{\lambda}_2}{\gamma} \right) n \right]}{1 + \frac{\gamma \hat{\lambda}_1 + \hat{\lambda}_2}{(1-\gamma)^2 \hat{\lambda}_1 \hat{\lambda}_2} \left(\gamma \hat{\lambda}_2 C_{V1}^2 + \hat{\lambda}_1 C_{V2}^2 \right)}, \quad (5.2)$$

with $\gamma = k_2/k_1$, $\hat{\lambda}_1 = \lambda_1/k_1$, $\hat{\lambda}_2 = \lambda_2/k_1$.

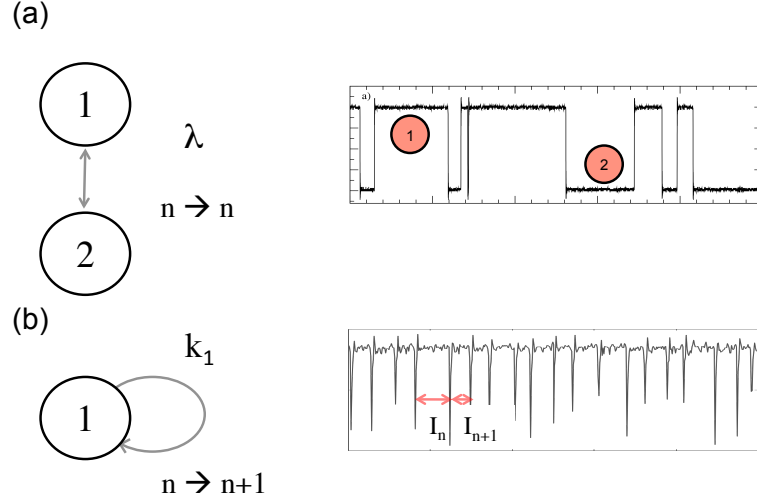


Figure 5.4: (a) Schematic representation of a system with two states being subject to firing with rate k_j . (b) The two states (1 and 2) switch dichotomically from one to the other at a rate λ . The symbol n denotes the event number, and I_n the n -th ISI. The panels on the right represent the real situations that the schemes represent in the case of a laser with feedback, with the upper plot showing the pump current of the laser for the case of external dichotomous driving, and the lower plot representing a time series of dropouts (events).

5.4 Comparison between experiments and theory

To test whether the serial correlations of the laser dropouts can be indeed associated to two alternating renewal processes, we estimated the parameters of the two-state model from the experimental sequence of ISIs. To this end, we labeled each interval in the experimental time series as “fast” or “slow” firing state. This was decided based on whether the ISI was smaller or larger than a certain threshold. The threshold was chosen as the largest interval T_i in the correlation map, Fig. 5.3(a), that significantly contributes to the prominent positive spot that gives rise to positive serial correlations. For the analysis of the DC data, an interval was considered as

belonging to the fast state if it was smaller than $T = 35$ ns. From the labeled ISI sequence one can determine the mean number, mean length and variance of intervals within a fast firing (slow firing) epoch [i.e. a subsequence of ISIs that are all smaller (larger) than θ] yielding values for $k_{1/2}$, $\lambda_{1/2}$ and $C_{V,1/2}$. The distribution of the number of ISIs in the slow firing state was approximately exponential. Further inspection of the correlations with fast/slow firing states reveals that the renewal assumption is approximately obeyed in the slow firing state state ($\rho_{1,slow} \approx 0.03$) but violated for the fast firing state ($\rho_{1,fast} \approx 0.1$).

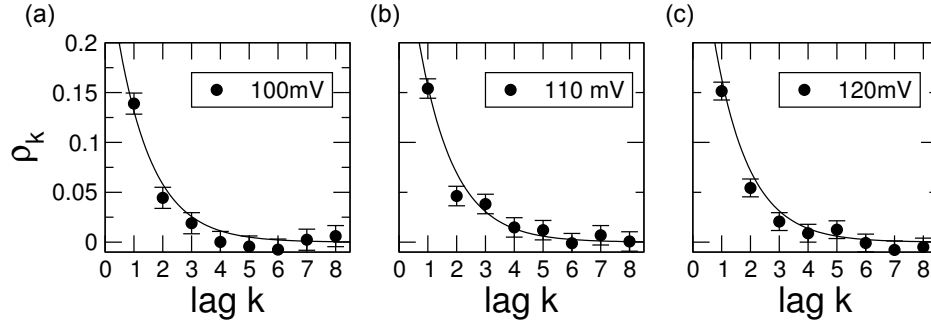


Figure 5.5: SCC as a function of the lag k for the DC data with $V = 100$ mV (a), $V = 110$ mV (b), and $V = 120$ mV (c). Symbols represent the experimental data, and the solid line the theoretical fit (Eq. (5.2)). The vertical error-bars are calculated as in Cox & Lewis (1966).

In Fig. 5.5 we show ρ_n for three different DC pumping inputs. We observe that the system shows small but non-negligible first-order (and second-order) serial correlations. The solid lines represent the theoretical results given in Eq. (5.2), using the values determined from the analysis of the dropout series described above. Although the assumptions of our two-level theory are probably not completely obeyed, we observe a reasonable agreement, indicating that the main source for the correlations of the total sequence is an intrinsic switching between two states with different firing statistics.

5.5 Externally controlled state switching

In order to test our interim conclusions that it is the switching between two states with different excitation rate what generates ISI correlations in a semiconductor laser with feedback, we now apply an external dichotomous modulation to the system, which we can control experimentally at will. Dichotomous noise has previously been found to lead to non-trivial correlations of residence times in bistable systems (Lindner & Schwalger, 2007; Schwalger & Lindner, 2008). Here we consider that the input signal of our excitable laser switches between two values (V_1 and V_2) with (symmetric) rate λ (Fig. 5.6(a)), and has an exponential correlation function $\langle \eta(t)\eta(t') \rangle = \sigma^2 \exp[-2\lambda|t - t'|]$, corresponding to a correlation time $\frac{1}{2\lambda}$ as depicted in Fig. 5.6(b). As shown in the inset of that plot, the exponential decay of the modulation is consistent with the analytical correlation of the dichotomous noise. The length of the time series used to calculate the autocorrelation was 1 ms. It is

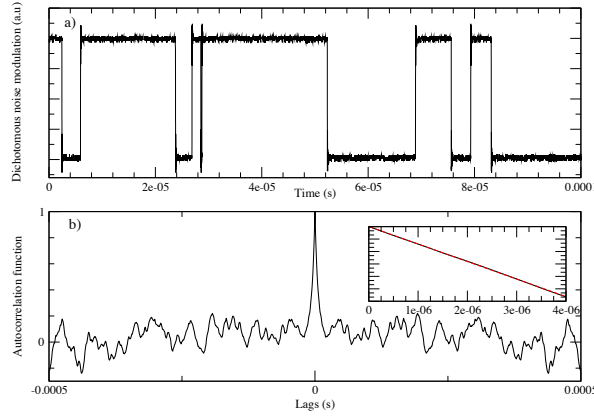


Figure 5.6: (a) Time trace for a dichotomous noise modulation with $\lambda = 100$ kHz. (b) Autocorrelation function of the noise. The inset shows a zoom of the autocorrelation with the time axis in logarithmic scale.

well known that the pumping of a semiconductor laser with feedback decreases the mean time between consecutive power dropouts, i.e. it increases the mean firing rate of the excitable system. Due to the dependence of the firing rate with respect to DC input, the dichotomous driving leads to switching between two firing rates, as shown in Fig. 5.7(a). The bottom trace in the figure depicts the response of the laser to the dichotomous signal represented in the top trace, for a particular switching rate λ and specific pumping levels. Figure 5.7(b) compares the serial correlation coefficient at $V_p = 100$ mV for different lags with the theory described above. The correlation exhibits an exponential decay with a good agreement with the theoretical predictions given by Eq. (5.2). Note that, as in experiments, we have taken $\lambda = 100$ kHz.

Figure 5.8 plots the first-order correlation coefficient ρ_1 versus the ratio of the firing rates, k_2/k_1 , corresponding to the two pumping levels of the dichotomous modulation. The firing rates are estimated as the average of the inverse time intervals between consecutive dropouts, from time traces of the laser's output intensity when subject to constant DC that correspond to each of the two levels of the dichotomous modulation. In this experiment, we have kept one of the pumping levels of the dichotomous modulation constant, and vary continuously the other one. The correlation shows a minimum (different from zero) when the firing rates are equal (i.e. in the DC case), and increases when k_2 becomes smaller and larger than k_1 . Interestingly, for $k_2 < k_1$ the first-order correlation exhibits a non-monotonic behavior with respect to the firing-rate ratio, first growing as k_2 departs (towards smaller values) from k_1 , reaching a maximum and decaying again for very small k_2 (for which most ISI's belong to a single firing state, which is renewal). This behavior is qualitatively reproduced by the theoretical expression given in Eq. 5.2, shown by the solid line in Fig. 5.8, which we remark has no free parameter and in this case has been applied to the external switching, instead of the internal one considered at the beginning of the Chapter.

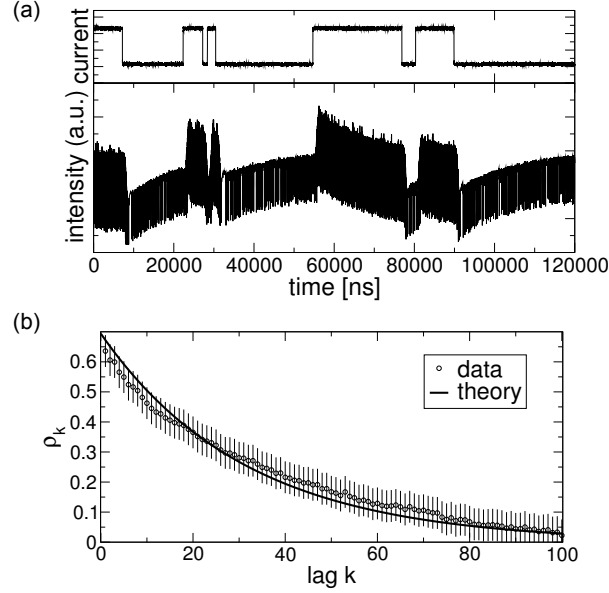


Figure 5.7: (a) Dichotomous noise modulation of the pumping (top, $\lambda = 100$ kHz) leads to a modulation of the dropout rates (bottom, $V_1 = 100$ mV, $V_2 = 0$ mV). (b) Correlation coefficient ρ_k measured from the extracted interval sequence (symbols, same parameter as in (a)) and two-state theory (solid line), where the parameters were determined from the unperturbed system. The vertical error-bars are calculated as in Cox & Lewis (1966).

5.6 Conclusions

In summary, we have shown experimentally that the power dropouts exhibited by a semiconductor laser with optical feedback display in certain conditions, correlations between inter-event intervals, and have proposed a discrete kinetic model that explains the mechanism of appearance of those correlations as resulting from the intrinsic switching of the system between two states with different firing rates. In order to test this conclusion we have applied an external random dichotomous modulation to the pumping of the excitable laser, and have observed that this external modulation also generates correlations in the time intervals between successive dropouts. The correlations under the dichotomous modulation exhibit a characteristic pattern

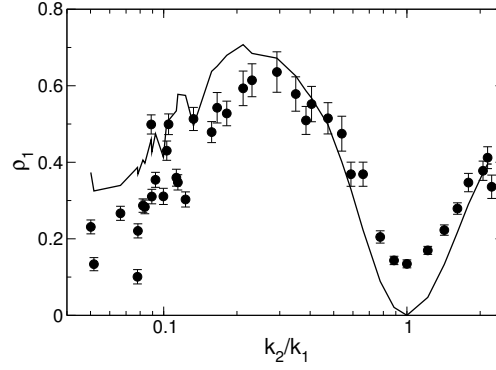


Figure 5.8: SCC at lag one as a function of the ratio of the rates $\gamma = k_2/k_1$ (dots). k_1 was held constant corresponding to $V_1 = 100$ mV, whereas k_2 was varied by varying the level V_2 . The two-state theory (based on the measured rates and C_v 's of the respective unperturbed processes) is depicted by the solid line. The vertical error-bars are calculated as in Cox & Lewis (1966).

as a function of the ratio between firing rates of the two levels of the modulation, which agrees with analytical results obtained in the discrete kinetic model. These results shed light on the minimal requirements to generate correlations in spike time series, showing in particular that no specific mechanisms intrinsic to the spiking system are necessary. This conclusion should be relevant to all spiking systems where ISI correlations are important, such as neuronal systems.

Once we have understood the intrinsic mechanism responsible to induce correlations in a ISI sequence one could ask how the dropouts are ordered within the temporal series. In the following two Chapters we calculate the probability of appearance of patterns (a sequence of ISI) as well as the probabilities of transitions between consecutive ordinal patterns and also the complexity of the ISI time series by using tools from information theory.

Chapter 6

Language structure of a semiconductor laser with feedback

In the previous Chapter we studied the first-order correlations that arise from the inter-dropout time series. We saw that correlations arise due to variations in the dropout rate across time, and were able to reproduce these correlations in a controlled way by applying an external current modulation. Our goal in this chapter is to shed light into the higher-order structural characteristics of the distribution of time between dropouts.

As shown in the previous Chapter, the specific subthreshold dynamics of an excitable system (such as a semiconductor laser with feedback) determines the correlation statistics of the pulse trains that it generates (Chacron et al., 2004). In turn, these correlations affect the functionality of the system, by regulating for instance its information encoding capabilities (Chacron et al., 2001; Avila-Akerberg & Chacron, 2011). It is thus important to establish the temporal organization of the spiking activity displayed by excitable systems. In this chapter we present a method to characterize this temporal organization based on symbolic analysis of the series of inter-dropout time intervals.

Much effort has been devoted to understand and characterize the excitable nature of the intensity power dropouts exhibited by semiconductor laser with optical feedback. In particular, an issue that has attracted much attention is the relative influence of the stochastic and deterministic nonlinear processes that are responsible for the dropouts. Several authors have investigated the characteristics of the LFFs in terms of the statistics of both the intensity fluctuations (Sukow et al., 1999; Hales et al., 2000; Torcini et al., 2006) and the time intervals between consecutive dropouts (in particular their probability distribution function) (Hohl et al., 1995; Mulet & Mirasso, 1999; Yacomotti et al., 1999; Martinez Avila et al., 2004; Hong & Shore, 2005b,a).

In this Chapter, we calculate the probabilities of transitions between consecutive ordinal patterns (Jalan et al., 2006). As discussed in Ch. 4, the ordinal pattern methodology is based on defining patterns (or “words”) in a time-series that result from ordering relations in sets of consecutive values of the series. In other words, we analyze the “language” of the LFFs by detecting consecutive words that appear with high relative frequency, similar to the sequences of words “it is” and “they are”, which are quite common in the English language. This analysis, in turn, provides us with the opportunity of performing a detailed comparison between experiments and theory.

Our results show that close to coherence collapse (but still in the LFF regime) not all the transition probabilities are equally probable; there are a few of them significantly more probable than the rest, which we consider to be a signature of deterministic triggering mechanisms. On the contrary, closer to threshold all the transition probabilities are similar, which suggests that in this region the LFFs are mainly triggered by noise. This result is coherent with previous reports in the literature, both for single lasers with optical feedback (Hales et al., 2000; Lam et al., 2003) and for coupled lasers, as we will show in Ch. 8.

We compare the experimental results with model predictions. Several models have

been proposed in the literature to explain the LFF dynamics (Eguia et al., 1998; Viktorov & Mandel, 2000; Huyet et al., 2000; Prasad et al., 2001). A well known model is the Lang-Kobayashi (LK) model, introduced in Sec. 2.1. As discussed in that Section, the LK model has been shown to successfully describe many features of the LFFs (Mork et al., 1992; Heil et al., 1999b; Sukow et al., 1999; Buldú et al., 2006; Torcini et al., 2006). A phenomenological model, proposed by Eguia, Mindlin and Giudici (Eguia et al., 1998) (in the following referred to as EMG model), consisting of a set of *ordinary* differential equations, has also been shown to explain many features of the LFFs (Yacomotti et al., 1999; Mendez et al., 2001, 2002).

In this Chapter we compare the predictions of these two models and find that the experimental observations are in good agreement with simulations of the LK model; in particular the word that is significantly more probable in the LK simulations is the same as in the experiments. On the other hand, the agreement with simulations of the EMG model is only qualitative, as in simulations of this model the most significant word is not the same as in the experiments. Thus, we show that the ordinal pattern method can also be used to distinguish among theoretical models.

6.1 Symbolic analysis of low-frequency fluctuations

The experimental system used in this chapter consists in a laser diode subject to optical feedback from an external cavity. The laser used in the experiment is an AlGaInP Fabry-Perot semiconductor laser (Sharp GHO6510B2A) operating at a nominal wavelength $\lambda_n = 650$ nm. The temperature and pump current of the laser are controlled with an accuracy of ± 0.01 °C and ± 0.01 mA. For a temperature $T = 18.30$ °C, the threshold current of the solitary laser is $I_{th} = 29.39$ mA. The round-trip time in the external cavity is 2.5 ns. The laser intensity is detected by a high-speed fiber photodetector with a bandwidth of 2 GHz (DET01CFC), whose

signal is amplified using a 2-GHz high-speed amplifier (Femto) and sent to a 1-GHz oscilloscope (Agilent DS06104A). Due to the relatively low bandwidth of the detection system, we are only able to measure the slow feedback-induced dynamics (i.e., the LFF power dropouts) and not the fast picosecond pulses.

The laser output was measured for increasing bias current, which leads to an increase in the frequency of the power dropouts. The dropouts start to merge for large enough pump current, thus leading to the qualitatively different dynamical behavior of coherence collapse (see Sec.2.1.2). In Ch. 7 we characterize this transition in terms of complexity measures applied to the time-series of inter-dropout intervals (IDIs). The results showed that the normalized Shannon entropy was close to 1 all the way up to a critical pump current, which we will refer to as I_c , $I_c \simeq 33$ mA, after which it leveled off rapidly at a value smaller than 1.

In order to further characterize these variations in the dynamical behavior of the LFFs, we transform the time series of IDIs, $\{\Delta T_0, \Delta T_1, \Delta T_2, \dots\}$ into a series of words or “ordinal patterns” (OPs), $\{s_1, s_2, \dots\}$. As discussed in Ch. 4 a first step is to divide a time series $\{x(t), t = 1 \dots M\}$, into $M - D$ overlapping vectors of dimension D . Then, each element of a vector is replaced by a number from 0 to $D - 1$, in accordance with the relative strength of the element in the ordered sequence (0 corresponding to the shortest and $D - 1$ to the longest value in each vector). Each vector has then associated an “ordinal pattern” composed by D symbols. For example, with $D = 3$, the IDI sequence $\{\Delta T_0, \Delta T_1, \Delta T_2\} = \{5, 1, 10\}$ gives the ordinal pattern (1 0 2), as $\Delta T_1 < \Delta T_0 < \Delta T_2$.

The number of different ordinal patterns of dimension D is $D!$. By counting the number of times a pattern s_i appears in the sequence $\{s_1, s_2, \dots\}$ one can compute the probability distribution function (PDF) of the ordinal patterns. Since the number of possible ordinal patterns is $D!$, to have a good statistics one must have a long enough time series, such that $(M - D) \gg D!$.

In the following we consider various pattern lengths, specifically $D = 2, 3$, and

4 and compute the PDFs of the $D!$ possible patterns, and the $D! \times D!$ transition probabilities (TPs) between these patterns (Jalan et al., 2006). The TPs quantify the frequency in which a certain pattern in the time series transforms into another one, and constitute a novel way to yield insight into time-correlations present in the laser dynamics.

The ordinal patterns can be labeled, without loss of generality, by means of a scalar, $\alpha = 1, \dots, D!$, with increasing values according to their degree of increase between consecutive IDIs. For instance:

- In the case $D = 2$, the order relation $\Delta T_m \geq \Delta T_{m+1}$ for the m -th and $(m+1)$ -th IDIs of the series ('10' in the notation of BP) corresponds to $\alpha = 1$, while $\alpha = 2$ denotes the pattern $\Delta T_m < \Delta T_{m+1}$ ('01' in the BP notation), see Fig. 6.1;
- In the case $D = 3$, $\alpha = 1$ represents the '210' pattern ($\Delta T_m \geq \Delta T_{m+1} \geq \Delta T_{m+2}$), $\alpha = 2$ stands for the '201' pattern ($\Delta T_m \geq \Delta T_{m+2} > \Delta T_{m+1}$), and so on.

Using this notation, the TPs can be expressed as $P(\alpha \rightarrow \beta)$, where α and β can take any value of the set $\{1, \dots, D!\}$, and

$$P(\alpha \rightarrow \beta) = \frac{\sum_{t=1}^L n(s_t = \alpha, s_{t+1} = \beta)}{\sum_{t=1}^L n(s_t = \alpha)}, \quad (6.1)$$

where n is a count of the number of times of occurrence in the series of OPs, $\{s_1, s_2, \dots, s_L\}$, of length L .

Only non-overlapping words are considered in what follows. Hence for M IDIs, the number of patterns generated is $L = \lfloor (M - D)/D \rfloor + 1$, where $\lfloor x \rfloor$ denotes the largest integer less than or equal to x . Under these conditions, for surrogated data all TPs are expected to be equal to $1/D!$, corresponding to a Markov process between word pairs. In order to have good statistics the number of OPs must be

much larger than the number of possible transitions, i.e. $(M - D)/D \gg D! \times D!$. In the following section the analysis is done with time-series of $M \simeq 10^4$ IDIs, which results in sequences of about 3300 (5000) words of $D = 3$ ($D = 2$).

6.2 Experimental results

A typical example of the word transitions discussed above is displayed in Fig. 6.1, where two instances of the transition from the word $\alpha = 2$ ('01') to the word $\beta = 1$ ('10') can be seen. In the experimental time series, Fig. 6.1, this is a typical situation: when the pump current is greater than the critical pump current, $I_c \simeq 33$ mA, the transition from word $\alpha = 2$ to word $\beta = 1$ is over-represented in the laser language (for comparison, Fig. 6.7 displays numerical results that will be discussed in Sec. 6.3). This can be clearly seen in Fig. 6.2, which plots the PDFs of the two words (top panels) and the probabilities of the four transitions between them (bottom panels). The figure compares the results obtained from analyzing both the experimental time series (left panels) and the surrogated time series (right panels).

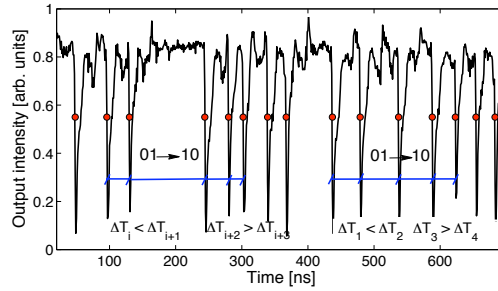


Figure 6.1: Experimental time series of the laser intensity for an injection current $I = 34$ mA. The circles indicate the times used to calculate the inter-dropout intervals, and a few words and transitions are indicated as examples.

Figure 6.2(a) reveals that, for $D = 2$ the two words ('01' and '10') are equally

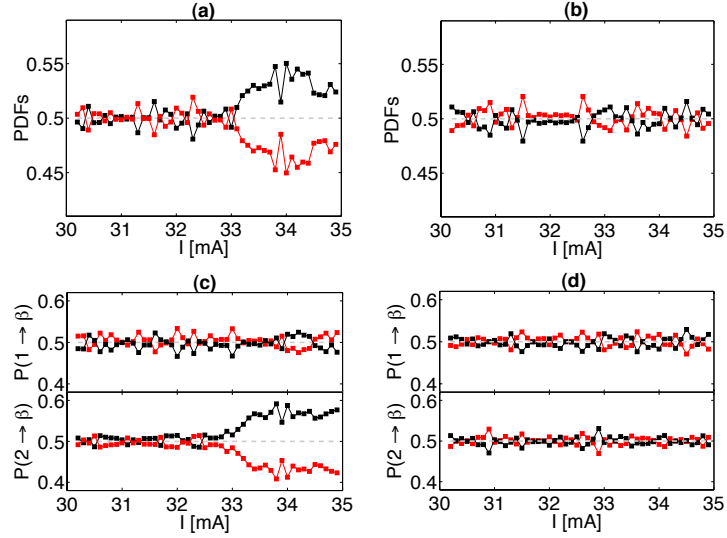


Figure 6.2: Probability distributions (a,b) of the two possible words for $D = 2$ ($\alpha = 1$ in black and $\alpha = 2$ in red), and the four possible transition probabilities (c,d) between consecutive words (colors corresponds to the transitioned word) vs the laser injection current. Captions (a, c) display results for the experimental time series and (b, d) for the surrogated data. The dashed horizontal gray lines indicate the equally distributed probabilities that are expected for random series.

represented in the experimental time series up to the critical current value $I_c \simeq 33$ mA, beyond which one of the words ('10', $\alpha = 1$) becomes over-represented at the expense of the other ('01', $\alpha = 2$). This behavior is related to the changes in the statistical complexity that will be discussed in Ch. 7 below, at the same pump current.

We note that this behavior is robust and does not depend on where on the IDI series the word encoding begins. This contrasts with the case of a regular periodic series: for a repetitive set of words $\alpha = 2$ ('01'), for instance, a shift of one position in the IDI series would transform all the words into $\alpha = 1$ ('10'). The fact that this does not happen in our case highlights the irregular character of our series, in spite of

which a clear over-representation of a word emerges for large enough pump current. Note that in Fig. 6.2(a) the two PDFs level off shortly after I_c . This phenomenology is conspicuously absent for the surrogated series (Fig. 6.2(b)).

Concurrently with the changes exhibited by the word PDFs as the pump current increases, a similar behavior occurs for the transition probabilities. In particular, starting again at $I_c = 33$ mA the transition from $\alpha = 2$ to $\beta = 1$ becomes clearly over-represented, in this case at the expense of the $2 \rightarrow 2$ transition, as shown in Fig. 6.2(c). Transitions departing from $\alpha = 1$ are left unchanged throughout all pump levels. Once again, the phenomenon is, as expected, absent in the surrogated series (Fig. 6.2(d)).

The results presented above for $D = 2$ (two-letter words) are also seen for three-letter words, $D = 3$. For instance, regarding the relative frequencies of the 6 words that exist for $D = 3$, once more all words are equally probable for low enough pump currents (Fig. 6.3(a)). However, for currents above the critical, value one of the words ($\alpha = 1$, namely ‘210’) becomes over-represented, at the expense mainly of $\alpha = 2$ (‘201’), which becomes less frequent than the average, also in comparison with the surrogate (Fig. 6.3(b)). In general, the results reveal a large heterogeneity in the relative frequencies of the different words for $I > I_c$, with several words departing from the equi-distribution value, either above or below it, and in different amounts.

The most frequent word, $\alpha = 1$, appears to be also the most transitioned to, as shown in Fig. 6.4. Correspondingly, the least frequent word, $\alpha = 2$, is also the one less transitioned to. Therefore, decreasing patterns seem to be the predominant ones when the pump current is above the critical value. These conclusions also hold for words of four letters, where ‘3210’ appears to be the most recurrent pattern beyond I_c (however, the differences among the probabilities of the different words are less pronounced, results not shown).

In order to make more evident the heterogeneity of the word PDFs and TPs reported above, in Fig. 6.5 we compare, for $D = 3$ the PDFs of the 6 possible

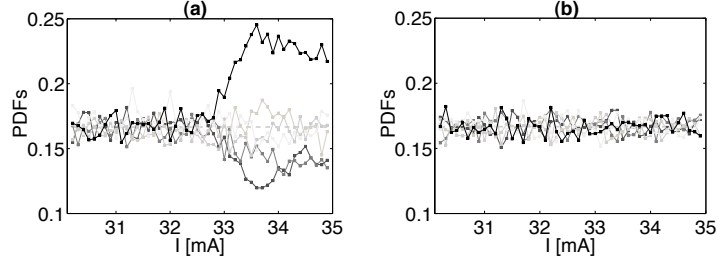


Figure 6.3: Probability distributions of the 6 words with $D = 3$ vs. the pump current, for both the experimental (a) and the surrogated (b) time series. The different words are represented in grayscale, with black corresponding to $\alpha = 1$, and lighter grays to increasing α up to 6.

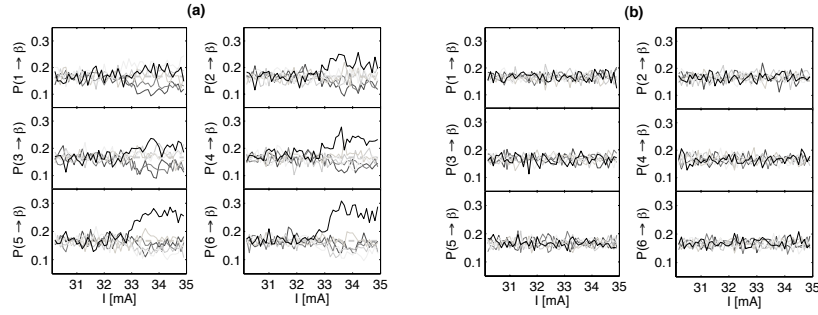


Figure 6.4: Transition probabilities vs. pump current for the 36 possible transitions between consecutive words with $D = 3$. The plots are organized according to the starting word, with the final word represented in grayscale, following the criterion of Fig. 6.3. Results for the experimental series are shown in (a), and for the surrogate series are shown in (b).

words (left panels) and the 36 TPs (right panels) for two different injection currents: below the critical current value I_c (top panels) and above the critical current value I_c (bottom panels). In all the panels, the black bars correspond to the experimental series, and the red ones, to the surrogated series.

One can notice that in the panel corresponding to $I > I_c$ the word distribution shows a behavior clearly different from that of the surrogate data (panel c), while these differences disappear when the pump current is smaller than I_c (panel a). The TPs are more heterogeneous above the critical current, in comparison with surrogate data (panel d), than below the critical current (panel b).

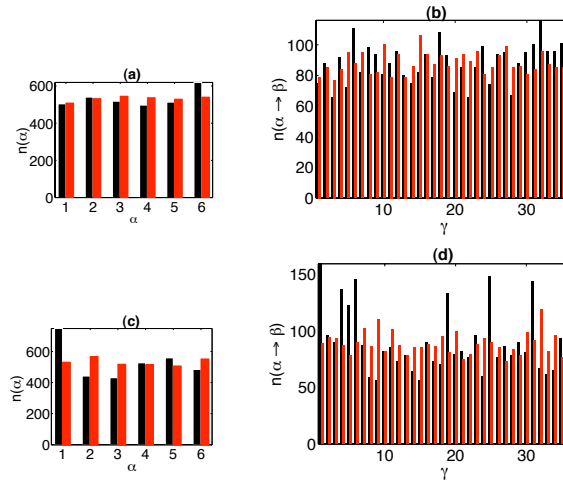


Figure 6.5: Histograms of the occurrences of words of $D = 3$ (a, c) and consecutive transitions (b, d) at a pump current below the critical value, $I = 32$ mA (a, b) and above the critical value, $I = 34$ mA (c, d). The number of transition are labeled from $\alpha = 1 \rightarrow \beta = 1$ ($\gamma = 1$) to $\alpha = 6 \rightarrow \beta = 6$ ($\gamma = 36$). Black bars correspond to the experimental series, and the red ones to the surrogated series.

So far we have analyzed transitions probabilities between *consecutive* words, but there could be higher-order correlations in the word transitions. An inspection of panels (a) and (c) of Fig. 6.2 reveals that, for $I > I_c$, differences for the TPs are higher than for the PDFs. For instance, for $I = 34$ mA, the under- and over-represented TPs are close to 0.4 and 0.6, respectively, whereas the PDFs are close to 0.45 and 0.55. In other words, the TPs exhibit asymmetries larger than the words PDFs.

In order to see how long-lasting these high-order correlations are, we performed a statistical analysis of the transitions between *non-consecutive* words. Figure 6.6 shows, for a fixed laser current, the probabilities of transitions between increasingly distant patterns,

$$P_{\tau_{lag}}(\alpha \rightarrow \beta) = \frac{\sum_{t=1}^L n(s_t = \alpha, s_{t+\tau_{lag}} = \beta)}{\sum_{t=1}^L n(s_t = \alpha)}, \quad (6.2)$$

where n is a count of the number of times of occurrence in a series.

Figure 6.6 shows that as transitions between more “distant” words are considered, i.e., as τ_{lag} increases, word correlations are lost and the TPs end up exhibiting the statistical nature of the word appearances in the IDI series, as revealed by the PDFs. In other words, the deterministic signature arising for injection currents larger than I_c is lost when transitions between non-consecutive patterns distant more than 2 IDIs are considered.

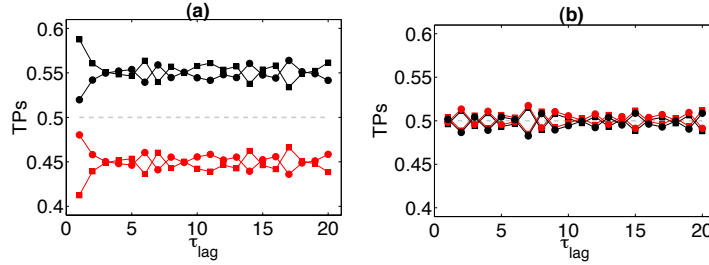


Figure 6.6: Transition probabilities between words of $D = 2$ separated by τ_{lag} (see Eq. 6.2), for an injection current above the critical value, $I = 34$ mA. Right column: experimental data; left column: surrogate data. Circles correspond to $\alpha = 1$ and squares to $\alpha = 2$. Colors stand for the transitioned pattern: black is $\beta = 1$ and red is $\beta = 2$.

We conclude this section by remarking that these observations are robust against experimental parameter variations such as time delay and feedback strength. We performed experiments with different semiconductor lasers and setup arrangements, and observed the same results. Specifically, the words ‘10’ for $D = 2$ and ‘210’

for $D = 3$ are over-represented in the LFF dynamics for current values close to coherence collapse.

We interpret these observations as due to the topology of the phase-space of the laser dynamics, that is such that, when the dropouts are very frequent, if a dropout occurs before the laser is fully recovered from the previous one, it performs an excursion in phase space that is shorter than the previous one, so that the following inter-dropout interval will be shorter than the previous one.

6.3 Comparison with theoretical models

In order to test whether the above reported observations are particular to the specific experimental conditions used for the generation of the time series, we now turn to numerical modeling. We compare the observations with the predictions of two models: the Lang-Kobayashi model (Sec. 2.1.1) and EMG model (Eguia et al., 1998).

6.3.1 The LK model

First we compare the experimental results with the Lang-Kobayashi model presented in Sec. 2.1.1. Figure 6.7 shows the simulated time series obtained with the LK model. This figure already suggests that $\alpha = 1$ is a frequent word, and that the inter-word transition going from $\alpha = 2$ to $\beta = 1$ is also frequent, in good agreement with the experimental results. In order to verify this observation, we now perform systematic numerical simulations to quantify the corresponding PDFs and TPs with good statistics.

Table 6.1 lists the parameter values used in the numerical simulations described below. For these parameters we have (except when the injection current is close to the threshold) a large number of power-dropouts before the LFFs die away (Zamora-Munt et al., 2010a; Torcini et al., 2006). This allows to compute the word PDFs

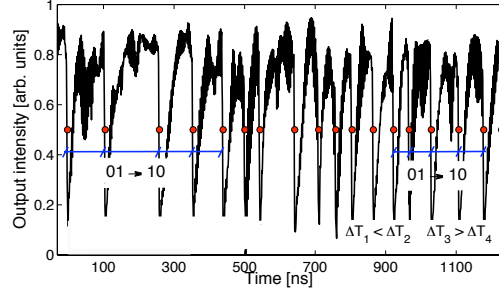


Figure 6.7: Simulated intensity from the LK model with a pump current parameter $\mu = 1.08$. The circles indicate the times used to calculate the inter-dropout intervals, and a few words and transitions are indicated as examples. The parameters used in the numerical simulations are given in Table 6.1.

with good statistics. When the pump current parameter is close to threshold, the transient LFF dynamics is short and there are not enough dropouts to compute the word statistics reliably. To overcome this problem we simulated several stochastic trajectories, with both different noise realizations in the rate equations and different stochastic initial conditions, which were chosen with the optical field at the noise level, $E(t) = \xi(t)$, $0 \leq t \leq \tau$, and $N(0) = 0$.

The PDFs of the words resulting from these IDI series, and the corresponding TPs, are shown for increasing pump currents in Fig. 6.8. The results show a qualitative agreement with Fig. 6.2: as the pump current increases, the frequency of the word $\alpha = 1$ ('10') grows, and the transition from $\alpha = 2$ to $\beta = 1$ (i.e. from '01' to '10') becomes more probable.

The results for $D = 3$ (Fig. 6.9) show the same qualitative agreement with the experiments as for $D = 2$. In particular, for $D = 3$ the word $\alpha = 1$ ('210') is the most probable to occur and to be transitioned to. The agreement also holds for the least likely word ($\alpha = 2$, i.e. '201'), as can be seen in Fig. 6.9(a). We note that for both $D = 2$ and $D = 3$, the agreement between theory and experiments is remarkable,

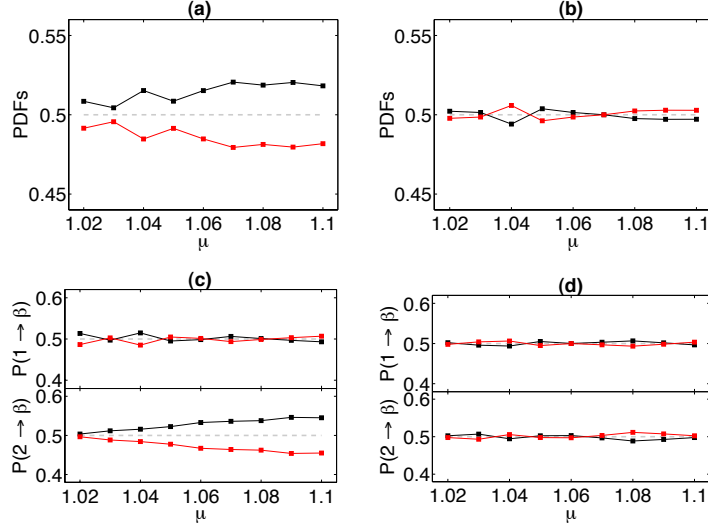


Figure 6.8: Results of simulations of the LK model. Words with $D = 2$ are considered. (a,b) PDFs of the two possible words vs. the pump current parameter, computed from the numerical time series (a) and their surrogates (b). Panels (c,d) depict the corresponding TPs between consecutive words, again for the numerical series (c) and the surrogated (d). The color coding is as in Fig. 6.2.

as the preferred word and transition are the same here as in the experimental time series. This result is relevant because it demonstrates that the behavior is a general feature of semiconductor lasers with optical feedback, and not of the specific device and/or conditions of this experiment.

Table 6.1: Laser parameters of the numerical model in the LFF regime

Symbol	Parameter	Value
μ	pump current of LD1	$1.02 \cdots 1.1 \cdot \mu_{th}$
τ	feedback time delay	3 ns
κ_f	feedback strength	60 ns^{-1}
γ_e	inverse carrier lifetime	1 ns^{-1}
γ	inverse photon lifetime	0.3 ps^{-1}
α	linewidth enhancement factor	4
ϵ	saturation coefficient	0.01
β	noise intensity	$1 \cdot 10^{-4} \text{ ns}^{-1}$

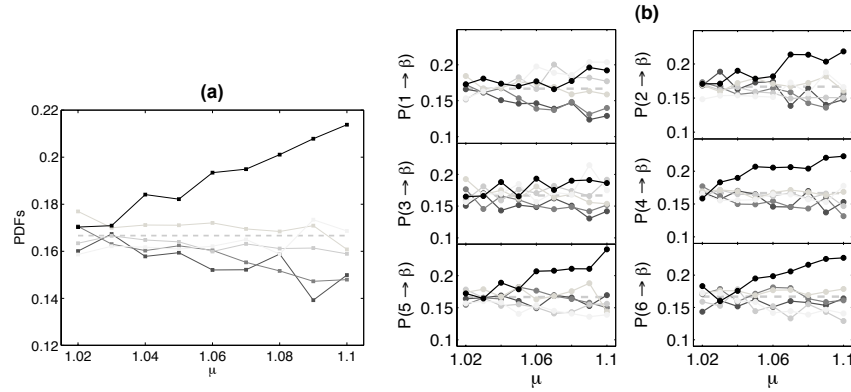


Figure 6.9: Results of simulations of the LK model, considering words with $D = 3$. PDFs of the six possible words vs. the pump current, computed from the numerically generated time series (a) and the corresponding TPs between consecutive words (b). The color coding is as in Fig. 6.3.

6.3.2 The EMG model

The rate equations of the phenomenological, low-dimensional model proposed by Eguia *et al.* are (Eguia *et al.*, 1998):

$$\frac{dx}{dt} = y + \sqrt{2\beta}\xi(t) \quad (6.3)$$

$$\frac{dy}{dt} = x - y - x^3 + xy + \epsilon_1 + \epsilon_2 x^2 \quad (6.4)$$

where ϵ_1 and ϵ_2 are control parameters, β is the noise strength and $\xi(t)$ is a Gaussian white noise.

The model exhibits excitability for appropriate parameters (Méndez *et al.*, 2005). In the excitable regime the model has three fixed points: a stable focus (node), a saddle point and an unstable focus (repeller). An initial condition close to the node, in the presence of noise, may result in a trajectory that crosses the stable manifold of the saddle and relaxes back after a long excursion in phase space. These pulses can be associated to the dropouts of the laser intensity in the LFF dynamics. The noise term makes the LFF's sustained in time. A typical time-series displaying such noise-induced pulses was presented in Fig.6.10.

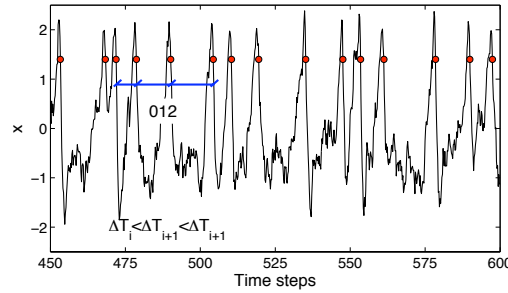


Figure 6.10: Simulated time trace from the EMG model with $\beta = 0.1$, $\epsilon_1 = 0.26$, and $\epsilon_2 = 0.44$. The circles indicate the times used to calculate the inter-dropout intervals. Few words are indicated as examples.

We computed the PDFs of the ordinal patterns and the corresponding TPs, for

parameters within the excitable region, when the amount of noise is varied. The results are presented in Figs. 6.11 (PDFs) and 6.12 (TPs) for the original and for the surrogated data. First, one can observe that for low noise strength all words are equally probable (as in the experiments and LK simulations) while for an intermediate amount of noise the word ‘012’ ($\alpha = 6$) shows a higher probability of appearance, which does not occur neither in the experiments nor in the LK simulations. For even higher noise strength not only the word ‘012’ is over-represented, but also the word ‘210’ is over-represented, which also does not fully agree with the experiments and the LK simulations, where only the word ‘210’ is over-represented.

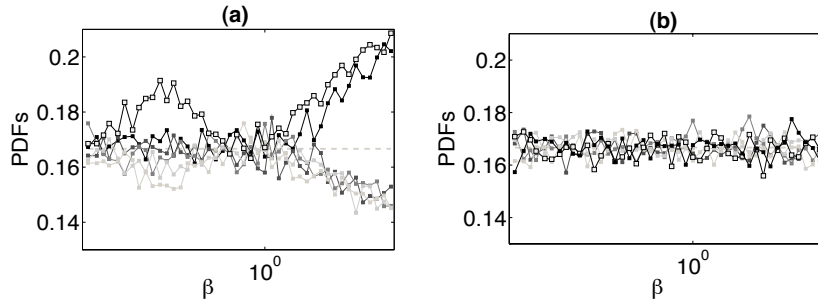


Figure 6.11: Results of simulations of the EMG model, considering words with $D = 3$. The PDFs of the six possible words are plotted vs. the noise strength (in arbitrary units): (a) original data, (b) surrogated data. The color coding is as in Fig. 6.3 except the word ‘012’ ($\alpha = 6$), which now is represented, for clarity, with a black line and unfilled squares. Parameters are those of the bottom plot of Fig. 6.1.

Therefore, we can conclude that, while the EMG model captures many features of the LFFs, the subtle time-correlations among a few consecutive dropouts is not fully represented. This can be due to the low-dimensionality of the EMG model. The laser with optical feedback is a time-delayed system and in that sense the LK model, which has a delayed term, is more likely to represent the high-dimensional phase space of the experimental system.

Since in the EMG model the parameter ϵ_1 has been associated with the laser bias current (Yacomotti et al., 1999), we also studied the effect of varying this parameter and did not find an improvement in the agreement with the experimental observations (results not shown). Perhaps in this model, to effectively simulate the variation of the laser current, one needs to simultaneously vary both ϵ_1 and β ; however, this is an interesting study that is beyond of the scope of the present work and that is left for future work.

Our results also point at the fact that the ordinal pattern methodology can be a powerful tool for determining subtle differences among various numerical models, that cannot be uncovered by other methods that do not take into account the time-ordering of the sequence of dropout events, such as the study of the inter-spike time distributions.

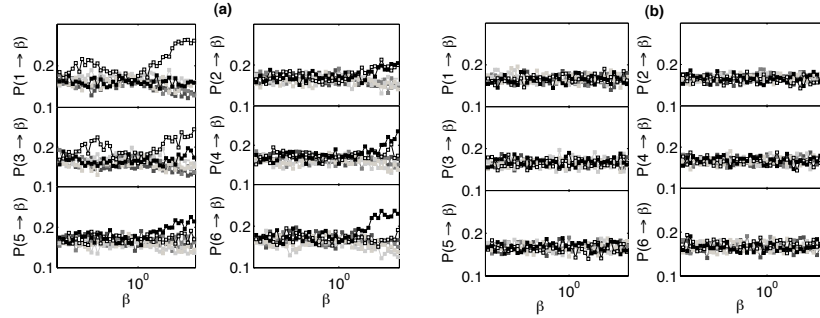


Figure 6.12: Transition probabilities vs. the noise strength (in arbitrary units) for simulations of the EMG model. The 36 possible transitions between consecutive non-overlapping words with $D = 3$ are shown. The plots are organized and colored according to the same criteria used in Fig. 6.4. Results of the original time series are shown in (a), and of the surrogate series, in (b). Parameters are those of the bottom plot of Fig. 6.1.

6.4 Conclusions

We have characterized experimentally and numerically the language organization of a semiconductor laser with optical feedback, operating in an excitable regime. This regime allows us to represent the laser dynamics in terms of a “language” of words, which represent the ordinal relations within sets of consecutive inter-event intervals.

Our results show that at low pump currents all words occur with the same frequency and the same probability to be transitioned to, thus we can interpret that the dropouts are uncorrelated and memory effects play no role, and consequently that the dropouts are mainly driven by noise. As the injection current increases the dropouts become more frequent and time correlations between them appear. These correlations imply that there is some memory in the system, so that certain words and transitions become more frequent than others. We conjecture that this behavior is a signature of determinism in the system for sufficiently large pump currents. This result agrees with previous investigations of the same experimental situation via complexity measures (Tiana-Alsina et al., 2010), but goes beyond that analysis, since the distribution of transition probabilities between words quantifies a higher-order organization of the language.

We have also shown that the words lose their correlations when we increase the distance between transitioning words, at which point the TPs match the probability of the word appearance.

We also performed a critical comparison of the observations with the predictions of two models: the Lang-Kobayashi (Ch. 2) model and EMG model (Eguia et al., 1998). The LK model is time-delayed model (and thus, its phase space is infinite dimensional) while the EMG model is a low-dimensional one. We found that, in spite of the fact that both models successfully predict the probability distribution of the inter-dropout intervals, their predictions differ regarding the probability distribution of the ordinal patterns and the transition probabilities.

In the LK model the preferred word and transition coincide with the experimental time series, which confirms the generic nature of the experimental observations, independent of the semiconductor laser device and/or the parameters. In the EMG model the agreement is not as good, as not only the word ‘210’ is over-represented (in good agreement with observations), but also the word ‘012’ is over-represented, which is not observed experimentally. Therefore, our results also show that the ordinal pattern methodology can be a powerful tool for determining subtle differences among excitable models, that can not be uncovered by methods that do not take into account the time-ordering of the sequence of excitable pulses.

In the following Chapter we will use the patterns probabilities computed by using the Bandt and Pompe method in order to characterize the dynamics of the system by means of information-theory measures, such as the Shannon entropy and the MPR-statistical complexity (Martin et al., 2006). In particular, we investigate the gradual change in the dynamics that takes place during the transition from LFFs to coherence collapse when the laser bias current increases.

Chapter 7

Quantifying the statistical complexity in a semiconductor laser with optical feedback

In the previous Chapter, we quantified linear correlations and transition probabilities in a semiconductor laser with feedback, using a method based on ordinal patterns, by which the relative length and ordering of consecutive inter-dropout intervals (i.e. the time intervals between consecutive intensity dropouts) are analyzed, disregarding the precise timing of the dropouts and the absolute durations of the inter-dropout intervals. In this Chapter we extend the characterization of the dynamics of that system by using two nonlinear quantifiers, namely Shannons entropy and MPR statistical complexity measure. We show that this methodology is suitable for quantifying subtle characteristics of the LFFs, and in particular the transition to fully developed chaos that takes place when the laser's pump current is increased. Many studies of optical feedback effects exist, but no systematic quantification of the level of statistical complexity exhibited by these systems, in particular in the regime of chaotic dynamics, exists so far. Our method shows that

the statistical complexity of the laser does not increase continuously with the pump current, but levels off before reaching the coherence collapse regime. This behavior coincides with that of the first- and second-order correlations of the inter-dropout intervals, suggesting that it is these correlations, and not the chaotic behavior, that determine the level of complexity of the laser's dynamics. These results hold for two different dynamical regimes, namely sustained LFFs and coexistence between LFFs and steady-state emission.

As we have shown in Ch. 2, a characteristic feature of LFFs is that, as the laser bias current increases, the average time interval between consecutive dropouts decreases, and the dropouts become increasingly frequent and begin to merge (Heil et al., 1998). Thus, there is a gradual transition through which the output power becomes increasingly irregular with increasing bias current. For large enough bias current no dropouts are observed, but rather a completely irregular intensity time trace arises, a regime which has been termed fully developed coherence collapse (see Ch. 2 for an introduction).

Another characteristic of the LFF regime is that, in a wide region of parameters, it co-exists with stable emission, with the relative durations of the stable emission state and the LFF state depending on the bias current, the feedback strength, and the phase-amplitude coupling factor (α -factor) (Heil et al., 1998, 1999a; Heil, 2000; Hong & Shore, 2005a). The coexistence of LFFs and stable emission has raised the issue of whether the LFFs are a transient dynamics which turns into a sustained one due to the presence of noise. Several studies have focused on characterizing deterministic chaotic features of the dropouts (Martinez Avila et al., 2004; Ray et al., 2006), as well as stochastic properties (Hohl et al., 1995). It has been shown (Davidchack et al., 2000b,a; Torcini et al., 2006; Zamora-Munt et al., 2010a) that the α -factor strongly influences the operation regime of the laser. For small α , the LFFs are transient for all levels of optical feedback, after which the laser settles into a stable operation mode; for intermediate values of α , the regime of sustained LFFs alternates with “windows” of transient LFFs; for large α , the laser operates

in sustained LFFs (Davidchack et al., 2000b,a).

In spite of the vast amount of research done on the LFF instability, the *statistical complexity* of this dynamical regime has, to the best of our knowledge, not been investigated so far. Here we address this issue from the perspective of information theory, which allows us to quantify the complexity of the LFF regime as it approaches fully developed coherence collapse, for increasing intensity of the laser’s pump current.

Most systems in nature are neither completely ordered nor completely disordered, but something in between (see Ch. 4 for an introduction). Within the framework of information theory, the statistical complexity of a system is zero in the extreme situations of complete knowledge (or “perfect order”) and total ignorance (or “complete randomness”). Both are simple situations, as one is fully predictable, and the other one has a simple statistical description. In order to capture the diversity and the rich spectrum of unpredictability occurring between these two extreme situations, many statistical complexity measures have been proposed in the literature (Lempel & Ziv, Jan 1976; Grassberger, 1986; Crutchfield & Young, 1989; Wackerbauer et al., 1994; Pincus, 1995; Lopez-Ruiz et al., 1995; Palus, 1996; Bandt & Pompe, 2002; Martin et al., 2006; Ke & Tong, 2008). These are useful tools for analyzing high-dimensional dynamics presenting underlying, hidden, or unobserved states that might organize the system’s behavior. Statistical complexity measures are particularly useful when there is no prior knowledge of the hidden dynamics. They have been used, for instance, to characterize spatio-temporal patterns (Kaspar & Schuster, 1987), distinguish noise from chaos (Rosso et al., 2007), and identify a transition from a healthy to a diseased state in the brain (Young et al., 2005).

The LFF power dropouts, being a slow modulation of fast high-dimensional pulses, are a potentially interesting dynamical regime to be analyzed with complexity tools. Here, following Martin et al. (2006) and Rosso et al. (2007), and as discussed in Ch. 4, we employ the MPR statistical complexity measure $C[P]$, defined as a functional of

the probability distribution function P that characterizes the state of the system. $C[P]$ is the product of the “disequilibrium”, $Q[P]$, which measures the distance to the equilibrium state, and the normalized Shannon entropy, $H[P]$. Defined in this way, $C[P]$ can be expected to display a maximum somewhere in between $H = 0$ (complete order) and $H = 1$ (complete disorder).

A crucial step for obtaining meaningful results is to define a probability distribution P that fully characterizes the system, i.e. that captures the organization of the hidden fast dynamics underlying the LFF dropouts. While one could just define P in terms of the distribution of either intensity fluctuations or inter-dropout intervals, this would result in neglecting time correlations that may exist between consecutive dropouts. In this Chapter we use the probability distributions, that takes into account the time ordering of the dropouts, obtained in the previous Chapter (Ch. 6) and presented in Rubido et al. (2011). Even though the BP method ignores the precise timing of the dropouts and the absolute duration of the inter-dropout intervals, it reveals, as we show below, interesting new features in the transition from LFFs to fully developed coherence collapse (such as enhanced complexity accompanied by a decrease of the entropy).

7.1 Experiments

The experimental system consists of an AlGaInP Fabry-Perot semiconductor laser (Sharp GH06510B2A) with a nominal wavelength $\lambda_n = 650$ nm, subject to optical feedback from an external mirror. Details of the experimental setup can be found in Ch. 6 (Sec. 6.1).

Power dropouts for three different values of the pump current are shown in Fig. 7.1, whose panel (a) represents the output intensity corresponding to a dynamical behavior where there is coexistence between stable emission and LFFs. As described in Ch. 2 above, within the coexistence region the duration of the LFF intervals

increases with the pump current and the feedback strength. In Fig. 7.1(b) the injection current is high enough to be outside of the coexistence region, and the laser intensity displays sustained LFFs. Due to the increment of the injection current, the time between consecutive dropouts is shorter. Finally, in Fig. 7.1(c), the injection current is high and the laser operates close to coherence collapse, characterized by highly irregular oscillations of the light intensity.

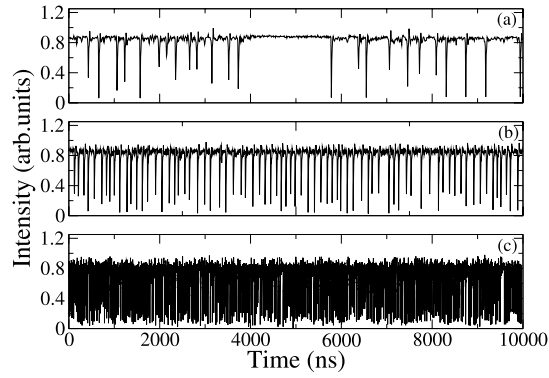


Figure 7.1: Time traces for three different values of the pump current corresponding to three different dynamical regimes: (a) coexistence of LFFs and stable emission, (b) sustained LFFs and (c) transition to coherence collapse. $I_a = 31.20$ mA, $I_b = 32.40$ mA and $I_c = 35.00$ mA. The horizontal scale is the same in the three panels.

Time series with more than 10^4 dropouts were recorded for various values of the pump current. For low pump currents the dropouts are infrequent and very long time series had to be recorded; thus, a small sampling rate was used in the digital acquisition system. For high pump currents the dropouts are more frequent, and shorter time series were recorded with a larger sampling rate. The sampling rates used in the experiments ranged from 250 megasamples/second to 1 gigasample/second.

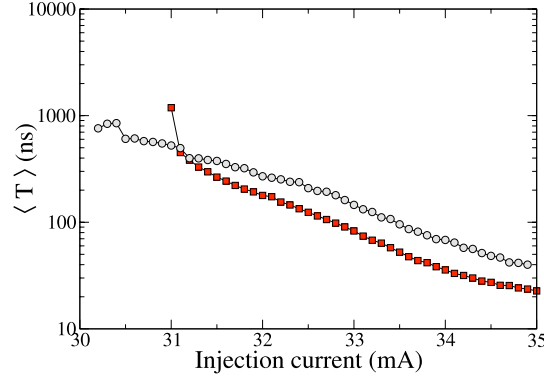


Figure 7.2: Mean value of the inter-dropout interval as a function of the pump current for two different experimental measurements that differ in the alignment of the external mirror, and thus in the optical feedback strength. For one data set (referred to in the text as set I and indicated with circles) the mean inter-dropout interval is longer than for the other data set (set II, squares). This occurs in all the range of variation of the injection current, except at the lowest current values in set II.

7.2 Statistical characterization of the time series

Figure 7.2 displays the mean time between consecutive dropouts, $\langle T \rangle$, as a function of the pump current, for two experimental realizations that differ in the alignment of the external mirror. This results in different couplings between the intra-cavity field and the re-injected field. The two couplings are distinct enough to lead to two different dynamical regimes (sustained LFFs –set I–, and dynamic alternation of LFFs and stable emission –set II–), but similar enough to have a comparable threshold reduction due to the feedback (around 7%). As can be seen in Fig. 7.2, in the two sets of experimental measurements the mean time between consecutive dropouts decreases with the injection current, as mentioned previously. We have adjusted the experimental conditions to be as similar as possible to each other, with

the goal of analyzing data that were different only in their dynamical behavior.

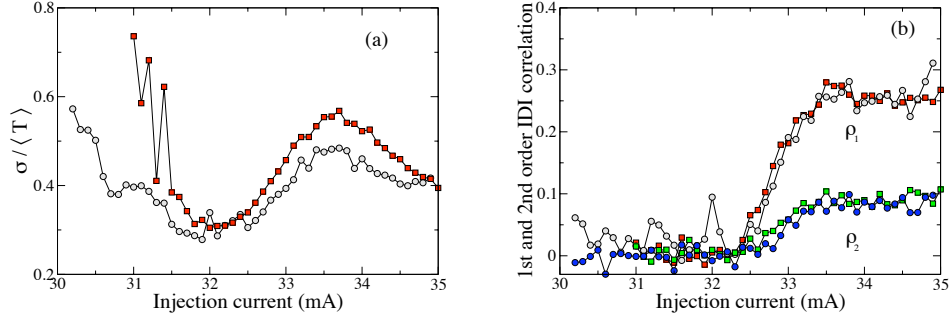


Figure 7.3: (a) Normalized standard deviation of the inter-dropout intervals (IDIs) as a function of the injection current, for two different experimental realizations. (b) First- and second-order IDI correlation coefficients as a function of the injection current, again for two different experimental realizations. Circles correspond to set I and squares to set II.

In the next section we analyze via ordinal patterns the time-series measured under these different conditions and contrast their complexity measures. But before computing the complexity of the time series, we first characterize them statistically. Figure 7.3(a) displays the normalized standard deviation of the inter-dropout interval (or coefficient of variation), $C_v = \sigma / \langle T \rangle$. Note that a decrease of C_v indicates enhanced regularity of the dropouts. Close to the solitary threshold (in the range from 30 to 32 mA) the increase of the injection current results in a decrease of C_v and the system becomes more regular. At an intermediate value of the pump current a minimum of C_v is reached, beyond which the dropouts become increasingly irregular, approaching coherence collapse, as the pump current increases further. As described by Martinez Avila et al. (2004), the pump current affects the fast dynamics, i.e. the picosecond intensity pulses, differently than it affects the slow-modulation, i.e. the power dropouts. The fast pulses play the role of an effective

noise, and thus the variation of the injection current results in a variation of the amplitude of the effective noise. Within that context, the existence of a minimum in the coefficient of variation for an intermediate pump current can be likened with the enhanced regularity of dropouts that arises for an optimal noise level in coherence resonance (Giacomelli et al., 2000; Buldú et al., 2001, 2004).

In Fig. 7.3(a) it can also be noticed that for one set of experimental measures C_v presents large fluctuations at low current values, while for the other set these oscillations are absent. As explained previously, the two sets of observations differ on the alignment of external mirror, and thus in the feedback strength. The large variations of C_v in data set II are due to the occurrence of a regime of coexistence of LFFs and stable emission, which is absent in the other data set. This behavior induces an error on C_v . Another statistical property of the data is the correlation of time intervals between consecutive dropouts (inter-dropout intervals, IDI). The n -th order correlation coefficient between IDIs is defined as:

$$\rho_n = \frac{\langle I_{k+n} I_k \rangle - \langle I_{k+n} \rangle \langle I_k \rangle}{\langle I_k^2 \rangle - \langle I_k \rangle^2}, \quad (7.1)$$

where $\{I_k\}$ is an ordered sequence of IDIs. Figure 7.3(b) shows the dependence of the first- and second-order IDI correlation coefficients on the pump current. A transition from a Markov to a non-Markov process is observed at a value of the pump around 32.5 mA, above which the correlations become non-zero (the second-order correlation being smaller than the first-order one). In what follows we will evaluate and compare the statistical complexity of both data sets.

7.3 Quantifying the statistical complexity

We begin by transforming the sequence of consecutive inter-dropouts intervals $\{T_i, i = 1 \dots M\}$ into a set of D -dimensional “ordinal patterns”, as described in Ch. 4. Since the number of different vectors of dimension D is equal to $D!$, to have a good statistics one must have a large enough number of vectors, such that $M - D \gg D!$.

The last step is to compute the normalized Shannon entropy, $H[P]$, and the MPR statistical complexity, $C[P]$ (see Chap. 4) above.

Figure 7.4 displays H and C for the experimental data set where the feedback level is such that no coexistence is observed at low pump currents (set I); Figure 7.5 displays H and C for the other data set (set II), for which there is coexistence between LFFs and stable emission at low pump currents. Results are presented for various values of the length of the ordinal patterns, D (embedding dimension). Since the experimental data series have about $M = 15000$ dropouts (set I) and $M = 10000$ dropouts (set II), in order to have a good statistics we limit ourselves to $D \leq 5$. We also display the results of analyzing the corresponding surrogate data, which consistently shows $H \sim 1$ and $C \sim 0$.

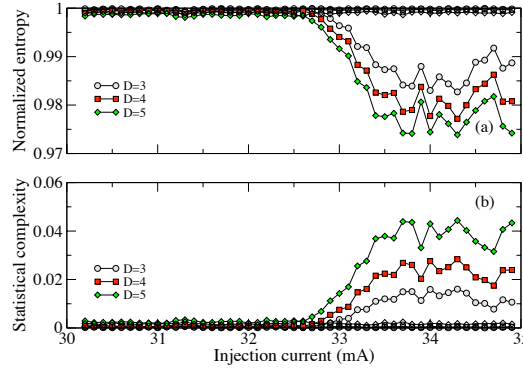


Figure 7.4: (a) Normalized Shannon entropy and (b) statistical complexity measure vs. the laser injection current, for various values of the length of the ordinal patterns, D (embedding dimension). $M = 15000$. The data set is “set I”, for which there is no coexistence of LFFs and stable emission at low injection currents. Empty symbols represent the surrogate data for the filled symbols with the corresponding shape.

It can be observed that in both data sets, a region of enhanced statistical complexity, accompanied by a decrease of the normalized entropy, occurs at high enough

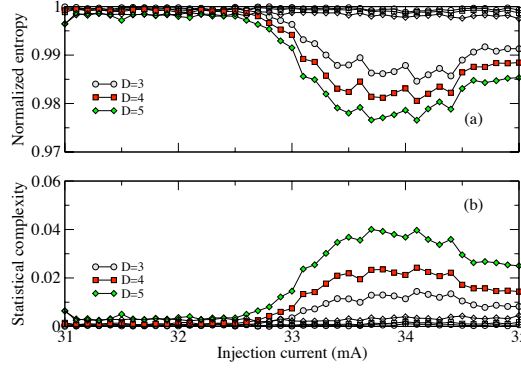


Figure 7.5: (a) Normalized Shannon entropy and (b) statistical complexity measure vs. the laser injection current, for various values of the length of the ordinal patterns, D (embedding dimension). The data set is “set II”, for which there is coexistence of LFFs and stable emission at low injection currents. $M = 10000$. Empty symbols represent the surrogate data for the filled symbols with the corresponding shape.

pump currents, i.e. around the transition between “regular” LFFs (where C_v is minimum, see Fig. 7.3) and highly irregular LFFs (approaching coherence collapse). The increase in the value of the complexity reveals that the distribution of ordinal vectors has a certain structure, in spite of the fact that the dynamics is highly stochastic (note that the normalized entropy is close to 1; however, it decreases in the region of increased complexity). For low injection currents, the coexistence of LFF and stable emission is not detected, as $C \approx 0$ and $H \approx 1$ for both data sets. However, we remark that for the second data set, large oscillations of the normalized standard deviation are seen for low current in Fig. 7.3. This reveals a drawback of the BP methodology, which is due to the fact that the absolute length of the inter-dropout intervals is not considered, but only the relative order is taken into account.

It can be noticed that the analysis with the entropy and complexity measures agrees very well with that of the first- and second-order correlations, in clearly displaying two qualitatively different regimes: one memory-less occurring at low in-

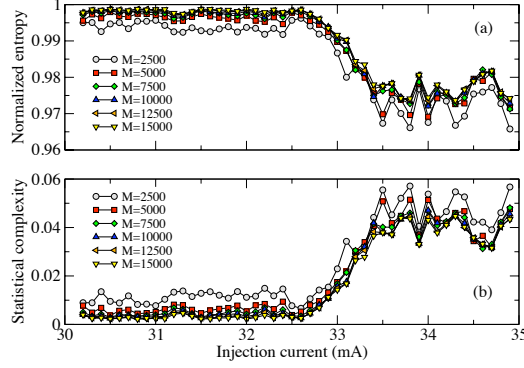


Figure 7.6: (a) Normalized Shannon entropy and (b) statistical complexity measure vs. the laser injection current, for various values of the length of the time series, with $D = 5$. Note that C and H converge with increasing M . The data set used in this figure is set I.

jection currents; and the other occurring at higher current values, for which there are memory effects revealed by time correlations. The second-order correlation coefficient is smaller than the first-order one, while an opposite effect is seen with the complexity measure C , which grows continuously as the ordinal pattern dimension D increases. This lack of convergence with respect to D can be interpreted as due to the finite size of the time series. To check this hypothesis, we display in Fig. 7.6 results of the analysis for fixed D and various values of the length of the time series. The figure shows that both C and H converge with increasing M . In other words, we speculate that if we could record experimentally a long enough time series, such that we could use larger D values with good statistics, convergence would be seen with increasing D , i.e., there would be an optimal D revealing the *finite* length of the memory of the system.

While we present here results only for two data sets, we have done extensive analysis of various experimental realizations and found that the results are robust, in the sense that characterizing the system in terms of the distribution of ordinal

patterns captures enhanced complexity during the transition to coherence collapse; however, the enhanced regularity (i.e. the minimum of the indicator C_v) and the regime of LFF-stable emission coexistence, are not detected.

7.4 Conclusions

We interpret the results in the following terms: at low injection currents the dropouts are infrequent, there are long time intervals between consecutive dropouts, and therefore, the dropouts are statistically independent one of another: there are no memory effects and no patterns or correlations arise in the sequence of consecutive dropouts. For larger injection currents the dropouts are more frequent and there is some memory in the system, i.e. there are time-correlations revealed by $C \neq 0$ and $H \neq 1$. We believe that these correlations might arise because of the finite recovery time: the time when the next dropout occurs will depend on whether the laser fully recovered from the previous dropout or not.

Our results show that the normalized Shannon entropy and the MPR statistical complexity measures are suitable tools for quantifying subtle characteristics of the LFF dropouts, and in particular, the transition to fully developed coherence collapse as the laser bias current increases. However, the coexistence of LFF and stable emission at low bias currents, and the phenomenon of coherence resonance, for which the normalized deviation of the inter-dropout intervals displays a minimum at a certain bias current (Giacomelli et al., 2000; Buldú et al., 2001, 2004), are not detected.

Chapter 8

Quantifying the stochasticity in the dynamics of two mutually coupled semiconductor lasers

When two semiconductor lasers are coupled to one another via mutual injection of their emitted light fields and have sufficiently similar frequencies, they exhibit chaotic dynamics, which furthermore is synchronized between the two lasers. However, since the coupling is subject to delay, synchronization must occur with a lag, and since the system is basically symmetrical, no laser can be the sole leader of the dynamics. In those conditions, a regime of lag synchronization in which the leader and laggard roles alternate between the lasers emerges (Heil et al., 2001). In this Chapter we ask the question of what is the level of stochasticity of the switching between the leader and laggard roles, as a function of the injection current of the lasers. We analyze this switching dynamics in terms of the distribution of forbidden patterns of the alternance time series. The results reveal that the system operates in a stochastic regime, with the level of stochasticity decreasing as the lasers are pumped further away from their lasing threshold. This behaviour is similar to that

exhibited by a single semiconductor laser subject to external optical feedback, as its dynamics shifts from the regime of low-frequency fluctuations to coherence collapse.

We use an approach recently introduced by Amigó et al. (2006) and described in Ch. 4, consisting in analyzing the set of all order patterns of a time series (defined as order sequences of sub-sets of elements of the time series). A random series of infinite length contains all possible order patterns with probability one, whereas in a chaotic time series certain order sequences will never occur due the structure of the phase space in which they evolve. Identifying such *forbidden patterns* in a time series will thus tell us if the series is stochastic or deterministic. This technique has been used to characterize the level (or lack of) stochasticity in logistic maps (Amigó et al., 2006), shift systems (Amigó et al., 2008), and financial time series (Zunino et al., 2009). Here we report on what is, as far as we know, the first application of this method to experimentally generated time series. In our case, as shown below, the leader-laggard dynamics provides us with a natural way of generating a symbolic time series and thus no order patterns must be extracted from the experimental measurements. Furthermore, due to the high-dimensionality of the dynamics of semiconductor lasers subject to delayed optical injection (Ahlers et al., 1998), the number of forbidden sequences eventually drops to zero for sufficiently long time series, and hence we quantify the level of stochasticity in terms of how fast the number of forbidden patterns decays with length. Our results show that, similarly to the case of a single semiconductor laser subject to optical feedback, the dynamics is more stochastic the closer the lasers are to their emission threshold.

8.1 Experimental setup

Figure 8.1 shows a schematic diagram of the setup used in the experiments reported below. Two semiconductor lasers (Mitsubishi ML925B45F) distant 6 meters from each other are bidirectionally coupled via an optical fiber. Coupling is achieved

by means of an optical coupler with 50/50 coupling ratio (10202A-50-FC). The lasers operate at a nominal wavelength $\lambda_n = 1550$ nm and nominal power of 6 mW. The temperature and pump current of the lasers are controlled with an accuracy of 0.01 °C and 0.01 mA, respectively, and are adjusted such that their optical frequencies when isolated are as similar as possible to each other. For temperatures $T_{LD1} = 10.97$ °C and $T_{LD2} = 20.75$ °C, the threshold currents of the solitary lasers are, respectively, $I_{LD1}^{th} = 11.10$ mA and $I_{LD2}^{th} = 11.63$ mA. The laser intensities are captured by high-speed fiber photodetectors with 2 GHz bandwidth (DET01CFC). The received signals are amplified, using a 2 GHz Femto high-speed amplifier, and sent to a 1-GHz oscilloscope (Agilent DS06104A). Note that due to the limited bandwidth of the detectors we are only able to monitor the slow dynamics of the system, which is enough for our study.

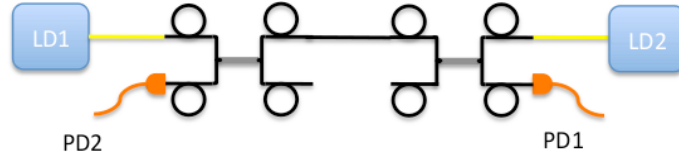


Figure 8.1: Experimental setup. Two semiconductor lasers (LD1 and LD2) inject their emitted light into each other via an optical fiber. PD1 and PD2 are photodetectors.

This setup allows us to control the leader-laggard dynamics of the system. In particular, the relative wavelengths of the lasers in isolation determine which laser leads the dynamics. The wavelengths can be tuned by adjusting the lasers' pump currents. As mentioned in Ch. 3, the laser detuned to higher energies always takes the leader role. However, as we now show, for a large range of parameters, the detuning can be made small enough so that no clear leader exists.

8.2 Experimental results

For the experimental conditions given above, the two otherwise stable semiconductor lasers start pulsing in the form of synchronized power dropouts. The dropouts do not occur simultaneously, but are separated a time ~ 30 ns, corresponding that the time taken by light to travel between the two lasers. When the pump currents of the lasers are adequately fine-tuned, the frequency detuning between them is approximately zero and the leading role of the dynamics alternated between the two lasers, as explained above and shown in Fig. 8.2.

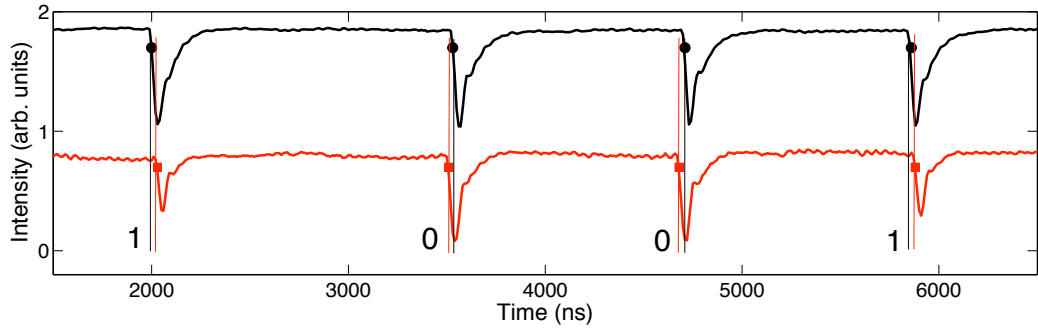


Figure 8.2: Experimental output intensities of the two coupled lasers. Laser LD1 is shown in the top trace and laser LD2 in the bottom trace. The pump current of LD1 is 13.38 mA and that of LD2 is 12.25 mA. The time trace of LD1 has been shifted upwards for clarity. The circles indicate the times at which the dropouts occur. Vertical lines are added at the dropout locations to allow comparison between the dropout times of the two lasers. The numbers at the bottom of the vertical lines indicate the binary value associated with the ordering of the dropouts between the two lasers.

Figure 8.2 portrays a sample pair of simultaneously measured time traces, with the dropouts of each laser identified by the time instant at which the intensity drops below a certain threshold, chosen in order to optimize the detection of the dropouts, while being consistent between the two lasers. In the particular sample shown in the figure, laser LD1 (top trace) leads the dynamics in the first and fourth dropouts,

while laser LD2 (bottom trace) is the leader for the second and third dropouts. A statistical analysis of the data indicates that the leader and laggard roles switch irregularly in time.

In order to quantify how the leader and laggard roles are distributed between the two lasers, we measured the time interval between each pair of synchronized dropouts. Figure 8.3 shows histograms of the inter-dropout intervals for different values of the pump currents of laser LD2, having fixed the value of LD1's pump current. The figure shows that as laser LD2 is pumped at smaller current levels, the

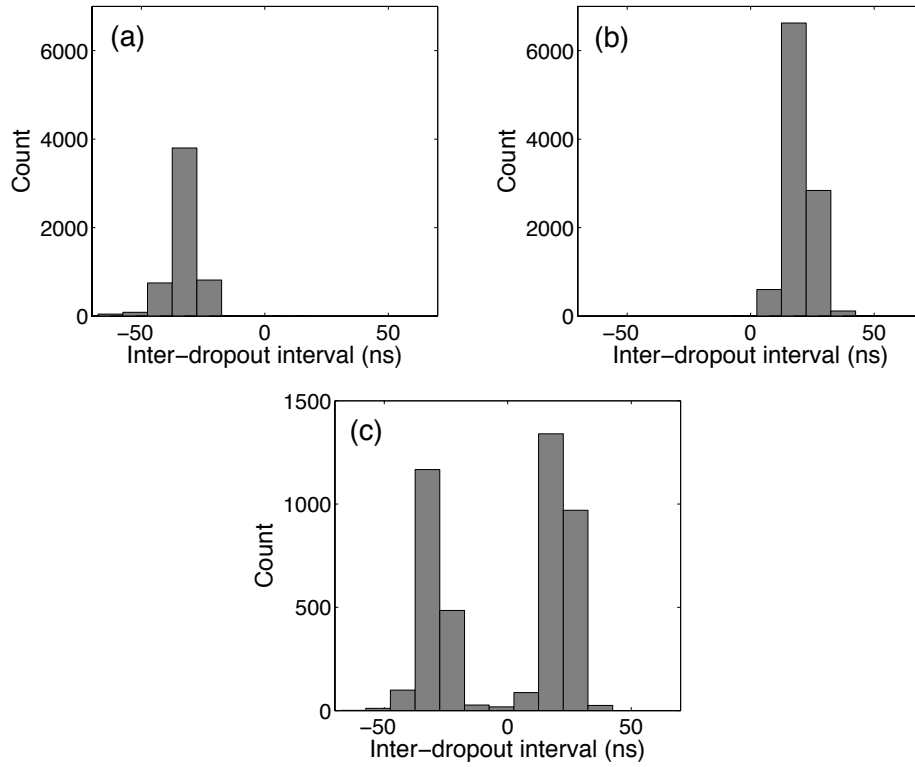


Figure 8.3: Histogram of time interval between dropouts for two coupled lasers for varying pumping of laser LD1. (a) $I_{LD1} = 13.84$ mA, (b) $I_{LD1} = 13.38$ mA, and (c) $I_{LD1} = 12.38$ mA. The pump current for LD2 is $I_{LD2} = 12.25$ mA in all three cases.

leader role shifts from LD2 (plot a) to LD1 (plot b). These situations correspond to the corresponding leading laser having a larger frequency. For an intermediate value of LD2's pump current (plot c) the frequencies of the two lasers can be made to coincide. In that case, the leader role is equally distributed among the two lasers.

Our goal is to determine the level of stochasticity of the irregular leader-laggard alternating dynamics shown in Figs. 8.2 and 8.3(c). To that end, we use the technique of forbidden patterns, described in Ch. 4. In its original implementation this technique used ordinal patterns in order to convert a continuous into a discrete time series (Zunino et al., 2009). In our case, however, there is a natural way of converting the analog character of the laser intensities into a discrete time series. The method is illustrated in Fig. 8.2. Simply put, we assign one of two binary values to each pair of synchronized dropouts, depending on which laser drops in intensity first. If the dropout of LD1 occurs earlier than the one of LD2, we assign a “1”, and in the opposite case we assign a “0”. In that way, we convert the two analog time series corresponding to the laser outputs, to a single binary time series for which we can characterize the statistics of patterns of a certain bit length. By way of example, and additionally as a way of quantifying the leader-laggard transition partially shown in Fig. 8.3, we show in Fig. 8.4 the number of forbidden patterns of length equal to 8 bits versus the pump current of LD1, keeping LD2's pump current constant. The calculation is made by scanning the binarized time series with an 8-bit-long box, and moving one bit at every step. Once all occurring patterns are identified, we compare the list of those patterns with the list of all possible patterns, which equals 256 for a box of length 8. Those patterns out of the 256 that do not appear a single time are labeled as forbidden. For a long enough time series, the absence of forbidden patterns indicates the stochastic character of the dynamics. Figure 8.4 shows the expected result that when one of the laser leads the dynamics, most of the time series consists of either 0's or 1's, and thus a large number of 8-bit forbidden patterns exists, the number being close to 256. On the other hand, in the situation of a perfect leader-laggard alternance, the number of forbidden patterns decreases

rather sharply to 0, even when the length of the time series is finite. Incidentally, the range of pump current values for which the time series is stochastic is rather large, on the order of several tenths of mA.

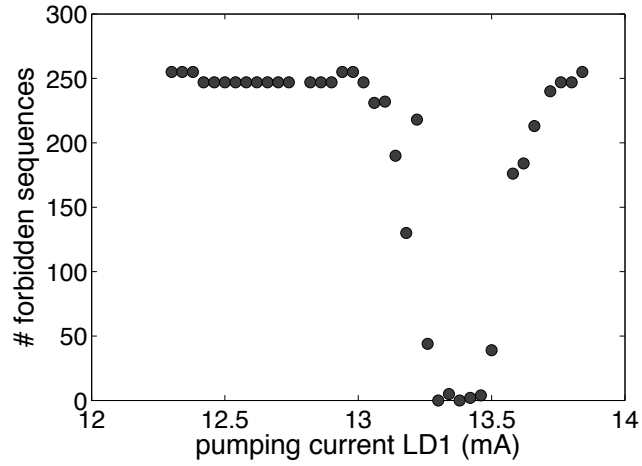


Figure 8.4: Number of forbidden patterns of length equal to 8 bits for increasing pump current of laser LD1. The pump current of LD2 is fixed to $I_{LD2} = 12.25$ mA.

In the remainder of the Chapter we concentrate in the situation in which the leader and laggard roles are equally distributed among the two lasers (Fig. 8.3(c)). The fact that the number of forbidden patterns is zero in that case, as shown in the preceding figure, does not necessarily mean that the time series is stochastic, since semiconductor lasers with delay are known to be highly dimensional chaotic systems (Ch. 2). Chaotic systems should exhibit a non-zero number of forbidden patterns (Ch. 4), but if the chaotic attractor is high-dimensional and the pattern length is too small, they would not appear distinguishable from a stochastic time series. Increasing the pattern length is usually unfeasible, since it would require to increase the length of the measured time series unrealistically (Amigó et al., 2007).

It is known, for instance, that in diode lasers with optical feedback stochasticity is important near threshold (Hohl et al., 1995; Lam et al., 2003), while deterministic

(i.e. chaotic) mechanisms play a relevant role farther away from threshold (Fischer et al., 1996). Given the similarities between the dynamics of a semiconductor laser with optical feedback and two mutually coupled semiconductor lasers, we can expect a similar trend to occur in the latter system. In order to see whether systematic differences between the level of stochasticity exist in our system as we approach the lasing threshold, we plot in Fig. 8.5 the number of forbidden patterns vs. the total series length for three different values of the pump current of LD2, while choosing the pump current of LD1 such that the leader/laggard alternance is split 50/50 among the two lasers in each case. The first feature shown in this figure is that as the

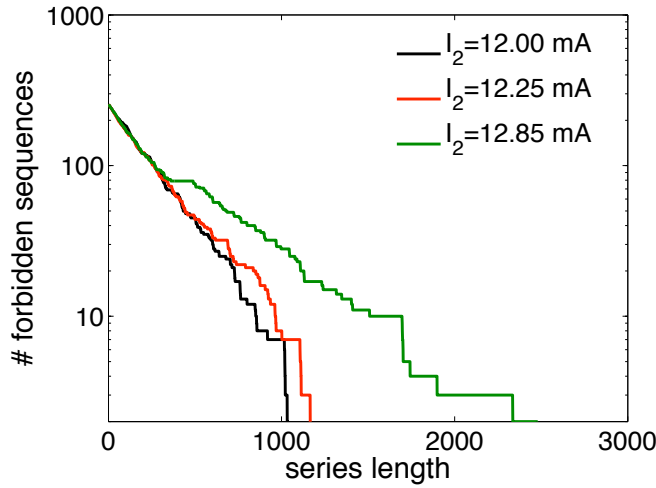


Figure 8.5: Number of forbidden patterns for increasing length of the time series, and for three different values of the pump current of LD2, as noted in the legend. The LD1 pump currents in each case are 12.62 mA (black), 13.38 mA (red) and 12.76 mA (green).

length of the time series being analyzed increases, the number of forbidden patterns decreases in all cases, since it becomes easier to detect rare patterns (Amigó et al., 2007). The rate at which the number of forbidden patterns decreases to zero is however different for different pump strengths: for smaller pump currents, i.e. closer to threshold (black line in Fig. 8.5) the decay to zero is very fast, indicating

that the process is strongly stochastic. As the pump current increases the decay becomes clearly slower, which indicates that the level of stochasticity in the dynamics monotonically decreases as LD2 is pumped further away from its threshold. Thus, these experimental results confirm the expectations that in mutually coupled semiconductor lasers, similar to the case of single semiconductor lasers with optical feedback, the dynamics is more stochastic closer to threshold, while farther away from threshold noise plays a lesser role.

8.3 Numerical simulations

In the previous experimental study the pump current of laser LD1 had to be tuned for each value of LD2's pump current so that 50/50 leader-laggard alternance was maintained as LD2 was pumped increasing farther away from its threshold. It could then be argued that the joint lasing threshold of the system was not being increased monotonically in Fig. 8.5. In order to confirm that indeed the stochasticity of the dynamics increases gradually as we approach threshold, we now perform numerical simulations of an ideal version of the system studied experimentally above. To that end, we use the generalized version of the Lang-Kobayashi model for two bidirectionally coupled semiconductor lasers, described in Ch. 3.

Table 8.1 lists the parameter values used in the numerical simulations described below. For these parameters, the coupled-laser system operates in the LFF regime.

We performed extensive numerical simulations of the model described above, in the case where the two lasers exhibit synchronous power dropouts. Since the model assumes no frequency detuning, the simulations produce naturally complete alternance between the leader and laggard roles for the two lasers. Under those conditions, we studied how the number of forbidden patterns varies as the pump currents of *both lasers* increases further away from threshold. The results are summarized in Fig. 8.6. As in the experimental results reported above, here the number of forbid-

Table 8.1: Laser parameters of the numerical model in the LFF regime

Symbol	Parameter	Value
$I_{1,2}^p$	pump current of LD1,2	$1.02 \cdot \dots \cdot 1.07 \cdot I_{th}$
$\tau_{1,2}$	coupling time path 1	3.4 ns
$\tau_{2,1}$	coupling time path 2	3.4 ns
$\kappa_{i,j}$	Coupling strength	30 ns^{-1}
γ_e	inverse carrier lifetime	$6.89 \cdot 10^{-4} \text{ ps}^{-1}$
γ	inverse photon lifetime	0.480 ps^{-1}
N_0	carrier number at transparency	$1.25 \cdot 10^8$
N_{th}	carrier number at threshold	$1.634 \cdot 10^8$
g	gain parameter	$1.25 \cdot 10^{-8} \text{ ps}^{-1}$
α	linewidth enhancement factor	3.5
β	noise intensity	$1 \cdot 10^{-15} \text{ ps}^{-1}$

den sequences decays to zero slower the farther away the system is from threshold, indicating that the level of stochasticity is larger close to threshold and smaller away from it.

In order to quantify the trend exhibited in Fig. 8.6, we show in Fig. 8.7 how the area under the curves shown in the former figure depend on the injection current, for three different values of the noise intensity, which can be controlled at will in the numerical model. As we have shown in Fig. 8.6, when the injection current increases the area under the curve increases, reflecting the monotonic decrease in stochasticity of the coupled-laser system. Interestingly, while increasing the noise intensity the area under the curve decreases in general, as could be expected, the decrease is more important far from threshold. This indicates that close to threshold the dynamics is mostly dominated by noise and not by deterministic effects, and thus an increase in the noise level does not influence strongly the statistics of the forbidden patterns.

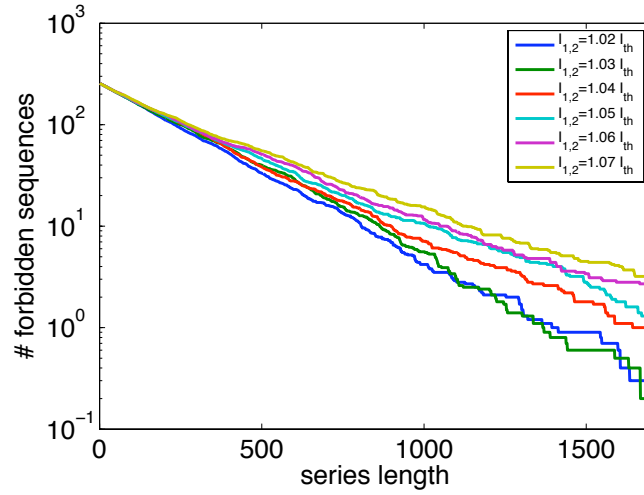


Figure 8.6: Number of forbidden sequences in front of series length and number of surrogated forbidden sequences for different values of the pumping current

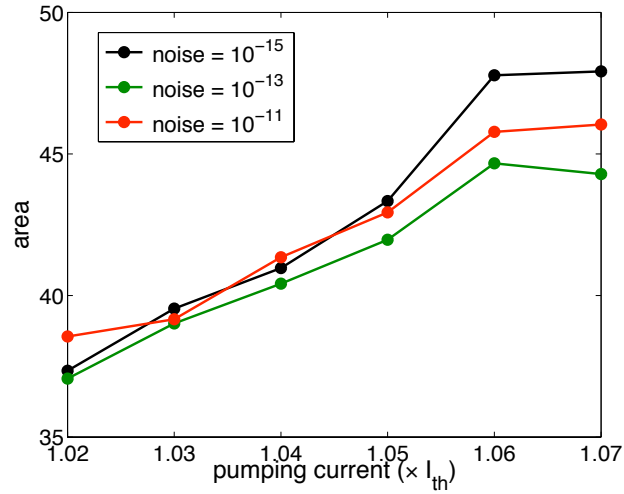


Figure 8.7: Area under the curve of the forbidden patterns of Fig. 8.6. Black line corresponds to a noise intensity of $1 \cdot 10^{-15} \text{ ps}^{-1}$, red line corresponds to a noise intensity of $1 \cdot 10^{-13} \text{ ps}^{-1}$, and green line corresponds to a noise intensity of $1 \cdot 10^{-11} \text{ ps}^{-1}$.

8.4 Conclusions

It is important to determine if the resulting dynamics of a complex system is deterministic or stochastic (for instance, in order to establish whether it is possible to control it). Here we have used a recently proposed method to quantify the level of stochasticity of a time series, based in computing the number of forbidden patterns exhibited by the time series, to address this issue in mutually coupled semiconductor lasers. Both the experimental and numerical results presented here show that the leader-laggard dynamics exhibited by this system is stochastic close to the laser threshold, while the stochasticity is reduced monotonically as the system is pumped further away from threshold. No forbidden patterns are observed for large enough time series in any case, indicating that the deterministic components of the dynamics far from threshold have a high dimensionality.

Chapter 9

Dual-lag synchronization due to path-delay interference

Coupled semiconductor lasers such as the ones studied in this Thesis can be used as model systems to study the behavior of networks of nonlinear dynamical elements. Three-laser systems, for instance, have been shown experimentally to undergo a route to synchronization via clustering (Gonzalez et al., 2007), while theoretical studies have addressed the collective behavior of higher numbers of coupled lasers (D’Huys et al., 2008; Zamora-Munt et al., 2010b). The tendency is to move towards larger systems that can be used as experimental models of complex networks of dynamical elements (Boccaletti et al., 2006). An outstanding issue in complex networks is how information is transmitted between pairs of nodes. Usually, multiple paths exist connecting a given pair of nodes, and thus (if the speed of the coupling signals cannot be neglected) multiple coupling delays are involved in the communication between them. In those conditions, it is not clear what type of synchronized dynamics we should expect: will one of the two coupling delays dominate and lead to a consistent lag between the lasers? If so, under what conditions will that happen? And what will be the dynamics when none of the two delays is dominant? Will the

synchronization lag alternate irregularly between the two delays, similarly to the lag alternance found between two mutually coupled lasers? (Heil et al., 2001; Gonzalez et al., 2007)

In order to address these questions, we have studied experimentally a minimal model system consisting of two optically coupled semiconductor lasers connected unidirectionally via two distinct paths, with different coupling delays. The emitter laser is led to operate in the chaotic low-frequency-fluctuation regime, due to optical feedback. This chaotic dynamics is transmitted simultaneously down the two coupling paths towards the other laser, which operates in a continuous-wave regime when uncoupled from the emitter laser. Injection from the emitter leads to chaotic dynamics in the receiver, synchronized with that of the emitter with a lag that depends on the coupling conditions. When one of the two coupling paths prevails upon the other, in terms of the relative amount of light traveling through them, the delay time associated to the prevailing path dominates, becoming the synchronization lag between the dynamics of emitter and receiver. On the other hand, when no path dominates over the other, a state of *dual-lag synchronization* emerges in which the two coupling delays coexist in the synchronized dynamics of the two lasers.

Our experimental setup allows us to systematically investigate these regime of dual-lag synchronization as a function of the relative coupling strength. Numerical simulations of a delay-differential model further allows us to examine the phenomenon in a wide parameter regime and interpret its existence. Finally, the influence of this lag coexistence on the ability of the system to transmit information is examined both experimentally and numerically.

9.1 Experimental setup

A schematic diagram of the experimental setup is shown in Fig. 9.1. Two semiconductor lasers (Mitsubishi ML925B45F) with a nominal wavelength $\lambda_n = 1550$ nm

are coupled unidirectionally, with LD1 being the emitter and LD2 the receiver. The temperature and pump current of the lasers are controlled with an accuracy of 0.01°C and 0.01 mA , respectively, and are adjusted such that the optical frequencies of LD1 (with its feedback; see below) and LD2 (with injection) are as similar as possible to each other. For temperatures $T_{LD1} = 19.91^\circ\text{C}$ and $T_{LD2} = 19.99^\circ\text{C}$, the threshold currents of the solitary lasers are, respectively, $I_{LD1}^{th} = 11.10\text{ mA}$ and $I_{LD2}^{th} = 11.63\text{ mA}$.

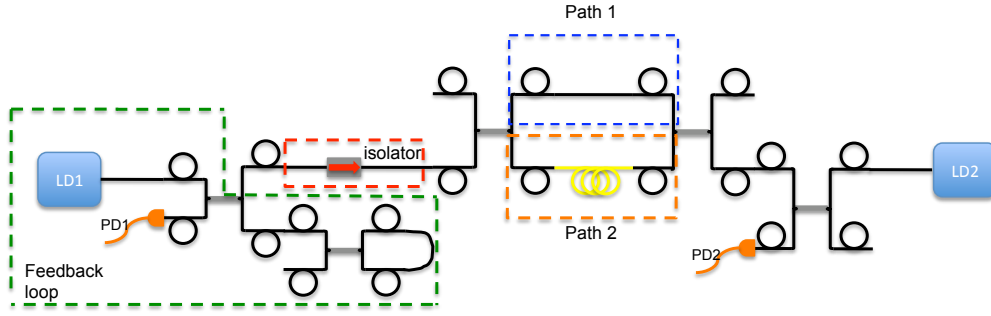


Figure 9.1: Experimental setup of two semiconductor lasers coupled unidirectionally via two paths of different lengths. LD1 is the emitter laser and receives optical feedback via a closed loop. LD2 is the receiver laser. PD1 and PD2 are photodetectors, and the optical isolator ensures unidirectionality. The grey segments represent optical couplers, black lines denote optical fibers and yellow lines free-space propagation of light.

The laser LD1 is subject to delayed feedback from the closed loop shown at the left side of Fig. 9.1, whose length (10 m) provides for a feedback time of 55 ns. The output of this laser is injected, in a unidirectional coupling configuration, with LD2 via two different paths with two distinct delays, with $\tau_1 = 65\text{ ns}$ for path 1 and $\tau_2 = 97\text{ ns}$ for path 2, corresponding to fiber lengths of 12 m and 18 m, respectively. In order to control the relative influence of the couplings we introduce variable optical attenuators in the two paths. The reduction of the threshold current of laser LD1 due to its feedback is 4.2%. The reduction of the threshold current of laser LD2 due to the injection through path 2 is 0.89%, and the one due to injection through

path 1 ranges from 1.86% to 0.05%. The laser intensities are captured by high-speed fiber photodetectors with a bandwidth of 2 GHz (DET01CFC). The electrical signals received are amplified, using 2 GHz high-speed amplifiers (Femto), and sent to a 1-GHz-bandwidth oscilloscope (Agilent DS06104A) and a power spectrum analyzer (Anritsu MS2651B). Due to the relatively small bandwidth of the detectors, we are only able to show the slower dynamics of the system, which is enough for our study.

9.2 Experimental results

Due to the delayed feedback mentioned above, the laser LD1 oscillates chaotically in a regime of low-frequency fluctuations as seen repeatedly in this Thesis and explained in Ch. 2. This chaotic behavior is injected into LD2 via the two different paths, as described in the previous section. In those conditions, synchronization between the two lasers can be achieved when one or both paths are switched on, provided the transmission strength is large enough. In order to characterize the quality of synchronization between emitter and receiver, and to determine which coupling delay time (if any) dominates the synchronized dynamics, we calculate the cross-correlation function between the (filtered) time series of the light detected by the two photodiodes:

$$C(\Delta t) = \frac{\langle [I_1(t) - \langle I_1 \rangle][I_2(t + \Delta t) - \langle I_2 \rangle] \rangle}{\sqrt{\langle [I_1(t) - \langle I_1 \rangle]^2 \rangle \langle [I_2(t) - \langle I_2 \rangle]^2 \rangle}}. \quad (9.1)$$

The left plots in Fig. 9.2 show the cross-correlation function between the two laser outputs for varying levels of coupling in the two paths. Figure 9.2(a) corresponds to the case where path 2 is blocked; accordingly, the highest cross-correlation peak occurs at τ_1 , which means that laser LD1 leads LD2 with a lag equal to τ_1 . In plots (b) to (e) the path 2 is open with a relatively low attenuation, while the attenuation of path 1 is progressively increased, until that path is completely blocked in Fig. 9.2(e). Correspondingly, a peak in the cross-correlation function at τ_2 (which is the flight

time along path 2) appears and eventually dominates in the cross-correlation function. For an intermediate value of the attenuation (10 dB, Fig. 9.2(c)) the two paths are approximately equivalent and the cross-correlation function exhibits two coexisting global maxima at τ_1 and τ_2 , separated by a shallow valley whose small relative depth is a consequence of the filtering of the time series, as we can verify from simulations of the theoretical model described below. In this regime, no single coupling delay dominates over the other, but they both coexist in the synchronized dynamics of the system. Note that the value of the cross-correlation at this two time lags is on the order of 0.75, corresponding to a significant level of synchronization (in the two single-path limits –plots (a) and (e)– the cross-correlation scarcely reaches 0.80).

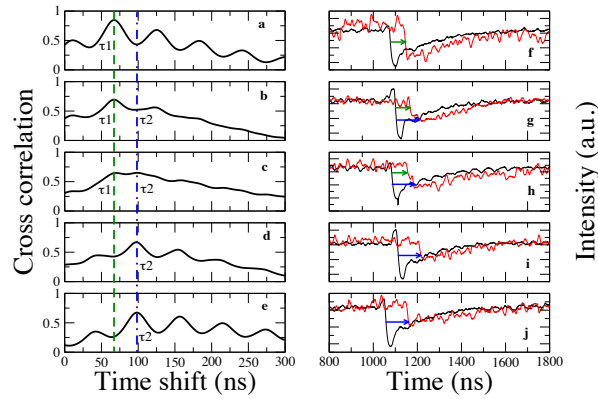


Figure 9.2: Experimental cross-correlation function between LD1 and LD2 (left column) and corresponding time traces of the output intensities (right column) for different values of coupling in the two paths. In panels (a,f) only path 1 is switched on, while in panels (e,j) only path 2 is activated. The attenuation of path 2 is constant and equal to 5 dB in panels (b-e) and (g-j), while the attenuation of path 1 is 5 dB in panels (a,f) and (b,g), 10 dB in panels (c,h), and 15 dB in panels (d,i).

In order to establish the nature of the lag-coexistence scenario revealed in Fig. 9.2(c)

(in particular, to determine if this regime corresponds to a lag alternance similar to that occurring in two mutually-coupled lasers (Heil et al., 2001)), we plot in the right panels of Fig. 9.2 the time series of the two laser intensities. When only one of the paths is switched on (Fig. 9.2(a,f) and (e,j)), the dropouts exhibit the usual single-lag synchronization dynamics, in which LD2 follows LD1 with a lag τ_1 or τ_2 depending on which one is the dominating path. This behavior, with a clear delay of τ_1 or τ_2 in the dropouts of LD2 after those of LD1, even when the two paths are open, provided that one path dominates over the other (Fig. 9.2(b,g) and (d,i)). On the other hand, in the transition between the τ_1 - and τ_2 -dominated regimes, during which the two lags coexist in the cross-correlation function (Fig. 9.2(c)), the dropouts of LD2 are qualitatively different. In principle one could expect that in this lag-coexistence regime, a fraction of the LD2 dropouts would follow LD1 with a delay τ_1 , and the rest would follow LD1 with delay τ_2 . This, however, is not what happens, as shown in the time series plotted in Fig. 9.2(g,h). In this figure the dropout of LD2 (red line) consists of a first fall in intensity that follows LD1 with a delay τ_1 , after which the intensity of LD2 remains approximately constant for a short instant, until finally there is a second fall in intensity that follows the original LD1 dropout with a delay τ_2 . This behavior is consistent for all LD2 dropouts. Thus, although the cross-correlation function is here similar to the case of two bidirectionally coupled lasers, which also has two peaks, this does not imply that the dynamical behavior is the same. In the case of bidirectional coupling, the two peaks in the cross-correlation imply a (random) alternance in time between the leader and laggard role of the dynamics, and not a modification of the shape of the dropouts, as happens in the dual-lag synchronization regime occurring in this case.

9.3 Numerical simulations

In order to verify the nature of the dual-lag synchronization regime described above, it would be helpful to increase the difference in the two coupling paths, which should

increase the duration of the plateau between the two falls in the intensity of LD2 that we interpret to be occurring during the LD2 dropouts, and which would give rise to the lag-coexistence observed in the cross-correlation function. However, technical reasons prevented to vary in a systematic manner the delay times, since laser coupling was made by optical fibers, and we would need to have a sufficiently large number of fibers of increasing length. In order to circumvent this requirement, we resorted to numerical simulations of the system, which is known to be accurately described by the Lang-Kobayashi model for moderate feedback strengths and single-mode operation (conditions which approximately hold in our experiment). The generalized Lang-Kobayashi model that we use is the one described in Sec. 3.2.1 but, the coupling term in Eq. (3.8), has been modified in order to include both coupling delay times τ_j and coupling strengths κ_j , for the two paths $j = 1, 2$. So, the differential equation for the electric field of the receiver laser reads as:

$$\frac{dE_2}{dt} = \frac{1+i\alpha}{2}(G_2 - \gamma_2)E_2(t) + \sum_j \kappa_j e^{i(\Delta\omega t - \omega_j \tau_j)} E_1(t - \tau_j) + \sqrt{2\beta N_2} \xi_2(t) \quad (9.2)$$

The parameters used in the numerical simulations are given in Table 9.1. For these parameters the emitter laser operates in the LFF regime. Here we consider a detuning $\Delta\omega = \omega_1 - \omega_2 = 15.89$ GHz between the lasers. Figure 9.3(a-e) shows the numerically computed cross-correlation functions between the filtered time series of the lasers, and Fig. 9.3(f-j) reproduce the corresponding time traces. In order to simulate the experimental filter (due to the relatively small bandwidth of our experimental setup) we filter the output intensities with a fourth-order Butterworth filter with a cutoff frequency of 100 MHz. The numerical results displayed in the figure qualitatively reproduce the experimental results. In particular, the simulations show that in the dual-lag synchronization regime (Fig. 9.3(c,h)), the LD2 dropouts consist of two intensity falls occurring at times τ_1 and τ_2 after the corresponding LD1 dropout, separated by a plateau. Numerical simulations also allow us to examine the dynamics at an arbitrary temporal resolution. In the absence of filtering, the cross-correlation function exhibits more clearly defined peaks, but the dual-lag syn-

Table 9.1: Laser parameters of the numerical model

Symbol	Parameter	Value
$I_{1,2}^p$	pump current of LD1,2	$1.01 \cdot I_{th}$
τ_1	coupling time path 1	65 ns
τ_2	coupling time path 2	97 ns
τ_f	feedback time	55 ns
γ_e	Inverse carrier lifetime	$6.89 \cdot 10^{-4} \text{ ns}^{-1}$
γ	Inverse photon lifetime	0.480 ps^{-1}
N_0	carrier number at transparency	$1.25 \cdot 10^8$
N_{th}	carrier number at threshold	$1.634 \cdot 10^8$
g	gain parameter	$1.25 \cdot 10^{-8} \text{ ps}^{-1}$
α	linewidth enhancement factor	4.0
β	spontaneous emission rate	$1 \cdot 10^{-15} \text{ ps}^{-1}$

chronization behavior is not evident in the unfiltered time series (results not shown).

In order to verify that the plateau in the LD2 dropout shown in Fig. 9.3(h) is not an artifact, we increased substantially in the numerical model the difference between the two coupling delays. The result of this test is displayed in Fig. 9.4, which shows the time traces of a pair of corresponding dropouts for two different values of τ_2 : 165 ns in plot (a), and 265 ns in plot (b), while $\tau_1 = 65$ ns in the two cases. Note that when we increase the coupling time of path 2, the plateau of the LD2 dropout increases correspondingly. Thus these simulations show clearly that the dual-lag dynamics is due to combined dropouts in LD2, consisting of two falls at the two lag times separated by a plateau.

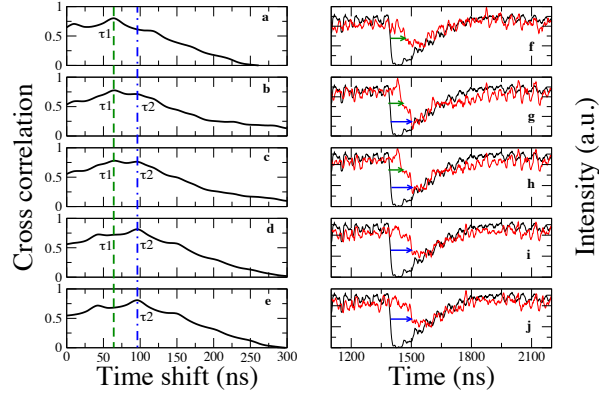


Figure 9.3: Numerical cross -orrelation function between LD1 and LD2 (left column) and the corresponding output intensities (right column) for different values of the coupling strengths: (a,f) $\kappa_1 = 0 \text{ ns}^{-1}$, $\kappa_2 = 40 \text{ ns}^{-1}$ (a,f), (b,g) $\kappa_1 = 20 \text{ ns}^{-1}$, $\kappa_2 = 40 \text{ ns}^{-1}$, (c,h) $\kappa_1 = 40 \text{ ns}^{-1}$, $\kappa_2 = 40 \text{ ns}^{-1}$, (d,i) $\kappa_1 = 60 \text{ ns}^{-1}$, $\kappa_2 = 40 \text{ ns}^{-1}$, and (e,j) $\kappa_1 = 40 \text{ ns}^{-1}$, $\kappa_2 = 0 \text{ ns}^{-1}$ (e,j). The feedback strength is fixed at $\kappa_f = 60 \text{ ns}^{-1}$. Other parameters are given in Table 9.1.

9.4 Chaotic communications

Many studies have addressed the transmission of information between two chaotic lasers coupled unidirectionally via a single path. In this section we want to study the viability of chaotic communications when the coupling between the lasers is done via two different paths, in the light of the dual-lag synchronization scenario described above. First we ask if the experimental setup presented in Fig. 9.1 above is able to filter a periodic signal introduced in the emitter laser, even in the case of dual-lag dynamics. This filtering mechanism is called chaos-pass filtering (Fischer et al., 2000; Murakami & Shore, 2005). As shown in Fig. 9.5, when a periodic modulation of frequency 1.20 MHz is applied to the pump current of the emitter laser, the receiver laser filters out the modulation, and no corresponding peak in the

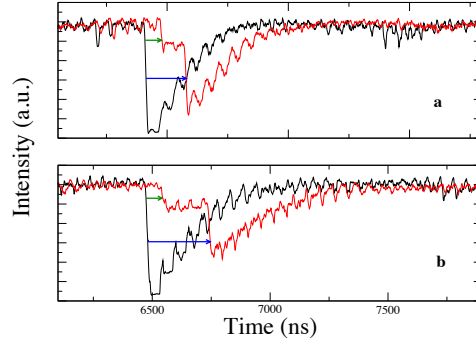


Figure 9.4: Numerical output intensities for different coupling times in path 2. The delay time is 165 ns in (a), and is 265 ns in (b). The coupling parameters are $\kappa_1 = \kappa_2 = 40 \text{ ns}^{-1}$, and $\kappa_f = 30 \text{ ns}^{-1}$. The other parameters are given in Table 9.1.

power spectrum of the laggard laser can be observed. Note that this experimental result is obtained in the dual-lag regime (i.e. both paths are equally synchronized).

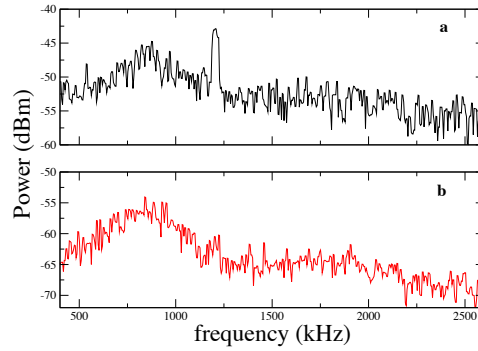


Figure 9.5: Spectral response of the receiver laser (b) to a modulation introduced in the emitter laser (a), in the case where both delays dominate equally the dynamics (dual-lag synchronization).

Once we have seen that chaos-pass filtering is possible between two semiconductor

lasers unidirectionally coupled through two lag times, we now ask for the viability of recovering a message for the different setup configurations (i.e only one path or both switched on). Figure 9.6 displays numerical results that evaluate the effectiveness of the message recovery for different values of $\frac{\Delta\kappa}{\kappa} = \frac{\kappa_2 - \kappa_1}{\kappa_2}$, when a non-periodic signal (specifically, a return-to-zero bit train) is introduced in the pump current of laser LD1. The message is introduced with an amplitude equal to 2.5% of the pump current, and is decoded by subtracting the light emitted by the two lasers, taking into account the delay between the signals. The subtracted signal is filtered with a fourth-order Butterworth low-pass filter. In order to quantify the effectiveness of the recovered message we calculate the success rate between the input and output message, as the fraction of bits that are successfully recovered by LD2. In order to compute this quantity, the output message is binarized by defining a threshold, such that when the recovered message is larger than this threshold we assign a '1' and when it is smaller we assign a '0'. The left panel of Fig. 9.6 displays the success rate for varying values of the coupling asymmetry between the two paths, $\frac{\Delta\kappa}{\kappa}$, and for three different values of the difference between coupling delays. The maximum value of the success rate occurs for sufficiently large coupling strength asymmetry, which corresponds to a situation in which standard single-lag synchronization occurs, and the choice of time shift to be applied in the message recovery is simple. As we approach the dual-lag regime, on the other hand, the success rate diminishes sharply. Thus, even though the receiver laser exhibits good chaos-pass filtering capabilities in the case of dual-lag synchronization, the coexistence of two lags in this case prevents the system from recovering the message. The time traces corresponding to three specific values of the coupling strength asymmetry (the two single-lag extremes and the dual-lag case) are shown in the right panels of Fig. 9.6. As expected, when the difference between the coupling delay times diminishes the success rate increases, because the interference effects degrading message recovery diminish.

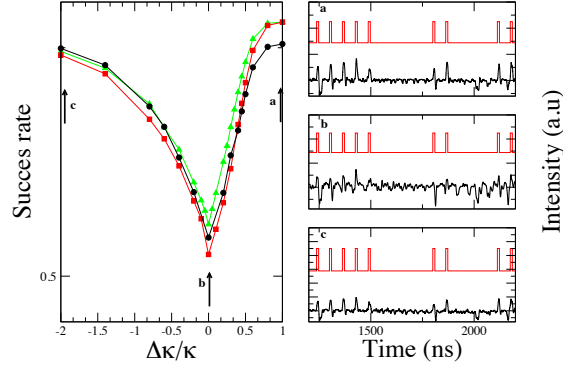


Figure 9.6: Left: Numerically computed success rate versus coupling asymmetry for three values of the difference between coupling delay times: 75 ns (squares), 65 ns (circles), and 55 ns (triangles). Right: input message (red) and recovered message (black) for three values of $\frac{\Delta\kappa}{\kappa}$, marked with arrows in the left plot (for the case of the squares in the left panel). For the recovery, the time series in the receiver laser is shifted a time lag that corresponds to the delay of the path with strongest coupling. Parameters are those given in Table 9.1, plus $\kappa_2 = 40 \text{ ns}^{-1}$.

9.5 Conclusions

We have examined the synchronized dynamics of two semiconductor lasers coupled unidirectionally via two different paths. The emitter laser operates in an intrinsically chaotic regime in the form of irregularly occurring power dropouts (low-frequency fluctuation regime), which generates chaotic behavior in the receiver. Our experimental results have revealed a transition a regime in which the synchronized dynamics is dominated by path 1, and another one dominated by path 2. In the transition region where both synchronization takes place via the two paths, two lags corresponding to the two coupling delays coexist, as shown by the cross-correlation function. Our experiments and numerical simulations have shown that this dual-lag

synchronization regime does not consist in an alternance between the two lags, as happens usually in mutually coupled semiconductor lasers (Heil et al., 2001; Gonzalez et al., 2007), but in a dynamics through which the power dropouts of laser LD2 are formed by two falls in the laser intensity, occurring after the two coupling lags, separated by a plateau. This dynamical regimes does not prevent the receiver laser from performing chaos-pass filtering of an input modulation in the emitter laser's output, but does prevent a successful recovery of the message.

Chapter 10

Zero-lag synchronization and bubbling in bidirectionally coupled lasers

We have seen in Ch. 8 that when two identical semiconductor lasers are bidirectionally coupled over a finite distance, the time delay associated with the coupling leads to spontaneous symmetry breaking, and synchronization of the output intensities of leader-laggard type can occur (Heil et al., 2001). It has also been shown that using a relay in the middle of the optical path between both lasers can result in stable zero-lag (isochronous) synchronization of the laser intensities. This relay can be an active one like a third laser, so that the coupling scheme consists of three lasers coupled along a line where the central laser acts as the relay (Fischer et al., 2006; Peil et al., 2007; Landsman & Schwartz, 2007), or a passive one like a semitransparent mirror (Vicente et al., 2007). However, even with an overall stable isochronous synchronization of two identical lasers, intermittent events of desynchronization can still occur. These events are induced by system intrinsic noise and by parameter mismatches, and have been called bubbling (Ashwin et al., 1994; Sauer & Kaiser,

1998). The bubbling events can be attributed to transversely unstable periodic orbits embedded in the attractor located in the overall stable synchronization manifold (Venkataramani et al., 1996; Nagai & Lai, 1997; Flunkert et al., 2009). The local instability forces the system's trajectory to temporarily leave the synchronization manifold until resynchronization occurs. In this Chapter we want to connect the overall synchronization quality to the occurrence of intermittent desynchronization events with a quantitative experimental approach.

10.1 Experimental setup

In order to obtain zero-lag synchronization behavior we employed the scheme depicted in Fig. 10.1.

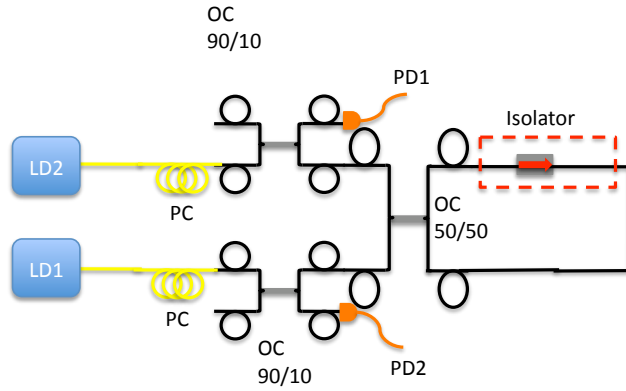


Figure 10.1: Schematic experimental setup. PC: polarization controller, PD: fast photodetector, OC: optical coupler, OI: optical isolator.

The fiber-based setup consists of two similar Eblana discrete mode semiconductor lasers operating at a nominal wavelength of approximately $\lambda = 1540$ nm, coupled symmetrically via a relay fiber loop. This loop accounts for symmetric feedback and coupling, respectively, and in that way functions as a semitransparent mirror.

Due to the 50/50 optical coupler used to combine both laser outputs in the loop, we have identical feedback and coupling strengths. It has been shown (Jiang et al., 2010; Hicke et al., 2011), that asymmetries in coupling strengths can lead to a significant decrease in overall synchronization quality. Therefore, our highly symmetric setup provides near-optimal conditions for our investigation of the synchronization dynamics. In addition, the overall symmetry of our setup leads to equal delay times for feedback and coupling, respectively. By autocorrelation analysis the delay time in our setup was determined to be $\tau = 73$ ns (see Fig. 10.2). We introduced polarization controllers (PC) in both laser lines to adjust the polarization for coherent feedback and therefore optimum coupling. Inside the coupling and feedback loop we placed an optical isolator in order to assure a single propagation direction in the loop and avoid interference effects.

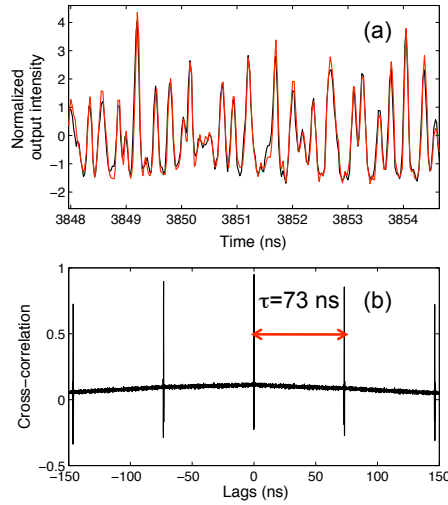


Figure 10.2: (a) Output intensity of the two lasers exhibiting isochronal synchronization at $I_p = 12mA$ (for which the laser operates in the LFF regime) and (b) cross-correlation between output laser intensities showing a maximum for lag equal to zero.

The spectral characteristics of both lasers were adjusted by temperature varia-

tion in order to assure zero spectral detuning, i.e. maximum overlap of the optical spectra. As mentioned in Ch. 1 the laser wavelength changes when the temperature is varied. It is also well known that when the pump current is increased the laser wavelength also increases. In Fig. 10.3 we show the contour plot of the wavelength behavior under pump current and temperature variation for the lasers used in the experiments, in order to point out the strong control we have over the laser wavelength.

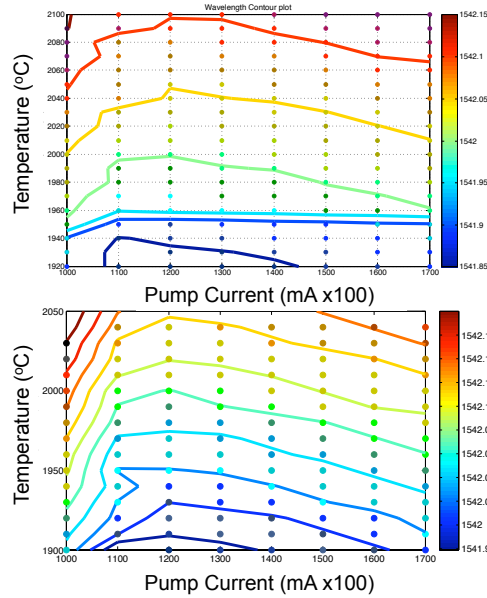


Figure 10.3: Contour plot of the wavelength behavior under pump current and temperature variation for the two lasers used in the experiments.

In order to show how we have achieved zero detuning between the lasers, at a given pump current, we depict the wavelength evolution under temperature variation for the two lasers (see Fig. 10.4). Note that for every wavelength one can find a pair of temperatures (one for each laser) where the zero detuning condition is achieved.

The laser temperatures and pump currents were controlled by a Thorlabs PRO8000

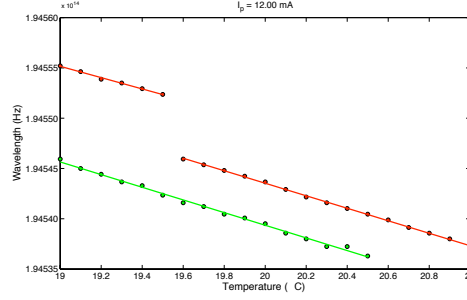


Figure 10.4: Wavelength vs temperature behavior for the two lasers used in the experiments.

diode laser controller with an accuracy of $\Delta T = \pm 0.01$ C and $\Delta I_p = \pm 0.01$ mA. We measured the laser outputs by using fast Miteq Dr-125G-A photodetectors (PD) with 13 GHz bandwidth. The intensity output timetraces were recorded using a LeCroy WaveMaster 816Zi oscilloscope with a sampling rate of 40GS/s. With a time resolution that high we can resolve very fast dynamics on a picosecond-timescale and observe and distinguish very short intervals of synchronization or unsynchronized behavior with unprecedented detail. We analyze the synchronization behavior of the coupled lasers for a pump current range of $I_p = 12 - 17$ mA which, for our setup and parameters corresponds to $I_p \approx 1.0 - 1.5 I_{sol,thr}$, where $I_{sol,thr}$ is the solitary lasing threshold. This current range leads for our operational parameter to two different dynamical regimes: Low Frequency Fluctuations (LFF) (Sec. 2.1.2) and full Coherence Collapse (CC) (see also Sec. 2.1.2). It is well-known that the dynamical properties of those two regimes are much different. Here, we investigate the different synchronization dynamics in these two regimes.

10.2 Zero-lag synchronization and bubbling

With our setup we were able to achieve high-quality zero-lag synchronization. Figure 10.5(a) depicts a typical experimental timetrace of both lasers, showing isochronously synchronized intensity dynamics in a fast time scale. The otherwise near-perfectly synchronized time series exhibit one distinct short desynchronization event (which we identify as a bubbling event below), also clearly visible in the intensity difference (Fig. 10.5(b)).

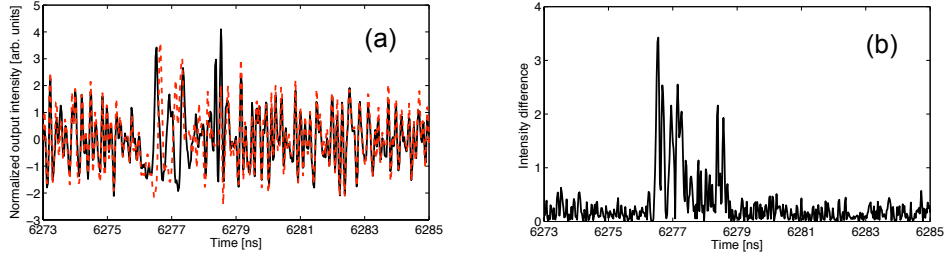


Figure 10.5: (a) Experimental time series of synchronized fast intensity dynamics of the two coupled lasers operating in the coherence collapse regime. The time series exhibit one short desynchronization event and fast resynchronization. (b) shows the corresponding timetrace of the normalized intensity difference (synchronization error) of both lasers.

One can quantify the degree of synchronization between two time series by using the cross-correlation function:

$$C(\Delta t) = \frac{\langle [I_1(t) - \langle I_1 \rangle] [I_2(t + \Delta t) - \langle I_2 \rangle] \rangle}{\sqrt{\langle [I_1(t) - \langle I_1 \rangle]^2 \rangle \langle [I_2(t) - \langle I_2 \rangle]^2 \rangle}} \quad (10.1)$$

where $\langle . \rangle$ means averaging over time. Another possibility is to calculate the normalized synchronization error (i.e. intensity difference). To further account for the fast dynamical fluctuations we integrate and normalize the synchronization error over shifting windows of one delay time τ . An accessible measure is then the mean value

of this integrated normalized intensity difference $\chi = \left\langle \frac{1}{\tau} \sum_{\tau} \frac{|I_1 - I_2|}{\langle I_1 + I_2 \rangle} \right\rangle$.

10.2.1 The role of detuning

We are now interested in the effect of the detuning on the synchronization quality. Understanding how the robustness of the synchronization is affected by parameter mismatches is important in order to improve the synchronization quality of real implemented setups. In Fig. 10.6 we show the behavior of the cross-correlation coefficient at zero lag (blue dots) and at the lags corresponding to the delay coupling time (red and green dots), as a function of the relative detuning between lasers. We observe a region where the synchronization is achieved (correlation values going up to 0.8) surrounded by a region where synchronization quality is clearly low. The region with high correlation coefficient, marked by the vertical dashed lines (black), is the so-called locking region and has a width of around of 20 GHz.

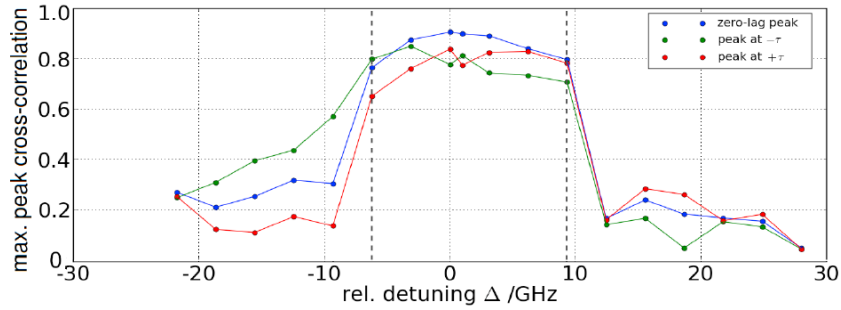


Figure 10.6: Cross-correlation coefficient at zero lag (blue dots) and at lags corresponding to the delay coupling time (red and green dots) as a function of the relative detuning between lasers. The locking region is denoted by the dashed line.

10.2.2 The role of pump current

In order to focus only on the effect of pump current on the synchronization quality, we have kept the detuning at zero. Figure 10.7 depicts the cross-correlation at zero lag (black circles) and the mean of the integrated synchronization error (blue diamonds) versus the applied pump current. We notice almost linear characteristics of both quantities, which behave of course in an inverse manner. We now want to find the mechanism responsible for the overall decline of synchronization. Therefore we analyze the fast timescale synchronization dynamics and connect the occurrence of high-frequent short desynchronization events with the decrease in synchronization quality.

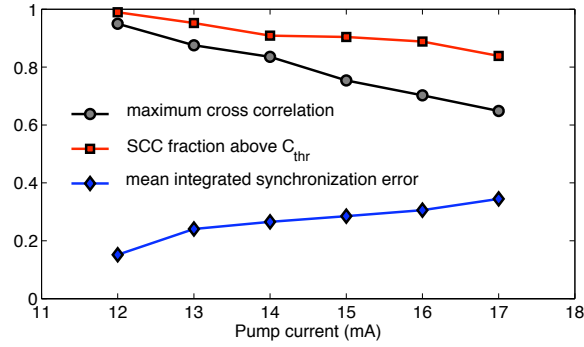


Figure 10.7: Cross-correlation at zero lag $C(0)$ (black circles), fraction of the sliding-cross-correlation above the correlation-threshold of $C_{thr} = 0.5$ (red squares) and mean integrated synchronization error χ (blue diamonds), respectively, versus the applied pump current.

We qualify a time interval as desynchronized by considering the momentary synchronization error, as well as by calculating a sliding-window cross-correlation (SLCC) as local synchronization measures. For that we choose a window size of 1 ns and a step size of 0.1 ns, to be able to distinguish short-term events, calculate the standard cross-correlation function for this window, and move the window by one step. As a

result we obtain a time trace of (local) cross-correlation values. A significant drop of the sliding cross-correlation means that a desynchronization event has occurred.

We will follow three different approaches: First, we investigate the time series of the output intensities and the corresponding sliding cross-correlation, and draw conclusions about general features of the synchronization dynamics in the LFF and coherence collapse regime, respectively. Second, we compare the distribution function of the sliding cross-correlation for each input current value and make statements about the changes in synchronization and desynchronization behavior induced by an increase in the pump current. Further, we analyze the evolution of the fraction of synchronized dynamics in respect to the total length of the SLCC time series. For that we have to introduce a correlation threshold C_{thr} for the cross-correlation. For sliding cross-correlation values below this threshold we do not consider the time-window as an interval of synchronized behavior. Third, we take an event-based approach and identify bubbling by local SLCC value using two additional thresholds: since the stepsize for the SLCC has to be small to achieve a sufficient resolution of short events, ultrashort dips may occur in this function. To filter those fluctuations out we have to introduce a threshold for a minimum duration of the bubbling events ΔT_{thr} that has to be more or less arbitrary. A third threshold necessary for the analysis of our time series is a connectivity threshold IEI_{thr} which is the maximum length for the inter-event interval to consider two isolated desynchronization events as part of a single longer one. These processing parameters lead us to statistical data for bubbling duration and inter-event intervals.

We start by studying the time traces of the laser intensities, together with the corresponding sliding cross-correlation. We are interested in the characteristics of desynchronization in the LFF as well as in the CC regime. Therefore we look into the dips in the SLCC time series. We find several significant features of those events in the two different dynamical regimes: as can be seen in Fig. 10.8, the desynchronization events in the LFF regime coincide with intensity dropouts at the end of each LFF-cycle. This has been shown numerically before (Flunkert et al.,

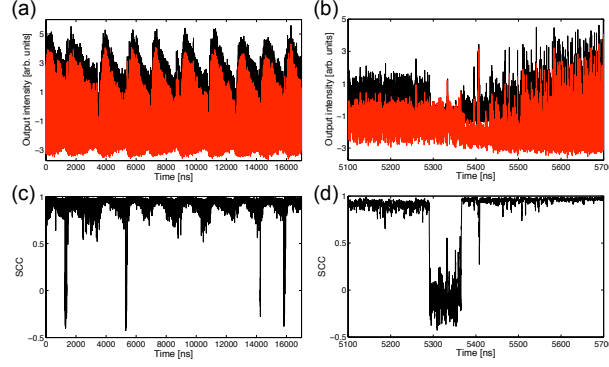


Figure 10.8: LFF dynamics and sliding cross-correlation (SLCC) as local synchronization measure. The LFF dropouts (a) and the dips in sliding cross-correlation coincide (c). (b) shows a magnification of the dynamics at one dropout point and (d) depicts the corresponding τ -length SLCC dip that is associated with a bubbling event. The intensity time series of one laser was shifted vertically for better visibility.

2009). It has been found that often dropouts take place first in one laser but not the other so that the intensity traces desynchronize (Fig. 10.8(b)). Because of the coupling delay τ the dropouts of both lasers then occur with a relative time shift of τ after which the lasers resynchronize (Heil et al., 2001). It is shown in Fig. 10.8(d) that the length of the desynchronization events in the LFF case usually corresponds to the delay time τ . It is also apparent that in the LFF regime the desynchronization events always coincide with intensity dropouts but not every dropout is accompanied by a desynchronization event (see Fig. 10.8(a,c)). In between the desynchronization events (i.e. in synchronized behavior) the synchronization level is very high, going beyond 0.95 in our experiments.

In the case of the Coherence Collapse regime, which we attain experimentally by increasing the pump current above the LFF-resulting range, the synchronization dynamics are much different due to the fact that the overall dynamics also differ much from LFF behavior. The dynamics only take place on a fast timescale, i.e.

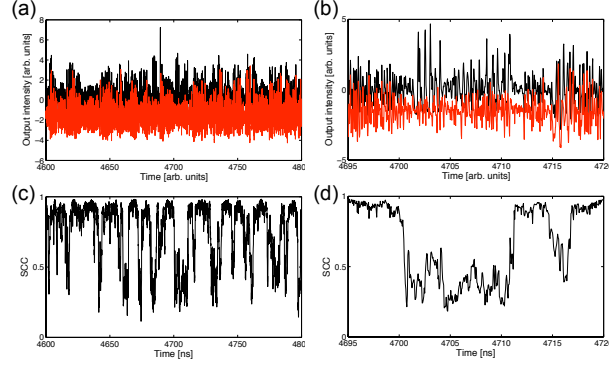


Figure 10.9: Laser dynamics in the coherence collapse (a) and the corresponding sliding cross-correlation (SLCC) time series (c). The SLCC shows distinct dips that correspond to local desynchronization. The upper level of the correlation time series exhibits a value higher than 0.90. The intensity time series of one laser was shifted vertically for better visibility.

there is no larger timescale like the one associated with the LFFs (see Fig. 10.9). We observe high-frequency short desynchronization events with a duration of the order of 1 ns. The intervals of synchronized behavior exhibit a high correlation coefficient in this case too, exceeding 0.90. The short stepsize for the sliding cross-correlation allows us to resolve the fast synchronization dynamics with good accuracy (Fig. 10.9(c,d)).

On the average, increasing the pump current leads to more desynchronization events, which in turn then of course decrease the overall cross-correlation. In the coherence collapse the bubbling events become shorter on average but also more frequent. However, in the whole pump current range we investigated, the local correlation coefficient (SLCC value) for synchronized time intervals does not change much with increasing current.

We now analyze the distribution of the sliding cross-correlation. Fig. 10.10 shows the normalized distribution of the SLCC for six pump current values. We notice that

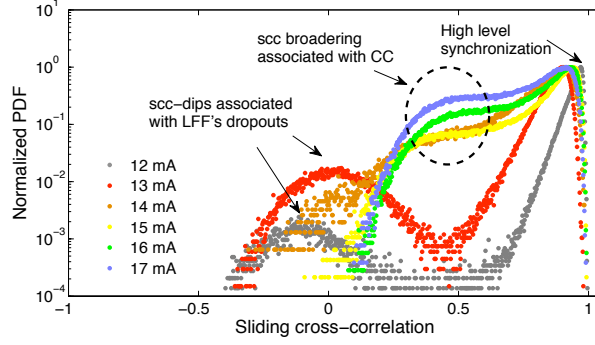


Figure 10.10: Probability distributions of the sliding cross-correlation for 6 different pump currents. Note the semi-logarithmic scale in the y -axis.

the distributions broaden significantly with increasing current. However, even in the coherence collapse the timetraces still show a significant fraction of synchronization which is represented by the predominant peaks at high correlation values. For the two curves associated with the LFF regime we can see broad peaks at -0.15 and 0.0 , respectively, that correspond to the negative SLCC values, associated with the power dropouts that are characteristic of the LFF regime (Fig. 10.8(c)). We deduce that the overall correlation (circles in Fig. 10.7) decreases with increasing pump current due to an increase in the number of bubbling events. That means that intervals of high level synchronization still occur, but are more often interrupted by a desynchronization event. A global decrease in synchronization would shift the peaks in Fig. 10.10 towards lower correlation values for increasing current, and can therefore be dismissed as a reason for the decrease in the maximum of the cross-correlation functions. The above is underlined by the fact that the fraction of timetraces that exhibit synchronized dynamics decreases with the pump current in Fig. 10.7. As synchronization threshold for the SLCC we choose $C_{thr} = 0.5$. Although that value is somewhat arbitrary, a higher threshold value only changes the slope of the curve slightly, but the overall monotony persists. We chose a low correlation threshold to make sure that we only capture real desynchronization events in the LFF regime. In

the coherence collapse the SLCC usually dips below 0.5 at an event (see Fig. 10.9).

Using the methodology described above for the event-based approach we now scan the SLCC timetraces for bubbling events by choosing the three necessary thresholds. We want to quantitatively characterize the bubbling events in terms of duration and inter-event interval length (IEI) and obtain a dependence of these characteristics on the pump current. In Fig. 10.11 the corresponding histograms for $I_p = 15 - 17$ mA are shown for threshold values of $\Delta T_{thr} = 0.5$ ns, $C_{thr} = 0.5$ and $IEI_{thr} = 0.5$ ns. For input currents $I_p = 12$ mA and $I_p = 13$ mA (which result in LFF dynamics) only 7 and 20, respectively, events are captured. As mentioned above, these are usually relatively long (τ length) events which are isolated, i.e. the IEI is of the order of microseconds. Therefore, we present only histogram data of bubbling events for the CC cases.

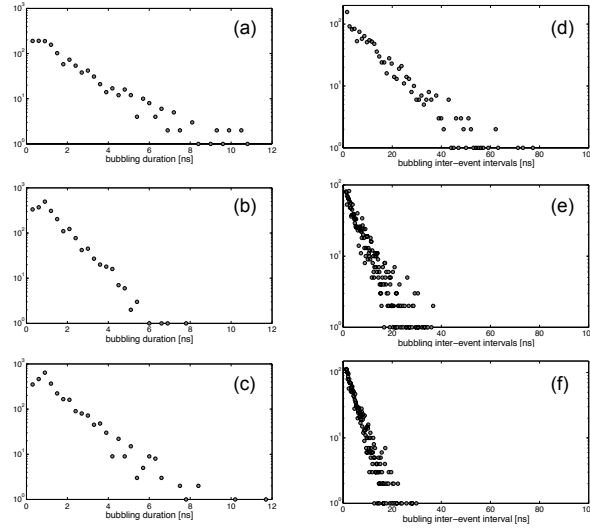


Figure 10.11: Histograms for bubbling duration (a-c) and for inter-event interval length (d-f) for pump currents $I = 15 - 17$ mA. The thresholds used for this analysis are $\Delta T_{thr} = 0.5$ ns, $C_{thr} = 0.5$ and $IEI_{thr} = 0.5$ ns. Note the logarithmic scale for the histogram counts.

As can be seen in Fig. 10.11, the distribution of the IEI scales towards more

frequent bubbling (or shorter inter-event intervals) with increasing current, which of course means a significant increase in the number of bubbling events. Relatively isolated events become more and more rare with increasing I_p . The distribution of bubbling duration is not affected much, apart from the fact that for increasing current, less of the longer events are present. It has to be mentioned that the seeming predominance of a bubbling duration of 1 ns (see e.g. Fig. 10.11(c)) is a numerical artifact because of choosing a window size of 1 ns for the computation of the SLCC.

The question remains what happens for larger pump currents. It is justifiable to conjecture that once we reach the computational limit of our SLCC (duration threshold T_{thr} and window size) and all captured events have a length of around 1 ns and an IEI of the connectivity threshold IEI_{thr} , the output time series are "saturated" with desynchronization events. Beyond this hypothetical limit, the local correlation will decrease globally, as no time intervals of highly synchronized dynamics will persist.

10.3 Conclusions

We have experimentally achieved high-quality zero-lag synchronization of two fiber-coupled semiconductor lasers, with correlation coefficients higher than 0.95. We have shown general differences in synchronization dynamics between the LFF and the CC. Due to the high-definition measurement equipment that we have used (during a stay in the laboratory of Prof. Ingo Fischer at IFISC, Palma de Mallorca), we have been able to analyze the time-depending synchronization with high resolution using a sliding cross-correlation scheme, and identify distinct desynchronization events which are attributed to the bubbling phenomenon. We have analyzed the role of the detuning on the synchronization quality. We have observed that it is possible to achieve a high synchronization quality for a wide range of frequency mismatch. We have also related the decrease in the overall correlation between the time series of the intensity dynamics of the lasers as the laser pump current increases with

a corresponding increase in the frequency of the bubbling events. Furthermore, we have shown that with increasing current, only the events with shorter duration persist.

Chapter 11

Conclusions and future work

In this Thesis we have presented experimental and numerical results that can be divided into two main groups: study of the chaotic dynamics of a semiconductor laser with feedback and study the synchronization of semiconductor lasers under different coupling architectures.

11.1 On the chaotic dynamics of a semiconductor laser with feedback

Semiconductor lasers with optical feedback have been profusely studied during the last two decades as models of nonlinear dynamical systems. We have been interested in this Thesis on quantifying the levels of stochasticity and complexity of these dynamical systems. Accordingly, in Part II of this Thesis we have presented experimental evidence that a semiconductor laser with feedback can behave as a stochastic or as a deterministic (complex) system depending on the control parameters. In particular, we have observed that at low pump currents, the dropouts are basically induced by noise and they are statistically independent one of the other. On the other hand, when the pump current of the laser is sufficiently high, the

system starts to show correlations between the dropouts. We have shown that a two-state kinetic model explains the mechanism of appearance of those correlations.

We have also observed correlations in the time series of power dropouts, reflected in the fact that some particular patterns for the sequence of consecutive dropouts (and the transitions between them) exhibit a probability of appearance higher than others, in contrast with a fully stochastic process. We can conclude that the appearance of these more probable patterns is a signature of an underlying deterministic behavior. We have compared the experimental observations with two different numerical models: the delay-differential Lang-Kobayashi (LK) model and an effective model based on coupled differential equations (EMG model) (Eguia et al., 1998). In the LK model, the statistics of patterns and their transitions is the same as in the experiments, but in the EMG model we found significant differences with the experiments.

We have also computed the entropy and the statistical complexity of the sequence of time between dropouts, which are suitable tools for quantifying structural characteristics of the LFF dropouts. The statistical complexity exhibited two distinct behaviors: one memory-less occurring at low injection currents; and the other occurring at higher current values, for which there are memory effects revealed by time correlations.

The results presented in this part of the Thesis address the debate involving the different explanations proposed for the LFF phenomenon. We observed experimentally, via novel statistical and complexity measures, that depending on the pump current the dropouts can be understood as an stochastic or deterministic nonlinear process.

11.2 On the synchronization of coupled semiconductor lasers

Semiconductor lasers are routinely used in the field of chaos synchronization. In Part III of this Thesis we have reported new synchronization phenomena between coupled semiconductor lasers under various coupling architectures. We have explored three coupling schemes: face-to-face configuration, open loop configuration and bidirectional coupling via a passive relay.

In the face-to-face configuration we have studied the switching dynamics of the leader-laggard role. We used a method capable of quantifying the level of stochasticity of a time series, based in computing the number of forbidden patterns that it exhibits. We observed that close to threshold, the system is totally stochastic. The stochasticity is reduced monotonically as the system is pumped further away from threshold. Numerical simulations of a generalized Lang-Kobayashi model were in complete agreement with the experimental observations.

In the open loop configuration, we have examined the synchronized dynamics of two semiconductor lasers coupled unidirectionally via two different paths. Under this configuration we were able to observe a synchronized behavior dominated by one of the paths. When the coupling strengths of both paths were comparable, no single coupling delay dominated over the other, but rather they coexisted in the synchronized dynamics of the system. We have observed experimentally and numerically that the dual-lag synchronization does not consist in an alternance between the two lag times, but every dropout of the receiver laser is formed by two drops in the laser intensity, occurring after the two coupling lags, separated by a plateau. Under this coupling architecture, we have numerically shown that this configuration does prevent a successful recovery of the message when both paths are comparable in strength.

In the case of bidirectional coupling via a passive relay, we have observed exper-

imentally with high time resolution that zero-lag synchronization can be achieved. We have shown general differences in synchronization dynamics between the regimes of low-frequency fluctuations (LFF) and coherence collapse (CC). We have been able to analyze in time the synchronization quality with high resolution using a sliding cross-correlation scheme, and identified distinct desynchronization events which are attributed to the bubbling phenomenon. We have also analyzed the synchronization quality when the lasers were detuned.

11.3 Perspectives for future work

As a result of the work performed in this Thesis, several questions have arisen. Next we enumerate some of the questions that could be addressed as a natural continuation of this Thesis.

With respect to the chaotic dynamics of a laser with feedback:

- Dynamical characterization of modal networks in semiconductor lasers with and without feedback. Most of the theoretical studies of dynamical phenomena in semiconductor lasers assume monomode lasing, but usually the commercial lasers emit in several longitudinal modes. It could be interesting to characterize the multimode behavior of the lasers in terms of a set of coupled nonlinear oscillators. With this study we should be able to understand the mode hopping dynamics present in most of the multimode EEL, and the effect of the feedback over the longitudinal mode dynamics.
- Detailed experimental study of the statistical properties of the transient LFF dynamics based on the theoretical work done by Zamora-Munt et al. (2010a). With this study we could apply the symbolic methodology in order to distinguish if the underlying transient dynamics is stochastic or deterministic.
- A consistent response of a system under repeated complex waveform drive

signal is an important consideration in systems as diverse as lasers and neuronal networks. One could ask if a laser with feedback operating in a region of parameters where it shows chaotic transient dynamics, is consistent under a given drive signal.

With respect to synchronization dynamics for coupled lasers:

- Generalize the study of dual-lag synchronization to networks of lasers with more than two elements. In that case a given pair of lasers might be connected by more than two paths, which would enhance the effects of path interference reported in this Thesis.
- In Ch. 10 we have studied how the system desynchronizes via bubbling for different pump current values. It could be interesting to do a similar study for different values of the detuning between the lasers. It would be also interesting to extend the study presented in this Chapter to information propagation through complex networks, in which pairs of nodes are commonly coupled via multiple paths of different lengths, and thus with different coupling delays.
- Study the zero-lag synchronization and the way in which the lasers desynchronize with an active relay (i.e. a third laser) instead of passive relay (i.e mirror), as in Ch. 10.

Appendix A

Derivation of the rate equations for a semiconductor laser

In this appendix we derive, following Petermann (1988), the rate equations for semiconductor lasers that are crucial to understand the basic laser dynamics in the presence of feedback and couplings. We will model a double heterostructure Fabry-Perot laser, but the rate equations derived below can describe any type of laser with a narrow stripe edge-emitting structure. For simplicity, we assume single longitudinal mode emission. According to Fig. A.1, the light inside the laser can be described by two electric fields corresponding to the forward (E_f) and backward (E_b) propagation. The optical field, assumed homogeneous in the plane perpendicular to the optical axes z , is given by

$$E(z, t) = E(z) \exp[i\omega t], \quad (\text{A.1})$$

where the space-dependent amplitudes of the forward and backward fields are:

$$E_f(z) = E_{0f} \exp[-ikz + \frac{1}{2}(g - \alpha_{abs})z], \quad (\text{A.2})$$

$$E_b(z) = E_{0b} \exp[-ik(L - z) + \frac{1}{2}(g - \alpha_{abs})(L - z)], \quad (\text{A.3})$$

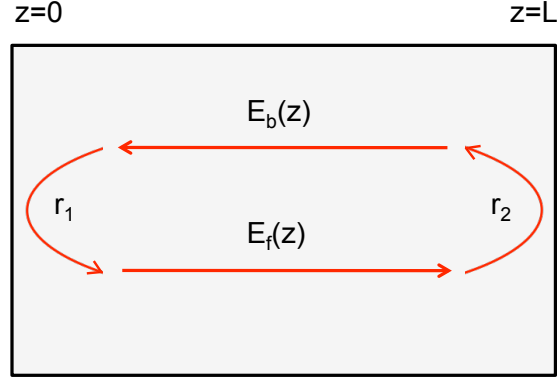


Figure A.1: Schematic representation of a semiconductor laser cavity and the corresponding traveling waves. The facets are located at $z = 0$ and $z = L$. The reflectivities of the cleaved facets are denoted by r_i and $E_f(z)$ and $E_b(z)$ are the forward and backward fields that propagate inside the cavity.

where g is the gain in the laser medium, α_{abs} is the total loss due to absorption and scattering in the laser medium and $k = \frac{n\omega}{c}$ is the wavevector, with n , c , and ω being the refracting index, the speed of light in vacuum and the optical frequency, respectively. From the boundary conditions at the facets $E_f(0) = r_1 E_b(0)$ and $E_b(L) = r_2 E_f(L)$ we find that the laser oscillation condition is the following:

$$r_1 r_2 \exp[-2ikL + (g - \alpha_{abs})L] = 1. \quad (\text{A.4})$$

The modulus of Eq. (A.4) yields a condition for the gain g . The gain at laser threshold g_{th} corresponds to the region parameters where gain balances the losses:

$$g_{th} = \alpha_{abs} + \frac{1}{L} \ln\left(\frac{1}{r_1 r_2}\right), \quad (\text{A.5})$$

Note that the term corresponding to the reflectivities represents the losses at the end facets (α_m). On the other hand the phase of Eq. (A.4) yields a condition for

the wavevector k (i.e. for the lasing frequency ω):

$$\begin{aligned} kL &= m\pi, \\ \omega_m &= m \frac{\pi c}{nL}, \end{aligned} \quad (\text{A.6})$$

being m an integer and ω_m the corresponding mode frequency. Note that n is the effective refracting index for the lasing mode. We can obtain the mode separation by:

$$\begin{aligned} d\omega &= \frac{\delta\omega}{\delta m} dm + \frac{\delta\omega}{\delta n} dn, \\ &= \frac{\pi c}{L} dm - \frac{m\pi c}{n^2 L} dn, \end{aligned} \quad (\text{A.7})$$

Taking into account that $dm = 1$ and the group refracting index $n_g = n + \omega \frac{dn}{d\omega}$, the mode separation has the following form:

$$\Delta\omega = \frac{\pi c}{n_g L} \implies \Delta\nu = \frac{c}{2Ln_g}, \quad (\text{A.8})$$

Before deriving the rate equations it would be interesting to introduce the definition for roundtrip gain and its corresponding time. The roundtrip gain is defined as follows:

$$G = r_1 r_2 \exp[-2ikL + (g - \alpha_{abs})L] = G_1 G_2, \quad (\text{A.9})$$

where G_1 is the frequency-independent term and G_2 the frequency-dependent term. On the other hand, the time inverted by one photon to go once around the cavity is given by the inverse of the mode spacing (Eq. (A.8)):

$$\tau_{cav} = \frac{2n_g L}{c}. \quad (\text{A.10})$$

In order to find an expression for G_1 and G_2 one first has to expand the wave vector k in a Taylor series around the laser threshold (i.e. around ω_{th} and N_{th}):

$$\begin{aligned} k = \frac{\omega}{c} n &= \left(k_{th} + \frac{\delta k}{\delta N} \Big|_{th} (N - N_{th}) + \frac{\delta k}{\delta \omega} \Big|_{th} (\omega - \omega_{th}) \right) \\ &= \frac{\omega_{th}}{c} \left(n_{th} + \frac{\delta n}{\delta N} (N - N_{th}) + \frac{n_g}{\omega_{th}} (\omega - \omega_{th}) \right), \end{aligned} \quad (\text{A.11})$$

note that to expand the wave vector we have assumed that the refractory index depends on the optical frequency and the carrier density. Once the wave vector is expanded, and after inserting Eq. (A.11) into Eq. (A.9) we are able to split the round trip gain into the frequency-independent term:

$$G_1 = r_1 r_2 \exp[(g - \alpha_{abs})L] \exp[-i\phi_G], \quad (\text{A.12})$$

$$\phi_G = \frac{2\omega L}{c} \frac{\delta n}{\delta N} (N - N_{th}), \quad (\text{A.13})$$

and the frequency-dependent term:

$$\begin{aligned} G_2 &= \exp\left[-\frac{2i\omega_{th}L}{c}\left(n_{th} + \frac{n_g}{\omega_{th}}(\omega - \omega_{th})\right)\right], \\ &= \exp[-i(\omega - \omega_{th})\tau_{cav}], \end{aligned} \quad (\text{A.14})$$

In order to obtain Eq. (A.14) we have used the fact that the first term of the exponential is a multiple of 2π , and the second term can also be simplified by using Eq. (A.8).

So far we have found an expression for the round trip gain. This gain is applied on each round trip to the light that travels inside the cavity. The complex time-dependent electric field inside the cavity has the general form:

$$\varepsilon(t) = E(t)e^{i(\omega_{th}t)}, \quad (\text{A.15})$$

where $E(t)$ is the slowly varying envelope of the electric field propagating in the positive direction inside the Fabry-Perot cavity, and the field oscillates essentially at ω_{th} . If we apply the expression of the gain into the traveling wave:

$$\varepsilon(t) = G\varepsilon_f(t) = GE_f(t)e^{i(\omega_{th}t)} = G_1 e^{-\tau_{cav} \frac{d}{dt}} E_f(t). \quad (\text{A.16})$$

The $e^{-\tau_{cav} \frac{d}{dt}}$ term produces a time shift of τ_{cav} in the electric field:

$$G\varepsilon_f(t) = G_1 E_f(t - \tau_{cav}). \quad (\text{A.17})$$

This final expression allows us to consider the effect of the material gain only over the slowly varying envelope of the field. After a round trip the amplitude of the

field for the traveling wave in the positive direction (E_f) has to coincide with the value of the field in the previous roundtrip, accomplishing the boundary condition of the cavity. As the boundary condition of the cavity is satisfied, we can ignore the subindex for the forward traveling wave.

$$E(t) = G_1 E(t - \tau_{cav}). \quad (\text{A.18})$$

The amplitude variations can be considered small over a round trip, so that it is possible to do Taylor expansion up to first order:

$$E(t - \tau_{cav}) \simeq E(t) - \tau_{cav} \frac{dE(t)}{dt}, \quad (\text{A.19})$$

and introducing Eq. (A.18) in the above expression:

$$\frac{dE(t)}{dt} = \frac{1}{\tau_{cav}} \left[1 - \frac{1}{G_1} \right] E(t). \quad (\text{A.20})$$

Expanding the exponential expression of the round trip gain $1/G_1$ around unity results on:

$$\frac{dE(t)}{dt} = \frac{(1 + i\alpha)}{2} [G - \gamma] E(t), \quad (\text{A.21})$$

where $\alpha = \frac{\text{Re}[\chi]}{\text{Im}[\chi]}$ is the linewidth enhancement factor, a parameter that plays an important role in establishing the linewidth of the laser oscillation. The α parameter is almost zero for most of lasers but has a positive value (usually between 1 and 7) for semiconductor lasers, plays an important role in both the spectral characteristics and the dynamics of semiconductor lasers, specially when subject to external perturbations. The parameter γ is the inverse of the photon lifetime, and G is the gain. This expression of the gain has to be completed, to take into account that the gain depends nonlinearly, in general, on the population inversion and the optical power ($P = |E|^2$). The total gain of the semiconductor laser can be linearized around the threshold value (g_{th}), taking into account its variations with the carrier density:

$$g(N) = g_{th} + \left. \frac{\partial g}{\partial N} \right|_{N_{th}} (N - N_{th}), \quad (\text{A.22})$$

where N_{th} is the carrier density at threshold.

At transparency the loss in the laser medium balances the gain. The gain must exceed this value for laser oscillations. Taking into account the density at transparency, we can define the gain at threshold as an expansion around transparency:

$$g_{th} \simeq \left. \frac{\partial g}{\partial N} \right|_{N_0} (N_{th} - N_0) \quad (\text{A.23})$$

where N_0 is the carrier density at transparency.

With that, the gain per unit time can be defined as:

$$G(N) = v_g g(N) = g_N (N - N_0) \quad (\text{A.24})$$

with $v_g = \frac{c}{n}$, and

$$g_N = v_g \left. \frac{\partial g}{\partial N} \right|_{N_0} \simeq v_g \left. \frac{\partial g}{\partial N} \right|_{N_{th}} \quad (\text{A.25})$$

is the differential gain.

This linear dependence is not accomplished for high optical powers, due to spatial hole burning and carrier heating effects. Spatial hole burning accounts for the fact that the optical field is not constant in all the active region (the standing wave inside the cavity forms an interference pattern), and the recombination is higher where the optical field is maximum. If the carrier diffusion is not sufficiently fast to supply these zones with more carriers, this effect will lead to a saturation of the gain coefficient. This can lead to emission in various frequencies, because the lasing mode experiences stronger gain saturation than the non-lasing modes. The other contribution to the saturation of the gain is given by carrier heating effects. They arise when the electrons of the conduction band are excited to higher energies. This fact hinders the recombination with the holes of the valence band, leading a saturation of the gain. The saturation coefficient accounts for both processes, and the nonlinear gain is described as:

$$G(N, |E|^2) = \frac{g_N (N - N_0)}{1 + s |E|^2} \quad (\text{A.26})$$

which accounts for the dependency of the gain with the carrier density and the amplitude of the field. In this expression, g_N is the differential gain, N_0 is the carrier density at transparency, s is the saturation coefficient, and $|E|^2$ is the power output of the field, i.e. the number of photons inside the cavity.

The dependence of the gain on the population inversion forces us to derive an equation for the carrier density, to have a complete description of the dynamics of the semiconductor laser. We start with the assumption of charge neutrality in the material, and use several approximations in order to arrive to a governing equation for the carrier density:

- We neglect carrier diffusion, because these lasers have a very small dimension of the active layer compared to the diffusion length.
- We consider that the carrier decrease due to recombination processes (spontaneous emission and non-radiative recombinations), and stimulated emission.
- We do not consider inhomogeneities in the carrier density, due to the fast carrier diffusion.

With these assumptions and taking into account that the generation of the electron-hole pairs is due to pumping, being I the pump current and e the elementary charge, the equation for the population inversion is:

$$\frac{dN}{dt} = C - \gamma_e N - G(N, |E|^2) |E|^2, \quad (\text{A.27})$$

where C is the normalized pumping current $C = \frac{I}{e}$ and γ_e is the inverse lifetime of the carriers.

A realistic model of a semiconductor laser has to include a noise term describing the spontaneous emission processes that initiates lasing emission. To that end we add an additional term in the field equation containing a complex Gaussian noise with zero mean and delta correlated in time. This term is proportional to the population inversion also to account for the quantity of spontaneous emitted photons.

Summarizing, the rate equations that describe the dynamics of a semiconductor laser and govern the electric field and the carrier density number are:

$$\frac{dE(t)}{dt} = \frac{(1 + i\alpha)}{2} [G(N, |E|^2) - \gamma] E(t) + \sqrt{2\beta N} \zeta(t), \quad (\text{A.28})$$

$$\frac{dN}{dt} = C - \gamma_e N - G(N, |E|^2) |E|^2, \quad (\text{A.29})$$

where β is the noise strength.

It is also possible to express these equations in terms of the photon number and its phase, instead of the slowly varying field. Taking into account that the equations are normalized such as: $E(t) = \sqrt{P(t)} e^{i\phi(t)}$, where $P(t) = |E(t)|^2$ is the photon number, and ϕ the phase of the field, the rate equations can be expressed as:

$$\frac{dP(t)}{dt} = [G(N, P) - \gamma] P(t), \quad (\text{A.30})$$

$$\frac{d\phi(t)}{dt} = \frac{\alpha}{2} [G(N, P) - \gamma], \quad (\text{A.31})$$

$$\frac{dN}{dt} = C - \gamma_e N - G(N, P) P, \quad (\text{A.32})$$

where the nonlinear gain is now given by:

$$G(N, P) = \frac{g_N(N - N_0)}{1 + sP}. \quad (\text{A.33})$$

In spite of being described by three rate equations, this system cannot show chaos, due to the fact that the phase variable does not affect the other two.

The steady state solutions of this reformulated system of equations are obtained setting each equation to zero. With this we obtain a solution for the number of photons, the difference of the optical frequency respect to the stationary value, and the density of carriers. There are two situations to take into account:

- Below threshold: the emission of photons is zero, the density of carriers increases linearly with the pumping current ($N_s = C/\gamma_e$), and there exists a difference between the stationary frequency (ω_s) and the instantaneous frequency of emission (ω).

- Above threshold: the emission of photons is proportional to the distance of the pump current from its threshold value. Carrier density is clamped to its threshold value, and the instantaneous frequency is clamped to the stationary value ($\Delta\omega = 0$).

Through the study of the linear stability of these solutions, it is possible to see that the solutions above threshold follow an oscillatory approach to equilibrium in response to small perturbations. This defines the relaxation oscillations (RO), which are common in any class-B lasers (Weiss & Vilaseca, 1991). This system of equations represents a two-dimensional system, which allows only to periodic solutions and not chaotic behavior. The laser oscillation occurs when the population inversion exceeds the value corresponding to the pumping threshold.

The relaxation oscillations can be explained if we introduce a step input through the pumping current. The carrier density reaches the threshold and emits light. The population inversion decreases due to light emission, and as consequence the output power decreases until the population inversion recovers. This produces oscillations between the field and the carrier density, that are the relaxation oscillations, which are reproduced only at the first instants after the turn-on of the laser, and are rapidly damped. They characterize the speed of reaction of the laser to external modulations of the pumping. The relaxation oscillation frequency sets the upper limit of the dynamics, and goes from 1 to 10 GHz typically. The enhancement of the relaxation oscillations in semiconductor lasers through external perturbations as optical feedback or optical injection causes strong instabilities, as we have seen in this Thesis. The damping rate of this oscillations, in turn, affects the response characteristics of the dynamics to these perturbations.

Appendix B

Statistical tools

B.1 Correlations

The correlation is a quantity that gives the degree of similarity between two or more variables. More specifically, the correlation coefficient points out how the variables are linearly associated. During this Thesis we have used this quantity in order to establish how a signal changes in time and whether the process repeats itself (auto-correlation), and also in order to quantify the degree of synchronization between two signals (cross-correlation).

B.1.1 Auto-correlation

As mentioned above the auto-correlation (correlation between a signal and itself) allows us to know how fast a signal changes in time (i.e. the memory of the system) and also the periodicity of the signal. For that one has to compute the auto-correlation for all the possible lag times (auto-correlation function). The normalized auto-correlation function of time-dependent signal $s(t)$ reads as follows:

$$\Gamma_{auto}(\Delta t) = \frac{\langle (s(t) - \mu)(s(t + \Delta t) - \mu) \rangle}{\sigma^2} \quad (\text{B.1})$$

where Δt is the lag time, μ is the mean value of the signal, and σ^2 its variance. Due to the fact that we are comparing the signal with itself the auto-correlation function is symmetric with respect to zero. Note that a high value of the auto-correlation function (~ 1) at a certain lag time (Δt), means a high similarity between the signal and itself at this particular value of Δt . On the contrary, at the time lags at which the signal does not repeat, the correlation takes values around zero. There is another possibility, arising when the signal and its shifted version are in anti-phase: in this case the auto-correlation function at the corresponding lag time is negative (~ -1). In order to illustrate the characteristics of the auto-correlation function we compute it for two different kinds of signals: stochastic (Fig. B.1(a)) and periodic (Fig. B.2(a)). Figure B.1(b) shows the auto-correlation function of an Ornstein-Uhlenbeck process, which is a prototype of a noisy relaxation process. We can see that the correlation exponentially decays to zero. The decay time can be related with the memory of the system.

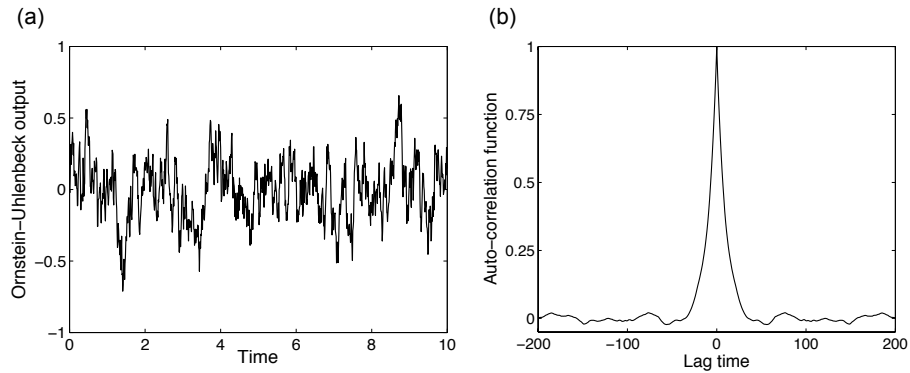


Figure B.1: (a) Time series for an Ornstein-Uhlenbeck process and the corresponding auto-correlation function (b).

On the other hand, when we analyze a periodic signal the auto-correlation function

is also periodic (Fig. B.2(b)). In this case the signal and its shifted version are equal every period, and so the correlation $\Gamma_{auto}(\Delta t = 2\pi n) = 1$. For a lag time $\Delta t = \pi$ the signal and itself are in anti-phase and the correlation is $\Gamma_{auto}(\Delta t = (2n - 1)\pi) = -1$.

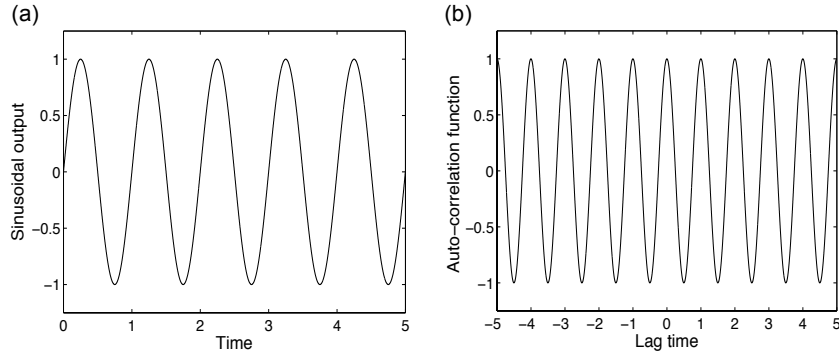


Figure B.2: (a) Time series for a periodic process and the corresponding auto-correlation function (b).

In this Thesis we have worked with chaotic signals from a semiconductor laser with feedback (Fig. B.3(a)). The behavior of the correlation in this type of signals integrates the phenomena previously described, with the signal quickly losing coherence but also showing some periodicity. As can be seen in Fig. B.3(b), the delay time induces quasi-periodicity with a period equal to τ_f . In each peak there is a decay of the correlation, followed by small oscillations around zero related with the relaxation oscillations. After a few relaxation periods the system loses the coherence. Due to the quasi-periodicity the system recovers part of the coherence in every multiple of the delay time, but after a few peaks the coherence is lost again. As can be seen in Fig. B.3(c), the auto-correlation function is modulated at large time scales, and when the laser is in the LFF regime the mean time between dropouts can be seen (secondary peak located at ~ 100 ns).

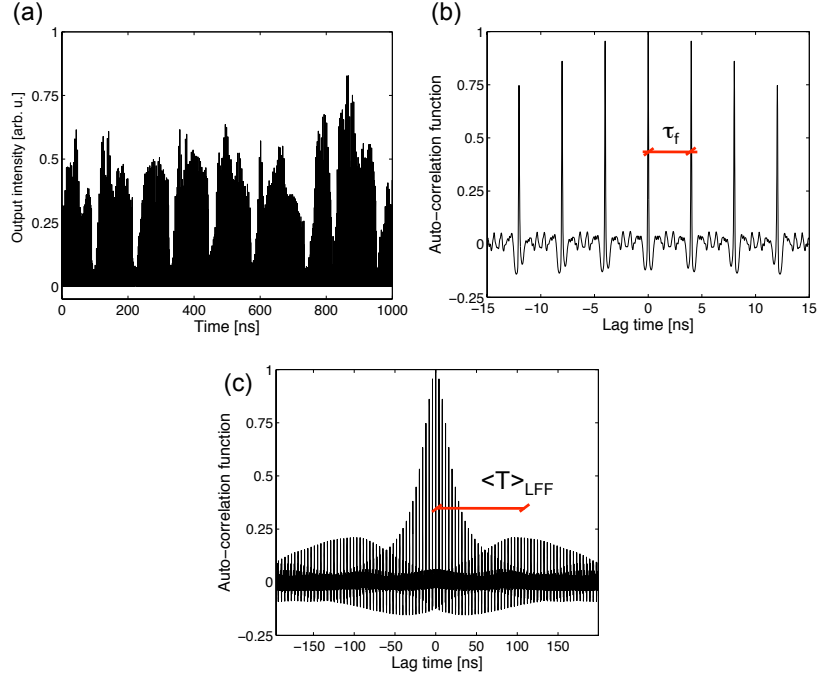


Figure B.3: (a) Numerical time series for a laser with feedback and the corresponding auto-correlation function for short (b) and large (c) time scales.

B.1.2 Cross-correlation

In order to compare two signals ($s_1(t)$ and $s_2(t)$) and know how similar they are, one can use the cross-correlation function, which has the following expression:

$$\Gamma_{cross}(\Delta t) = \frac{\langle (s_1(t) - \mu_1)(s_2(t + \Delta t) - \mu_2) \rangle}{\sigma_{s_1} \sigma_{s_2}}, \quad (\text{B.2})$$

where Δt is the lag time, μ_i is the mean value of the signal s_i , and σ_i^2 is the variance of the signals. It is worth to note that $\Gamma_{cross}(\Delta t)$ is also normalized via the product of the variances, but it is not symmetric as in the case of the auto-correlation function. When both signals are similar the maximum correlation appears at zero lag, but if one signal is delayed with respect to the other, the maximum of the correlation

appears at the delay time. Therefore, the cross-correlation function allows us to quantify the degree of synchronization between two outputs, but also the delay between them. Depending on the sign of lag time where the highest peak appears one can establish which of the two coupled systems leads the dynamics. The fall-off of the envelope depends on the robustness of the synchronization. If the cross-correlation peaks decrease very fast, the time series are correlated only during a few roundtrips of the light, and thus the signals are weakly correlated after a small time.

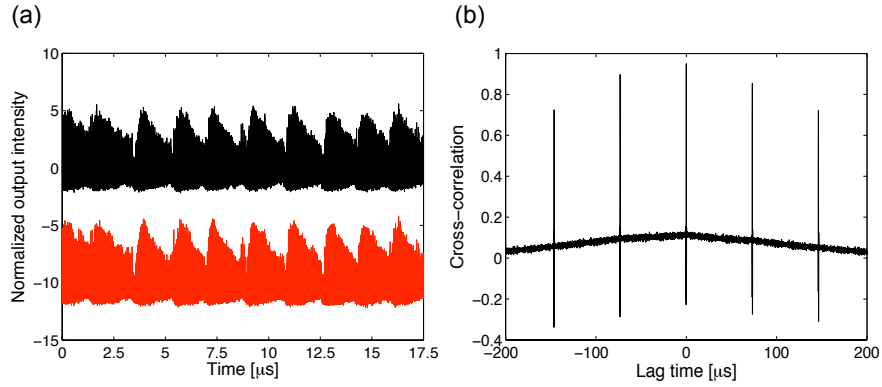


Figure B.4: (a) Experimental time series for two bidirectionally coupled lasers with feedback and the corresponding cross-correlation function (b).

The cross-correlation function is a very powerful tool to measure the degree of synchronization between coupled lasers. Figure B.4(a) plots the time series for two bidirectionally coupled lasers with feedback and in Fig. B.4(b) we show the corresponding cross-correlation function for two bidirectionally coupled lasers with feedback which exhibit zero-lag synchronization. The higher peak is at $\Delta t = 0$, and the separation between peaks shows the coupling and the feedback delay, which have the same value (i.e. $\tau_c = \tau_f = 73$ ns, see Ch. 10). Furthermore the slow decrease of the envelope means that the synchronization is very robust.

B.1.3 Sliding cross-correlation

As we have discussed above the cross-correlation tells us how similar two signals are over the whole duration of the time series. If one is interested in how the correlation varies itself in time, the sliding cross-correlation can be a useful technique. In order to calculate it, we have to divide the time signals into sliding windows of a size such that the correlation can be considered stationary. Once the cross-correlation is computed in each time window, we obtain correlations at different time values. It is worth to note that with this technique we are able to observe desynchronization events that cannot be observed with the time-averaged cross-correlation, but on the other hand we lose all information related to lag times.

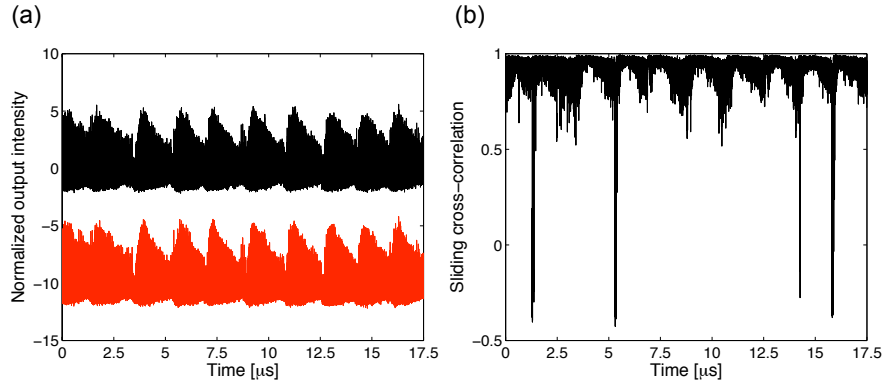


Figure B.5: (a) Experimental time series for two bidirectionally coupled lasers with feedback and the corresponding sliding cross-correlation function (b) for $\Delta t = 0$.

In Fig. B.5 we show the time series (a) and the sliding cross-correlation (b) function for two bidirectionally coupled lasers with feedback, operating at the LFF regime. In the figure we can observe desynchronization events related with the correlation drops, that would not be observed with the cross-correlation function (see Ch. 10).

Bibliography

- Abarbanel, H. D. I., Rulkov, N. F., & Sushchik, M. (1996). Generalized synchronization of chaos: The auxiliary system approach. *Physical Review E*, 53(5).
- Adler, R. (1946). A study of locking phenomena in oscillators. *Proceedings of the IRE*, 34(6), 351–357.
- Afraimovich, V. S., Verichev, N. N., & Rabinovich, M. I. (1986). Stochastic synchronization of oscillation in dissipative systems. *Radiophysics and Quantum Electronics*, 29(9), 795–803.
- Ahlers, V., Parlitz, U., & Lauterborn, W. (1998). Hyperchaotic dynamics and synchronization of external-cavity semiconductor lasers. *Physical Review E*, 58(6), 7208–7213.
- Alferov, Z. I., Andreev, V. M., Portnoi, E. L., & Trukan, M. K. (1970). Alas-gaas heterojunction injection lasers with a low room-temperature threshold. *Sov. Phys. Semicond.* 3, 1107 (1970), 3(1107).
- Amigó, J. M., Elizalde, S., & Kennel, M. B. (2008). Forbidden patterns and shift systems. *Journal of Combinatorial Theory, Series A*, 115(3), 485–504.
- Amigó, J. M., Kocarev, L., & Szczepanski, J. (2006). Order patterns and chaos. *Physics Letters A*, 355(1), 27–31.

- Amigó, J. M., Zambrano, S., & Sanjuán, M. A. F. (2007). True and false forbidden patterns in deterministic and random dynamics. *Europhys. Letters*, 79(5), 50001.
- Arecchi, F. T., Lippi, G. L., Puccioni, G. P., & Tredicce, J. R. (1984). Deterministic chaos in laser with injected signal. *Optics Communications*, 51(5), 308–314.
- Ashwin, P., Buescu, J., & Stewart, I. (1994). Bubbling of attractors and synchronisation of chaotic oscillators. *Phys. Lett. A*, 193(2), 126–139.
- Avila-Akerberg, O., & Chacron, M. (2011). Nonrenewal spike train statistics: causes and functional consequences on neural coding. *Experimental Brain Research*, 210, 353–371.
- Bandt, C., & Pompe, B. (2002). Permutation entropy: A natural complexity measure for time series. *Physical Review Letters*, 88(17).
- Bennett, M., Schatz, M. F., Rockwood, H., & Wiesenfeld, K. (2002). Huygens's clocks. *Proceedings: Mathematical, Physical and Engineering Sciences*, 458(2019), 563–579.
- Besnard, P., Meziane, B., & Stephan, G. M. (1993). Feedback phenomena in a semiconductor laser induced by distant reflectors. *Quantum Electronics, IEEE Journal of*, 29(5), 1271–1284.
- Boccaletti, S., Latora, V., Moreno, Y., Chavez, M., & Hwang, D. (2006). Complex networks: Structure and dynamics. *Physics Reports*, 424(4-5), 175–308.
- Buldú, J. M., Chialvo, D. R., Mirasso, C. R., Torrent, M. C., Chialvo, D. R., & García-Ojalvo, J. (2003). Ghost resonance in a semiconductor laser with optical feedback. *EPL (Europhysics Letters)*, 64(2).
- Buldú, J. M., García-Ojalvo, J., Mirasso, C. R., & Torrent, M. C. (2002). Stochastic entrainment of optical power dropouts. *Physical Review E*, 66(2).

Bibliography

- Buldú, J. M., García-Ojalvo, J., Mirasso, C. R., Torrent, M. C., & Sancho, J. M. (2001). Effect of external noise correlation in optical coherence resonance. *Physical Review E*, 64(5).
- Buldú, J. M., García-Ojalvo, J., & Torrent, M. C. (2004). Delay-induced resonances in an optical system with feedback. *Physical Review E*, 69(4).
- Buldú, J. M., Heil, T., Fischer, I., Torrent, M. C., & García-Ojalvo, J. (2006). Episodic synchronization via dynamic injection. *Physical Review Letters*, 96(2).
- Cencini, M., Falcioni, M., Olbrich, E., Kantz, H., & Vulpiani, A. (2000). Chaos or noise: Difficulties of a distinction. *Physical Review E*, 62(1).
- Chacron, M. J., Lindner, B., & Longtin, A. (2004). Noise shaping by interval correlations increases information transfer. *Physical Review Letters*, 92(8).
- Chacron, M. J., Longtin, A., & Maler, L. (2001). Negative interspike interval correlations increase the neuronal capacity for encoding time-dependent stimuli. *The Journal of Neuroscience*, 21(14), 5328–5343.
- Chakraborty, T., & Rand, R. H. (1988). The transition from phase locking to drift in a system of two weakly coupled van der pol oscillators. *International Journal of Non-Linear Mechanics*, 23(5-6), 369–376.
- Cox, D. R., & Lewis, P. A. W. (1966). *The statistical analysis of series of events*. Monographs on Applied Probability and Statistics, London: Chapman and Hall.
- Crutchfield, J. P., & Young, K. (1989). Inferring statistical complexity. *Physical Review Letters*, 63(2).
- Davidchack, R. L., Lai, Y.-C., Gavrielides, A., & Kovanis, V. (2000a). Chaotic transitions and low-frequency fluctuations in semiconductor lasers with optical feedback. *Physica D: Nonlinear Phenomena*, 145(1-2), 130–143.

- Davidchack, R. L., Lai, Y. C., Gavrielides, A., & Kovanis, V. (2000b). Dynamical origin of low frequency fluctuations in external cavity semiconductor lasers. *Physics Letters A*, 267(5-6), 350–356.
- Dente, G. C., Durkin, P. S., Wilson, K. A., & Moeller, C. E. (1988). Chaos in the coherence collapse of semiconductor lasers. *Quantum Electronics, IEEE Journal of*, 24(12), 2441–2447.
- D’Huys, O., Vicente, R., Erneux, T., Danckaert, J., & Fischer, I. (2008). Synchronization properties of network motifs: Influence of coupling delay and symmetry. *Chaos*, 18, 037116.
- Eguia, M. C., Mindlin, G. B., & Giudici, M. (1998). Low-frequency fluctuations in semiconductor lasers with optical feedback are induced with noise. *Physical Review E*, 58(2).
- Engel, T. A., Schimansky-Geier, L., Herz, A. V. M., Schreiber, S., & Erchova, I. (2008). Subthreshold membrane-potential resonances shape spike-train patterns in the entorhinal cortex. *Journal of Neurophysiology*, 100(3), 1576–1589.
- Englert, A., Kinzel, W., Aviad, Y., Butkovski, M., Reidler, I., Zigzag, M., Kanter, I., & Rosenbluh, M. (2010). Zero lag synchronization of chaotic systems with time delayed couplings. *Physical Review Letters*, 104(11).
- Feldman, D. P., & Crutchfield, J. P. (1998). Measures of statistical complexity: Why? *Physics Letters A*, 238(4-5), 244–252.
- Feng, J., Ye, X., Esashi, M., & Ono, T. (2010). Mechanically coupled synchronized resonators for resonant sensing applications. *Journal of Micromechanics and Microengineering*, 20(11).
- Ferdinand-Braun-Institut (2011). *Miniaturized External Cavity Diode Lasers emitting at 633 nm are best suited for application in absolute distance interferometry*

and atomic spectroscopy.

URL <http://www.fbh-berlin.com/whats-new/research/2011>

- Fischer, I., Liu, Y., & Davis, P. (2000). Synchronization of chaotic semiconductor laser dynamics on subnanosecond time scales and its potential for chaos communication. *Physical Review A*, 62(1), 011801.
- Fischer, I., Van Tartwijk, G., Levine, A. M., Elsässer, W., Göbel, E., & Lenstra, D. (1996). Fast pulsing and chaotic itinerancy with a drift in the coherence collapse of semiconductor lasers. *Physical Review Letters*, 76(2), 220–223.
- Fischer, I., Vicente, R., Buldú, J. M., Peil, M., Mirasso, C. R., Torrent, M. C., & García-Ojalvo, J. (2006). Zero-lag long-range synchronization via dynamical relaying. *Phys. Rev. Lett.*, 97(12), 123902.
- Flunkert, V., D’Huys, O., Danckaert, J., Fischer, I., & Schöll, E. (2009). Bubbling in delay-coupled lasers. *Phys. Rev. E*, 79, 065201 (R).
- Gabor, D. (1946). Theory of communication. part 1: The analysis of information. *Electrical Engineers - Part III: Radio and Communication Engineering, Journal of the Institution of*, 93(26), 429–441.
- Giacomelli, G., Giudici, M., Balle, S., & Tredicce, J. R. (2000). Experimental evidence of coherence resonance in an optical system. *Physical Review Letters*, 84(15).
- Giudici, M., Green, C., Giacomelli, G., Nespolo, U., & Tredicce, J. R. (1997). Andronov bifurcation and excitability in semiconductor lasers with optical feedback. *Physical Review E*, 55(6).
- Gonzalez, C. M., Torrent, M. C., & Garcia-Ojalvo, J. (2007). Controlling the leader-laggard dynamics in delay-synchronized lasers. *Chaos*, 17(3), 033122–8.

Bibliography

- Grassberger, P. (1986). Toward a quantitative theory of self-generated complexity. *International Journal of Theoretical Physics*, 25, 907–938. 10.1007/BF00668821.
- Grassberger, P., & Procaccia, I. (1983). Measuring the strangeness of strange attractors. *Physica D: Nonlinear Phenomena*, 9(1-2), 189–208.
- Haken, H. (1975). Analogy between higher instabilities in fluids and lasers. *Phys. Lett.*, 53, 77–78.
- Hales, J., Zhukov, A., Roy, R., & Dykman, M. I. (2000). Dynamics of activated escape and its observation in a semiconductor laser. *Physical Review Letters*, 85(1).
- Hall, R. N., Fenner, G. E., Kingsley, J. D., Soltys, T. J., & Carlson, R. O. (1962). Coherent light emission from gaas junctions. *Physical Review Letters*, 9(9).
- Hawkes, J., & Latimer, I. (1995). *Lasers: Theory and Practice*. ISBN 0135214939. Prentice Hall.
- Hayashi, I., Panish, M. B., Foy, P. W., & Sumski, S. (1970). Junction lasers which operate continuously at room temperature. *Applied Physics Letters*, 17(3), 109–111.
- Heil, T. (2000). Stabilization of feedback-induced instabilities in semiconductor lasers. *Journal of Optics B: Quantum and Semiclassical Optics*, 2(3).
- Heil, T., Fischer, I., & Elsässer, W. (1998). Coexistence of low-frequency fluctuations and stable emission on a single high-gain mode in semiconductor lasers with external optical feedback. *Physical Review A*, 58(4).
- Heil, T., Fischer, I., & Elsässer, W. (1999a). Influence of amplitude-phase coupling on the dynamics of semiconductor lasers subject to optical feedback. *Physical Review A*, 60(1).

- Heil, T., Fischer, I., Elsässer, W., Mulet, J., & Mirasso, C. R. (2001). Chaos synchronization and spontaneous symmetry-breaking in symmetrically delay-coupled semiconductor lasers. *Phys. Rev. Lett.*, *86*(5), 795–798.
- Heil, T., Fischer, I., Elsässer, W., Mulet, J., & Mirasso, C. R. (1999b). Statistical properties of low-frequency fluctuations during single-mode operation in distributed-feedback lasers: experiments and modeling. *Opt. Lett.*, *24*(18), 1275–1277.
- Henry, C., & Kazarinov, R. (1986). Instability of semiconductor lasers due to optical feedback from distant reflectors. *IEEE J. Quantum Electron.*, *22*(2), 294–301.
- Herstens, T. (2005). An overview of laser diode characteristics. Tech. Rep. 5, ILX Lightwave.
- Hicke, K., D’Huys, O., Flunkert, V., Danckaert, J., Schöll, E., Danckaert, J., & Fischer, I. (2011). Mismatch and synchronization: Influence of asymmetries in systems of two delay-coupled lasers. *Phys. Rev. E*, *83*(1), 056211.
- Hohl, A., van der Linden, H. J. C., & Roy, R. (1995). Determinism and stochasticity of power-dropout events in semiconductor lasers with optical feedback. *Opt. Lett.*, *20*(23), 2396–2398.
- Hong, Y., & Shore, K. A. (2005a). Influence of optical feedback time-delay on power-drops in vertical-cavity surface-emitting lasers. *Quantum Electronics, IEEE Journal of*, *41*(8), 1054–1057.
- Hong, Y., & Shore, K. A. (2005b). Statistical measures of the power dropout ratio in semiconductor lasers subject to optical feedback. *Opt. Lett.*, *30*(24), 3332–3334.
- Huyet, G., Porta, P. A., Hegarty, S. P., McInerney, J. G., & Holland, F. (2000). A low-dimensional dynamical system to describe low-frequency fluctuations in a semiconductor laser with optical feedback. *Optics Communications*, *180*(4-6), 339–344.

Bibliography

- Illing, L., Hoth, G., Shareshian, L., & May, C. (2011). Scaling behavior of oscillations arising in delay-coupled optoelectronic oscillators. *Physical Review E*, *83*(2), 026107.
- Jalan, S., Jost, J., & Atay, F. M. (2006). Symbolic synchronization and the detection of global properties of coupled dynamics from local information. *Chaos: An Interdisciplinary Journal of Nonlinear Science*, *16*(3), 033124–9.
- Jiang, N., Pan, W., Luo, B., Yan, L., Xiang, S., Yang, L., Zheng, D., & Li, N. (2010). Properties of leader-laggard chaos synchronization in mutually coupled external-cavity semiconductor lasers. *Phys. Rev. E*, *81*, 066217.
- Kantz, H., & Olbrich, E. (2000). Coarse grained dynamical entropies: Investigation of high-entropic dynamical systems. *Physica A: Statistical Mechanics and its Applications*, *280*(1-2), 34–48.
- Kaspar, F., & Schuster, H. G. (1987). Easily calculable measure for the complexity of spatiotemporal patterns. *Physical Review A*, *36*(2).
- Ke, D. G., & Tong, Q. Y. (2008). Easily adaptable complexity measure for finite time series. *Physical Review E*, *77*(6).
- Kim, M., Roy, R., Aron, J., Carr, T., & Schwartz, I. (2005). Scaling behavior of laser population dynamics with time-delayed coupling: Theory and experiment. *Physical Review Letters*, *94*(8), 88101.
- Kullback, S., & Leibler, R. A. (1951). On information and sufficiency. *The Annals of Mathematical Statistics*, *22*(1), 79–86.
- Lam, W. S., Guzdar, P. N., & Roy, R. (2003). Effect of Spontaneous Emission Noise and Modulation on Semiconductor Lasers Near Threshold with Optical Feedback. *Int. J. Mod. Phys. B*, *17*, 4123–4138.

- Landsman, A. S., & Schwartz, I. B. (2007). Complete chaotic synchronization in mutually coupled time-delay systems. *Phys. Rev. E*, 75(2), 026201.
- Lang, R., & Kobayashi, K. (1980). External optical feedback effects on semiconductor injection laser properties. *Quantum Electronics, IEEE Journal of*, 16(3), 347.
- Larger, L., Goedgebuer, J., & Delorme, F. (1998). Optical encryption system using hyperchaos generated by an optoelectronic wavelength oscillator. *Physical Review E*, 57(6), 6618–6624.
- Lee, C. H., Yoon, T. H., & Shin, S. Y. (1985). Period doubling and chaos in a directly modulated laser diode. *Applied Physics Letters*, 46(1), 95–97.
- Lempel, A., & Ziv, J. (Jan 1976). On the complexity of finite sequences. *Information Theory, IEEE Transactions on*, 22(1), 75–81.
- Lindner, B., & Schwalger, T. (2007). Correlations in the sequence of residence times. *Physical Review Letters*, 98(21).
- Liu, J. M. (2005). *Photonic devices*. ISBN 0521551951. Cambridge.
- Lopez-Ruiz, R., Mancini, H. L., & Calbet, X. (1995). A statistical measure of complexity. *Physics Letters A*, 209(5-6), 321–326.
- Marino, F., Giudici, M., Barland, S., & Balle, S. (2002). Experimental evidence of stochastic resonance in an excitable optical system. *Physical Review Letters*, 88(4).
- Martin, M. T., Plastino, A., & Rosso, O. A. (2006). Generalized statistical complexity measures: Geometrical and analytical properties. *Physica A: Statistical Mechanics and its Applications*, 369(2), 439–462.
- Martinez Avila, J. F., Cavalcante, H. L., & Rios-Leite, J. (2004). Experimental deterministic coherence resonance. *Physical Review Letters*, 93(14).

- Masoller, C. (1997a). Implications of how the linewidth enhancement factor is introduced on the lang and kobayashi model. *Quantum Electronics, IEEE Journal of*, 33(5), 796–803.
- Masoller, C. (1997b). Spatiotemporal dynamics in the coherence collapsed regime of semiconductor lasers with optical feedback. *Chaos: An Interdisciplinary Journal of Nonlinear Science*, 7(3), 455–462.
- Masoller, C. (2001). Anticipation in the synchronization of chaotic semiconductor lasers with optical feedback. *Physical Review Letters*, 86(13).
- Mendez, J. M., Aliaga, J., & Mindlin, G. B. (2002). Topologically inequivalent orbits induced by noise. *Physical Review Letters*, 89(16).
- Méndez, J. M., Aliaga, J., & Mindlin, G. B. (2005). Limits on the excitable behavior of a semiconductor laser with optical feedback. *Physical Review E*, 71(2).
- Mendez, J. M., Laje, R., Giudici, M., Aliaga, J., & Mindlin, G. B. (2001). Dynamics of periodically forced semiconductor laser with optical feedback. *Physical Review E*, 63(6).
- Mirasso, C., Colet, P., & García-Fernández, P. (1996). Synchronization of chaotic semiconductor lasers: Application to encoded communications. *Photonics Technology Letters, IEEE*, 8(2), 299–301.
- Mirasso, C. R., Mulet, J., & Masoller, C. (2002). Chaos shift-keying encryption in chaotic external-cavity semiconductor lasers using a single-receiver scheme. *Photonics Technology Letters, IEEE*, 14(4), 456–458.
- Mork, J., Tromborg, B., & Mark, J. (1992). Chaos in semiconductor lasers with optical feedback - Theory and experiment. *IEEE J. Quantum Electron.*, 28, 93–108.

Bibliography

- Mulet, J., & Mirasso, C. R. (1999). Numerical statistics of power dropouts based on the lang-kobayashi model. *Physical Review E*, 59(5).
- Murakami, A., & Ohtsubo, J. (2002). Synchronization of feedback-induced chaos in semiconductor lasers by optical injection. *Physical Review A*, 65(3).
- Murakami, A., & Shore, K. (2005). Chaos-pass filtering in injection-locked semiconductor lasers. *Physical Review A*, 72(5), 053810.
- Nagai, Y., & Lai, Y. C. (1997). Periodic-orbit theory of the blowout bifurcation. *Phys. Rev. E*, 56, 4031–4041.
- Nathan, M. I., Dumke, W. P., Burns, G., Dill, F. H., & Lasher, G. (1962). Stimulate emission of radiation from gaas p-n junctions. *Applied Physics Letters*, 1(3), 62–64.
- Ohtsubo, J. (2002). Chaotic dynamics in semiconductor lasers with optical feedback. In *Progress in Optics*, vol. 44, (pp. 1–84). Elsevier.
- Palus, M. (1996). Coarse-grained entropy rates for characterization of complex time series. *Physica D: Nonlinear Phenomena*, 93(1-2), 64–77.
- Pecora, L. M., & Carroll, T. L. (1990). Synchronization in chaotic systems. *Physical Review Letters*, 64(8).
- Peil, M., Larger, L., & Fischer, I. (2007). Versatile and robust chaos synchronization phenomena imposed by delayed shared feedback coupling. *Phys. Rev. E rapid comm.*, 76(4), 045201.
- Petermann, K. (1988). *Laser diode modulation and noise*. KTK Scientific Publishers.
- Pikovsky, A., Rosenblum, M., & Kurths, J. (2001). *Synchronization: A universal concept in nonlinear sciences*. 12. Cambridge University press.

- Pincus, S. (1995). Approximate entropy (apen) as a complexity measure. *Chaos: An Interdisciplinary Journal of Nonlinear Science*, 5(1), 110–117.
- Prasad, A., Lai, Y. C., Gavrielides, A., & Kovanis, V. (2001). Low-frequency fluctuations in external cavity semiconductor lasers: understanding based on a simple dynamical model. *Journal of Optics B: Quantum and Semiclassical Optics*, 3(4).
- Quist, T. M., Rediker, R. H., Keyes, R. J., Krag, W. E., Lax, B., McWhorter, A. L., & Zeigler, H. J. (1962). Semiconductor maser of gaas. *Applied Physics Letters*, 1(4), 91–92.
- Ray, W., Lam, W. S., Guzdar, P. N., & Roy, R. (2006). Observation of chaotic itinerancy in the light and carrier dynamics of a semiconductor laser with optical feedback. *Physical Review E*, 73(2).
- Rosenblum, M. G., Pikovsky, A. S., & Kurths, J. (1996). Phase synchronization of chaotic oscillators. *Physical Review Letters*, 76(11).
- Rosso, O. A., Larrondo, H. A., Martin, M. T., Plastino, A., & Fuentes, M. A. (2007). Distinguishing noise from chaos. *Physical Review Letters*, 99(15).
- Rosso, O. A., Martin, M. T., & Plastino, A. (2003). Brain electrical activity analysis using wavelet-based informational tools (ii): Tsallis non-extensivity and complexity measures. *Physica A: Statistical Mechanics and its Applications*, 320, 497–511.
- Rubido, N., Tiana-Alsina, J., Torrent, M. C., Garcia-Ojalvo, J., & Masoller, C. (2011). Language organization and temporal correlations in the spiking activity of an excitable laser: Experiments and model comparison. *Physical Review E*, 84(2).
- Sacher, J., Baums, D., Panknin, P., Elsässer, W., & Göbel, E. O. (1992). Intensity instabilities of semiconductor lasers under current modulation, external light injection, and delayed feedback. *Physical Review A*, 45(3).

Bibliography

- Sano, T. (1994). Antimode dynamics and chaotic itinerancy in the coherence collapse of semiconductor lasers with optical feedback. *Phys. Rev. A*, 50(3), 2719–2726.
- Sauer, M., & Kaiser, F. (1998). On-off intermittency and bubbling in the synchronization break-down of coupled lasers. *Phys. Lett. A*, 243(1-2), 38–46.
- Schawlow, A. L., & Townes, C. H. (1958). Infrared and optical masers. *Phys. Rev.*, 112(6), 1940–1949.
- Schuster, H. G., & Wagner, P. (1989). Mutual entrainment of two limit cycle oscillators with time delayed coupling. *Progress of Theoretical Physics*, 81, 939–945.
- Schwalger, T., & Lindner, B. (2008). Higher-order statistics of a bistable system driven by dichotomous colored noise. *Physical Review E*, 78(2).
- Schwalger, T., & Lindner, B. (2011). *Temporal correlations induced by intrinsic rate switching in excitable systems (Personal communication)*.
- Simcik, J. (1995). Module 4-6 diode laser power supplies. Tech. rep., CORD’s FIPSE-supported Curriculum Morphing Project.
- Sivaprakasam, S., & Shore, K. (1999). Signal masking for chaotic optical communication using external-cavity diode lasers. *Optics Letters*, 24(17), 1200–1202.
- Strogatz, S. H., & Stewart, I. (1993). Coupled oscillators and biological synchronization. *Sci. Am. Mag*, 269(102).
- Sukow, D. W., & Gauthier, D. J. (2000). Entraining power-dropout events in an external-cavity semiconductor laser using weak modulation of the injection current. *Quantum Electronics, IEEE Journal of*, 36(2), 175–183.
- Sukow, D. W., Heil, T., Fischer, I., Gavrielides, A., Hohl-AbiChedid, A., & Elsässer, W. (1999). Picosecond intensity statistics of semiconductor lasers operating in the low-frequency fluctuation regime. *Physical Review A*, 60(1).

- Takiguchi, Y., Fujino, H., & Ohtsubo, J. (1999). Experimental synchronization of chaotic oscillations in externally injected semiconductor lasers in a low-frequency fluctuation regime. *Optics Letters*, *24*(22), 1570–1572.
- Takiguchi, Y., Liu, Y., & Ohtsubo, J. (1998). Low-frequency fluctuation induced by injection-current modulation in semiconductor lasers with optical feedback. *Opt. Lett.*, *23*(17), 1369–1371.
- Thévenin, J., Romanelli, M., Vallet, M., Brunel, M., & Erneux, T. (2011). Resonance assisted synchronization of coupled oscillators: Frequency locking without phase locking. *Physical Review Letters*, *107*(10).
- Tiana-Alsina, J., Buldu, J. M., Torrent, M. C., & Garcia-Ojalvo, J. (2009). Quantifying stochasticity in the dynamics of delay-coupled semiconductor lasers via forbidden patterns. *Royal Society of London Philosophical Transactions Series A*, *368*, 367–377.
- Tiana-Alsina, J., Torrent, M. C., Rosso, O. A., Masoller, C., & Garcia-Ojalvo, J. (2010). Quantifying the statistical complexity of low-frequency fluctuations in semiconductor lasers with optical feedback. *Physical Review A*, *82*(1).
- Tkach, R., & Chraplyvy, A. (1986). Regimes of feedback effects in 1.5- μm distributed feedback lasers. *Lightwave Technology, Journal of*, *4*(11), 1655.
- Torcini, A., Barland, S., Giacomelli, G., & Marin, F. (2006). Low-frequency fluctuations in vertical cavity lasers: Experiments versus lang-kobayashi dynamics. *Physical Review A*, *74*(6).
- Uchida, A., McAllister, R., Meucci, R., & Roy, R. (2003). Generalized synchronization of chaos in identical systems with hidden degrees of freedom. *Physical Review Letters*, *91*(17).
- van Tartwijk, G. H. M., & Agrawal, G. P. (1998). Laser instabilities: a modern perspective. *Progress in Quantum Electronics*, *22*(2), 43–122.

- Vaschenko, G., Giudici, M., Rocca, J. J., Menoni, C. S., Tredicce, J. R., & Balle, S. (1998). Temporal dynamics of semiconductor lasers with optical feedback. *Physical Review Letters*, 81(25).
- Venkataramani, S. C., Hunt, B. R., & Ott, E. (1996). Bubbling transition. *Phys. Rev. E*, 54(2), 1346–1360.
- Vicente, R. (2006). *Nonlinear dynamics and synchronization of bidirectionally coupled semiconductor lasers*. Ph.D. thesis, Universitat de les illes balears.
- Vicente, R., Mirasso, C. R., & Fischer, I. (2007). Simultaneous bidirectional message transmission in a chaos-based communication scheme. *Opt. Lett.*, 32(4), 403–405.
- Viktorov, E. A., & Mandel, P. (2000). Low frequency fluctuations in a multimode semiconductor laser with optical feedback. *Physical Review Letters*, 85(15).
- Wackerbauer, R., Witt, A., Atmanspacher, H., Kurths, J., & Scheingraber, H. (1994). A comparative classification of complexity measures. *Chaos, Solitons & Fractals*, 4(1), 133–173.
- Weiss, C. O., & Vilaseca, R. (1991). *Dynamics of lasers*. VCH Weinheim.
- Wieczorek, S., Simpson, T. B., Krauskopf, B., & Lenstra, D. (2002). Global quantitative predictions of complex laser dynamics. *Physical Review E*, 65(4).
- Yacomotti, A. M., Eguia, M. C., Aliaga, J., Martinez, O. E., Mindlin, G. B., & Lipsich, A. (1999). Interspike time distribution in noise driven excitable systems. *Physical Review Letters*, 83(2).
- Young, K., Chen, Y., Kornak, J., Matson, G. B., & Schuff, N. (2005). Summarizing complexity in high dimensions. *Physical Review Letters*, 94(9).
- Young, K., & Schuff, N. (2008). Measuring structural complexity in brain images. *NeuroImage*, 39(4), 1721–1730.

- Zamora-Munt, J., Masoller, C., & García-Ojalvo, J. (2010a). Transient low-frequency fluctuations in semiconductor lasers with optical feedback. *Physical Review A*, 81(3).
- Zamora-Munt, J., Masoller, C., Garcia-Ojalvo, J., & Roy, R. (2010b). Crowd synchrony and quorum sensing in delay-coupled lasers. *Physical Review Letters*, 105(26), 264101.
- Zunino, L., Zanin, M., Tabak, B. M., Perez, D. G., & Rosso, O. A. (2009). Forbidden patterns, permutation entropy and stock market inefficiency. *Physica A: Statistical Mechanics and its Applications*, 388(14), 2854–2864.